

AD-A247 168



2

MODELLING BATHYMETRIC CONTROL OF
NEAR COASTAL WAVE CLIMATE: REPORT 3

by

James T. Kirby

with J. P. Anton, J. A. Baillard, R. A. Dalrymple,
J. W. DeVries and R. T. Guza



RESEARCH REPORT NO. CACR-92-01
February 1992

This document has been approved
for public release and sale; its
distribution is unlimited.



CENTER FOR APPLIED COASTAL RESEARCH

DEPARTMENT OF CIVIL ENGINEERING
UNIVERSITY OF DELAWARE
NEWARK, DELAWARE 19716

92 2 26 009

92-04994



REPORT DOCUMENTATION PAGE

1. Report No.	2.	3. Recipient's Accession No.	
4. Title and Subtitle MODELLING BATHYMETRIC CONTROL OF NEAR COASTAL WAVE CLIMATE: REPORT 3		5. Report Date February 1992	
7. Author(s) James T. Kirby		8. Performing Organization Report No. CACR-93-01	
9. Performing Organization Name and Address UNIVERSITY OF DELAWARE Department of Civil Engineering Center for Applied Coastal Research Newark, DE 19716		10. Project/Task/Work Unit No.	
		11. Contract or Grant No. N00014-90-J-1678	
12. Sponsoring Organization Name and Address Office of Naval Research 800 North Quincy Street Arlington, VA 22217		13. Type of Report Final Report	
		14.	
15. Supplementary Notes			
16. Abstract This document is the final report for the ONR project N00014-90-J-1678, the third phase of a study entitled "Modelling bathymetric control of near coastal wave climate." The effort in this phase of the study was concentrated on the extension of the angular spectrum modelling technique to nonlinear shallow water waves, and to further studies of the Bragg reflection mechanism for surface waves being reflected by artificial or natural bars.			
17. Originator's Key Words		18. Availability Statement	
19. U. S. Security Classif. of the Report Unclassified	20. U. S. Security Classif. of This Page Unclassified	21. No. of Pages	22. Price

**MODELLING BATHYMETRIC CONTROL OF
NEAR COASTAL WAVE CLIMATE: REPORT 3**

by

James T. Kirby

with J. P. Anton, J. A. Baillard, R. A. Dalrymple, J. W. DeVries
and R. T. Guza

RESEARCH REPORT NO. CACR-92-01
February 1992

CENTER FOR APPLIED COASTAL RESEARCH
DEPARTMENT OF CIVIL ENGINEERING
UNIVERSITY OF DELAWARE
NEWARK, DELAWARE 19716

1	Summary	2
2	Bragg Reflection	2
3	Angular Spectrum Modelling	2

Appendix A: Bragg Reflection of Waves by Artificial Bars

Appendix B: Bragg Reflection Breakwater: A New Shore Protection Method?

Appendix C: Considerations in Using Bragg Reflection for Storm Erosion Protection

Appendix D: A Note on Bragg Scattering of Surface Waves by Sinusoidal Bars

Appendix E: A Discrete Angular Spectrum Model for Nonlinear Shallow Water Waves. Part 1. Waves in Laterally Uniform Domains

Appendix F: Angular Spectrum Modelling of Water Waves



Accession For	
NTIS CRA&I	<input checked="" type="checkbox"/>
DTIC TAB	<input type="checkbox"/>
Unannounced	<input type="checkbox"/>
Justification	
By <i>per A225131</i>	
Distribution	
Availability Codes	
Dist	Avail and/or Special
<i>A-1</i>	

1 Summary

This document is the final report for the ONR project N00014-90-J-1678, the third phase of a study entitled "Modelling bathymetric control of near coastal wave climate" The effort in this phase of the study was concentrated on the extension of the angular spectrum modelling technique to nonlinear shallow water waves, and to further studies of the Bragg reflection mechanism for surface waves being reflected by artificial or natural bars.

Data from a laboratory experiment on the mean surfzone flows associated with a passively-driven syphon system is presently being reduced and will be described in a separate data report.

2 Bragg Reflection

The major effort in this area was related to describing the reflection process for bars with shapes that would correspond to artificial bars to be installed in the field. Appendix A contains a paper which describes the analysis of reflection from a bar field using the Fourier decomposition of the bar shapes in the analysis. Appendix B describes an attempted field installation (see Kirby, 1988) of bars of the type described in Appendix A. Finally, Appendix C assesses the usefulness of artificial bars as coastal protection devices. The analysis in this paper utilizes the bar selection program developed in Kirby (1987). Finally, Appendix D presents a manuscript which addresses some theoretical points arising in the analysis of resonant reflection of waves by sinusoidal bars.

3 Angular Spectrum Modelling

The development of the angular spectrum methodology for modelling nearshore wave propagation was extended to the case of nonlinear shallow water waves; this case is described in Appendix E. The work leading up to this point has culminated in an invited review article covering work on linear waves, nonlinear Stokes waves, and shallow water Boussinesq waves, which is presented here as Appendix F.

References

- Kirby, J. T., 1987, "A program for calculating the reflectivity of beach profiles", Report UFL/COEL-87/004, Coastal and Oceanographic Engineering Department, University of Florida, Gainesville.
- Kirby, J. T., 1988, "Survey Data Report: Cape Canaveral, March-July, 1988", Report UFL/COEL-88/011, Coastal and Oceanographic Engineering Department, University of Florida, Gainesville.

Appendix A: Bragg Reflection of Waves by Artificial Bars

Proc. 22nd Intl. Conf. Coastal Engrng., Delft, July 2-6, 1990.

CHAPTER 58

BRAGG REFLECTION OF WAVES BY ARTIFICIAL BARS

James T. Kirby¹, Jeffrey P. Anton²

Abstract

We consider the extension of previous theories for Bragg reflection of surface waves by parallel bars to the case of artificial bars placed discretely on the seabed. The case of non-resonant, weak reflection is considered first, followed by a consideration of the application of resonant interaction theory to the dominant Fourier mode of the bar field. Both theories are compared to numerical results, and discrepancies are seen in both cases. Finally, experimental results are compared to theory.

Introduction

The discovery that the Bragg reflection mechanism leads to strong reflection of incident surface waves by periodic bottom undulations has led to speculation that artificial bars could be constructed which would partially shelter shores or localized structures from wave attack. Possible bar configurations of this sort have been discussed previously by Mei et al. (1988) and Naciri and Mei (1988). The paper by Bailard et al. (1990) in this conference describes an effort which was made to install and test an artificial bar field offshore of a natural beach.

The purpose of the present study was to extend the scope of available theory and techniques which were available for predicting wave reflection from bars, in support of the proposed field study. Here, we discuss the application of analytic perturbation methods for both non-resonant and resonant cases. We also discuss numerical results, which point out limitations present in both analytic approaches. Finally, experimental results largely provide a qualitative verification but in turn show some limitation of the small amplitude bar theory.

Theory for Small Amplitude Bars

The theory which provides the framework for analysis here is given by an extended mild-slope equation derived by Kirby (1986).

We treat the water depth $h'(x, y)$ as the superposition of a mildly-sloping bottom $h(x, y)$ and a rapidly-varying but small-amplitude undulation $\delta(x, y)$:

$$h'(x, y) = h(x, y) + \delta(x, y) \quad (1)$$

¹Assoc. Prof., Center for Applied Coastal Research, Dept. of Civil Engrg., Univ. of Delaware, Newark, DE 19716

²Formerly, Grad. Stud., Coastal and Oceanographic Engineering Department, University of Florida, Gainesville, FL 32611

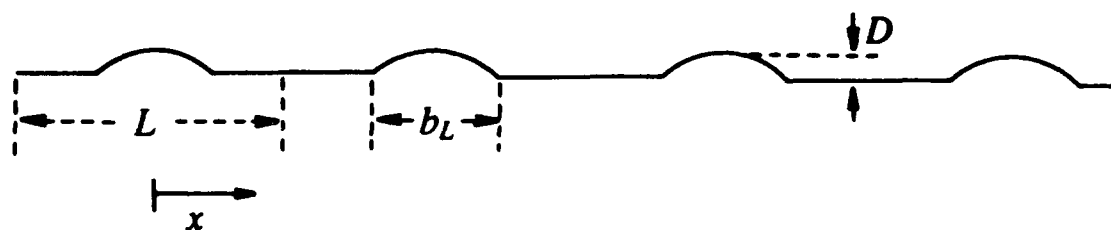


Figure 1: Bar field with four discrete bars.

Using $h(x, y)$ as the reference depth in the mild-slope sense, the model equation

$$\nabla_h \cdot (CC_g \nabla_h \phi) + k^2 CC_g \phi = \frac{g}{\cosh^2 kh} \nabla_h \cdot (\delta \nabla_h \phi) = 0 \quad (2)$$

is obtained, where ϕ is the value of the linear wave potential at the still water surface. The model coefficients are obtained from

$$\omega^2 = gk \tanh kh ; C = \frac{\omega}{k} ; C_g = \frac{\partial \omega}{\partial k} \quad (3)$$

and are determined by the value of $h(x, y)$ in all cases.

The Artificial Bar Field

In the absence of appropriate field data, we have restricted our attention here to the study of periodically spaced bars ($\delta = \delta(x)$) and an otherwise uniform depth $h = \text{constant}$. In principal, δ is arbitrary aside from the small amplitude restriction. In the present study, we have chosen a bottom consisting of rectified sine waves, given by

$$\delta(x) = \begin{cases} D \cos \frac{\pi}{b_L} (x - NL) ; & NL - \frac{b_L}{2} \leq x \leq NL + \frac{b_L}{2} \\ 0 & \text{otherwise} \end{cases} \quad (4)$$

$N = 0, \dots, N_b - 1$

where N_b is the number of bars, L is the periodic bar spacing, b_L is the footprint of the bar on the bottom, and D is the bar height. The rectified cosine form is chosen mainly for its convenience in later analysis. An example bar field is shown in Figure 1. The bar field is periodic over intervals of width L , and can be conveniently represented by the cosine series,

$$\delta(x) = \sum_{n=0}^{\infty} D_n \cos(n\lambda x) ; \quad \lambda = \frac{2\pi}{L} \quad (5)$$

where

$$D_0 = \frac{D}{\pi} ; D_1 = -\frac{D}{2} ; D_n = D \frac{\cos\left(\frac{n\pi}{2}\right)}{\pi(1-n^2)} (1 + \cos n\pi) \quad (6)$$

Non-resonant Reflection

For the case of h constant, the model equation (2) may be written as

$$\nabla_h^2 \phi + k^2 \phi = \alpha \nabla_h \cdot (\delta \nabla_h \phi) \quad (7)$$

where

$$\alpha = \frac{4k}{2kh + \sinh 2kh} \quad (8)$$

With $\delta(x)$ representing bars varying in the x -direction, we represent oblique waves according to

$$\phi(x, y) = \tilde{\phi}(x) e^{im y}; \quad m = k \sin \theta \quad (9)$$

and obtain

$$\begin{aligned} \tilde{\phi}_{xx} + \ell^2 \tilde{\phi} &= \alpha (\delta \tilde{\phi}_x)_x - m^2 \alpha \tilde{\phi}, \\ \ell^2 &= k^2 - m^2 = k^2 \cos^2 \theta \end{aligned} \quad (10)$$

This equation has been obtained by Miles (1981) who used it to study reflection from a single isolated obstacle.

For $\delta(x)$ confined in a finite region of space, we may write

$$\begin{aligned} \tilde{\phi}(x \rightarrow \infty) &= T e^{i\ell x} \\ \tilde{\phi}(x \rightarrow -\infty) &= e^{i\ell x} + R e^{-i\ell x} \end{aligned} \quad (11)$$

where T and R are complex transmission and reflection coefficients. With δ small, we expand $\tilde{\phi}$, T and R as series in the small parameter $\epsilon = D/h$, and obtain

$$\phi_0 = e^{i\ell x} \quad R_0 = 0 \quad T_0 = 1 \quad (12)$$

at leading order. At second order, the reflection coefficient R_1 for an arbitrary topography $\delta(x)$ is

$$R_1 = -\frac{i\alpha}{2\ell} (\ell^2 - m^2) \int_{-\infty}^{\infty} \delta(x) e^{2i\ell x} dx \quad (13)$$

as found by Miles (1981). Note that R_1 is singular in the limit as $\theta \rightarrow \pi/2$. This effect has not been previously noted and its practical implications are unclear.

For the case of a simple sinusoidal bottom

$$\delta(x) = D \sin(\lambda x); \quad 0 \leq x \leq N_b L \quad (14)$$

we obtain the expression

$$|R| = \begin{cases} \frac{\alpha D}{2} \left(\frac{\ell^2 - m^2}{\ell^2} \right) \frac{2\ell/\lambda}{2\ell^2 - 1} \left| \sin \left(\frac{2\ell}{\lambda} \pi N_b \right) \right|; & \frac{2\ell}{\lambda} \neq 1 \\ \frac{\alpha D}{2} \left(\frac{\ell^2 - m^2}{\ell^2} \right) \frac{\pi N_b}{2}; & \frac{2\ell}{\lambda} = 1 \end{cases} \quad (15)$$

This result extends the non-resonant theory of Davies and Heathershaw (1984) to include obliquely incident waves.

For the periodic bar field described by (5) and (6), we substitute (5) in (13) and obtain the expression

$$R_1 = \frac{-i\alpha}{2} \left(\frac{\ell^2 - m^2}{\ell} \right) \sum_{n=0}^{\infty} D_n I_n, \quad (16)$$

where the integrals I_n are given by

$$I_n = \int_{-\frac{L}{2}}^{(N_b-1)L+\frac{L}{2}} \cos(n\lambda x) e^{2i\ell x} dx. \quad (17)$$

As in the case of a single sinusoidal bar, the integral I_n takes on special values when $2\ell/n\lambda = 1$ for the corresponding value of n . We further simplify the notation by setting

$$\gamma = \frac{2\ell}{\lambda} \quad (18)$$

Then, for $\gamma \neq n$, we obtain the expression

$$I_n(\gamma) = \frac{\gamma^2}{\ell(\gamma^2 - n^2)} e^{i\ell N_b L} \sin \ell N_b L; \quad \gamma \neq n \quad (19)$$

For $n = \gamma$, we obtain the expression

$$I_n(\gamma = n) = \frac{N_b L}{2} \quad (20)$$

We thus obtain the general solution for obliquely incident waves

$$R_1 = -\frac{i\alpha}{2} \left(\frac{\ell^2 - m^2}{\ell^2} \right) \left\{ \sum_{n=0, \gamma \neq n}^{\infty} \frac{\gamma^2 D_n}{(\gamma^2 - n^2)} e^{i\ell N_b L} \sin \ell N_b L + D_n \delta(n - \gamma) \frac{\ell N_b L}{2} \right\} \quad (21)$$

where $\delta(n - \gamma)$ is the delta function, and there $n = \gamma$ can only occur for one wavenumber component for a fixed value of ℓ . For the case of normally incident waves (studied further below), we let $\ell \rightarrow k$, $m \rightarrow 0$ and obtain

$$R_1 = -\frac{i\alpha}{2} \left\{ \sum_{n=0}^{\infty} \frac{\gamma^2 D_n}{(\gamma^2 - n^2)} e^{ik N_b L} \sin k N_b L + D_n \delta(n - \gamma) \frac{k N_b L}{2} \right\} \quad (22)$$

From the form of the solution, it is apparent that each harmonic of the bar field contributes to the reflection process, with the dominant contribution of the n^{th} harmonic coming from the neighborhood $\lambda \approx n$. An example plot of reflection coefficient $|R_1|$ is shown in Figure 2 for a case of 4 bars with crest-to-crest spacing equal to the unrectified wavelength ($b_L = L/2$). Waves are normally incident on the bar field. The peak in $|R_1|$ at $2k/\lambda = 1$ corresponds to the usual Bragg interaction between the surface wave and the fundamental harmonic of the bar field, when the surface wave length is twice the bar spacing. A second prominent peak is located at $2k/\lambda = 2$, corresponding to a surface wavelength equal to twice the length of the second harmonic of the bar field (and thus equal in length to the bar spacing). This strong second peak is absent when the bar

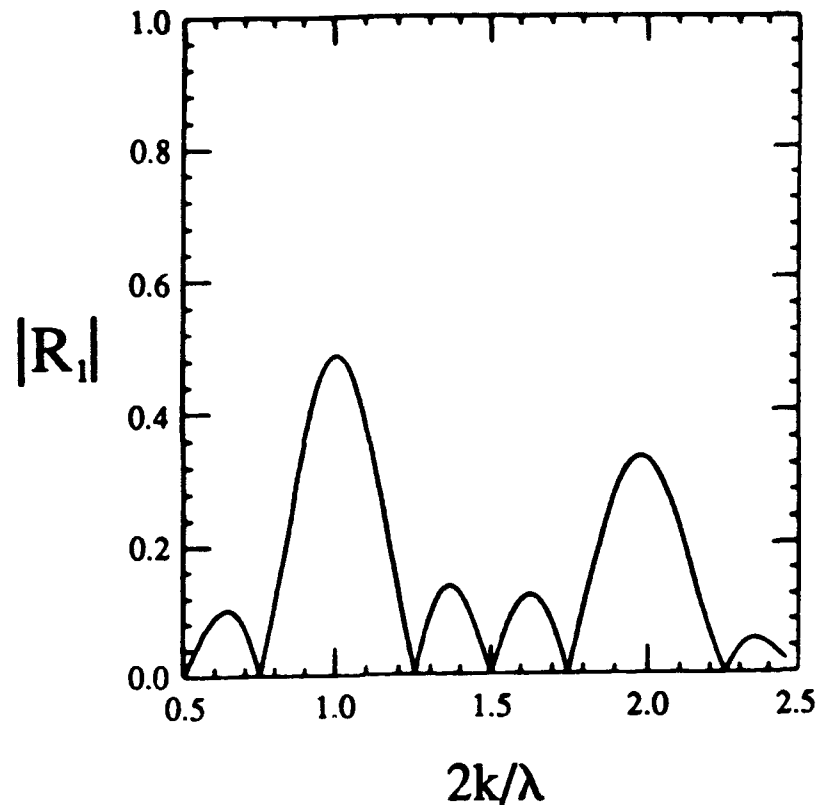


Figure 2: Reflection for four discretely placed bars. Non-resonant theory, equation (22).

field being considered is a simple sinusoid, as in Davies and Heathershaw (1984) and Mei (1985).

In general, the relative amplitude of the peaks in the reflection coefficient may be adjusted by changing the spacing of artificial bars, assuming the cross-section of each bar to stay the same. Pushing bars closer together makes the bar field more sinusoidal and reduces the importance of higher harmonics. Placing the bars further apart makes them into relatively more "solitary" features, and thus emphasizes the relative importance of higher harmonics. Two cases illustrating these extremes were investigated in the experiments described below.

Resonant Reflection

The reflection coefficient described in (21) is defective for the cases $2\ell \approx n\lambda$, where the coefficient can become arbitrarily large as $N_b \rightarrow \infty$. While this limit would never be reached in practice, the result shows that the theory is not strictly valid in the neighborhood of the resonances. The problem lies with assuming that R_1 is $O(1)$ in the perturbation series used above. Mei (1985) has developed a resonance theory which allows for $O(1)$ reflection in the neighborhood of each resonance. Mei et al. (1988) further suggested that, for the case of a bar field with multiple Fourier components, the reflection could be estimated using the resonance theory applied to the Fourier mode corresponding to the bar wavelength. This approach would not account for the occurrence of multiple strong peaks. In the present study, we define a neighborhood of each resonance $2\ell/\lambda = n$ to be the range $n - 1/2 \leq 2\ell/\lambda \leq n + 1/2$. Then, in each range, Mei's theory is used with $2\ell/\lambda^*$ replacing $2\ell/\lambda$, with $\lambda^* = n\lambda$. We refer the reader to Mei (1985) for the expressions defining the reflection coefficients. The only necessary modification to the theory account for oblique incidence and the presence of multiple resonant peaks. The frequency ω_n of the n^{th} resonant peak is given by

$$\omega_n^2 = \frac{gn\lambda}{2 \cos \theta} \tanh \left(\frac{n\lambda h}{2 \cos \theta} \right) \quad (23)$$

The cutoff condition Ω_0 defined by Mei is replaced by

$$\Omega_{0n} = \frac{\ell^2 - m^2}{\ell^2} \frac{\omega_n k D_n}{2 \sinh 2kh} ; \quad k = \frac{\ell}{\cos \theta} \quad (24)$$

where the D_n are the amplitudes of the bar Fourier coefficients, and there Ω_{0n} refers to the n^{th} resonant peak.

An example of the reflection calculated for the case of normal incidence is given in the following section, in comparison with numerical results and results of the non-resonant theory.

Numerical Solutions

In order to study the validity of each of the perturbation solutions, direct numerical solutions of equation (10) were also performed. For a bar field in the region $0 \leq x \leq N_b L$, an incident wave boundary is established at $x = A < 0$, and a downwave, transmitting boundary is established at $x = B > N_b L$. For an incident wave $\tilde{\phi}_I = e^{i\ell x}$, the appropriate boundary conditions are

$$\tilde{\phi}_x = \begin{cases} i\ell(2\tilde{\phi}_I - \tilde{\phi}) ; & x = A \\ i\ell\tilde{\phi} ; & x = B \end{cases} \quad (25)$$

Equations (10) and (25) are finite-differenced using central differences, leading to a tridiagonal system which is solved using the Thomas algorithm.

Figure 3 shows a sample of calculated reflection coefficients obtained with the numerical solution and the two analytic solutions, for the bar field described in Figure 2. As expected, the non-resonant solution over-predicts reflection at $2k/\lambda = 1$, in comparison with the resonant theory of Mei (1985). The discrepancy is relatively minor at the second peak $2k/\lambda = 2$, where the resonance is relatively weaker. In contrast to both analytic theories, the numerical results

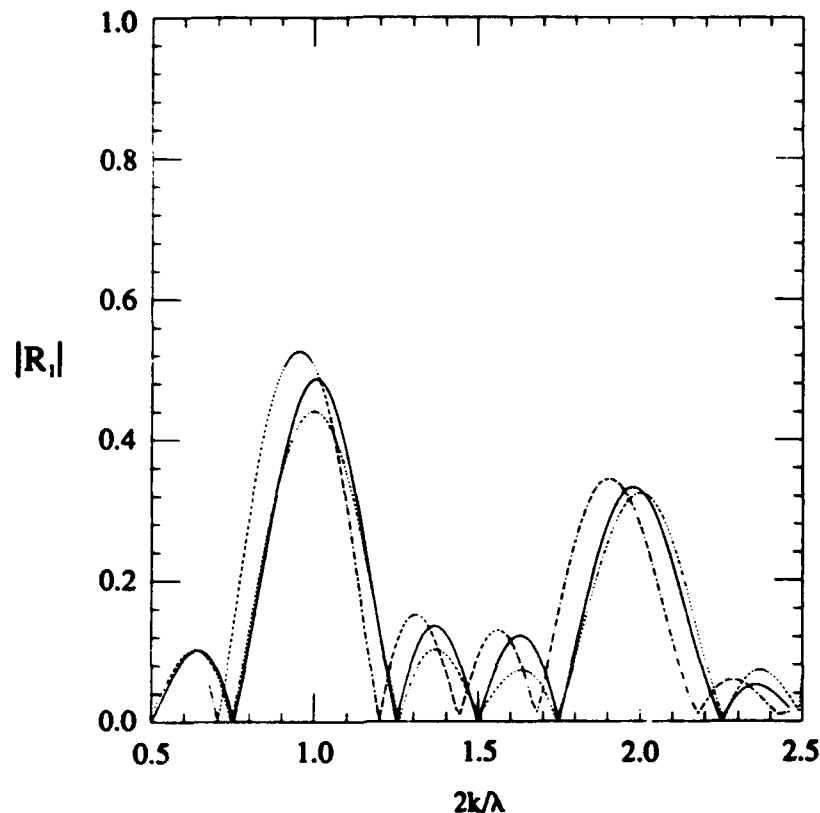


Figure 3: Comparison of non-resonant, resonant and numerical solutions for a bar field with $N_b = 4$. —, non-resonant theory; ---, resonant theory; - · -, numerical results.

show a strong downshift of the reflection peaks to lower values of $2k/\lambda$. This downshift is related to the simultaneous interaction between the wave field and several bottom modes; a similar effect occurs for the case of a sinusoidal bar field, but it is much more subtle. The numerical scheme also predicts a higher reflection coefficient at each peak. The large downshifts and higher peaks are largely validated by data described below. These results indicate that either of the two analytic solutions are at best qualitatively accurate when used to describe reflection from the type of bars that could be built in an actual construction project.

Experimental Results

Experiments were conducted in the 60 cm wide wave flume in the Coastal and Oceanographic Engineering Laboratory, University of Florida, in order to verify the basic aspects of the theory for normally incident waves. For the experiments, a water depth $h = 15$ cm was used. Bar height D was 5 cm, giving $D/h = 0.33$, which is relatively large and could contribute to some of the discrepancies between theory and data noted below. The bar footprint $b_L = 50$ cm. Two bar spacings, $L = 80$ cm and 120 cm, were tested, corresponding to cases with bar field higher harmonics of low importance and great importance,

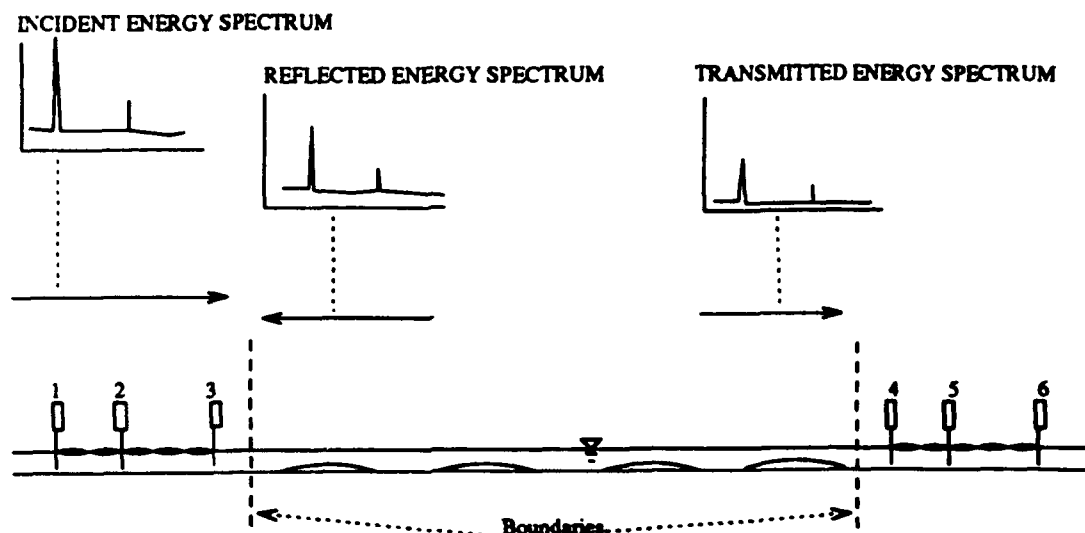


Figure 4: Bar field and wave gage placement

respectively. The bar fields tested contained four discrete bars.

In order to maintain a close correspondence between the assumed linearity of the wave theory and the experiments, incident waves on the order of 1 cm in height were generated. (Actual height varied with wave frequency, as would be expected from wavemaker theory.) Wave heights were measured using capacitance wave gages mounted with 6 cm-long wires, which were calibrated over their full length. Data was sampled using 12-bit digitization, giving a resolution of 0.012 mm/division. The wavefield was sampled at a 10 Hz frequency, with experimental waves being generated in the range $0.4 \text{ Hz} \leq f \leq 1.6 \text{ Hz}$.

Due to the small wave heights being used, there was an additional source of noise in the data associated with mechanical vibration in the wavemaker and other high-frequency effects. In retrospect, it would be better to use slightly higher waves in future experiments unless great care were taken to isolate mechanical vibration. (For a particularly spectacular example of clean data in a related low-amplitude wave experiment, see Benjamin et al. (1989)).

The three-gage, least squares method developed by Funke and Mansard (1980) was used to separate incident and reflected waves. The gage layout relative to the bar field is shown in Figure 4. The incident-reflected separation was performed both upwave and downwave of the experimental bar field. The downwave separation indicated a reflection from the absorbing beach on the order of 5-6%. This reflected energy was neglected in subsequent processing and the downwave region was assumed to be perfectly transmitting.

Figure 5 shows the measured reflection coefficient for the case of $L = 80 \text{ cm}$, when bar field harmonics are relatively unimportant. Also included in the figure is the prediction of the numerical model described in the previous section. The data largely validates the theory, although there is a great deal of scatter. (It also appears that shifting the data to higher values of $2k/\lambda$ would bring the data into fairly close agreement with theory. No systematic error was ever detected in the experimental procedure which could account for such a shift, unfortunately.)

Figure 6 shows corresponding data for the case of $L = 120 \text{ cm}$, where the

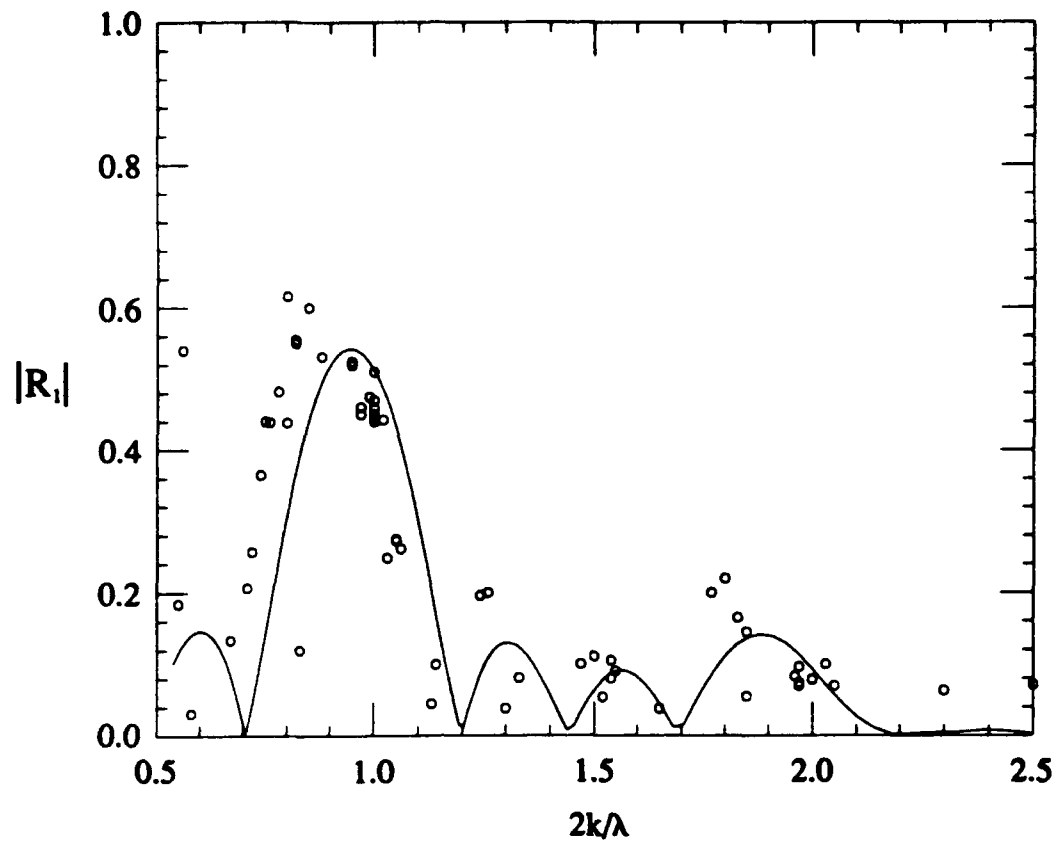


Figure 5: Experimentally measured reflection coefficient, $L = 80cm$.

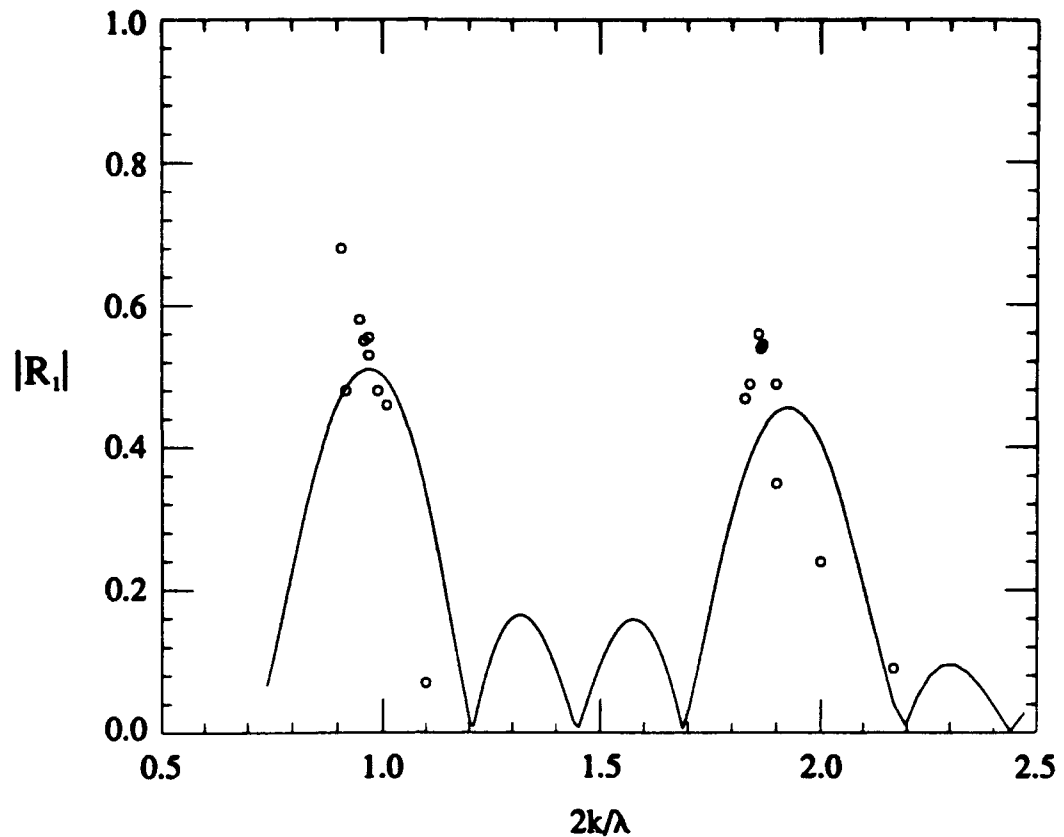


Figure 6: Experimentally measured reflection coefficient, $L = 120\text{cm}$.

second harmonic component of the bar field is comparable in height to the fundamental harmonic. Due to time constraints, the data here is relatively sparse, and tests were grouped in order to show the relative heights of the two reflection peaks. Both the presence and the relative importance of the two numerically-predicted peaks are substantiated by the data.

Response of a Closed-end Channel

One question that arises in response to the realization that bars can reflect significant amounts of incident energy is whether or not a region downwave of a bar field experiences a less severe wave condition than the region on the incident site. The answer to this question can be positive or negative, depending on the geometry of the downwave region and the reflectivity of the end boundary. For cases where reflection from the end wall is nearly complete, waves travelling back towards the bar field are partially re-reflected into the sheltered region. The possibility of resonating the sheltered region exists, as does the possibility of reducing the wave activity, and depends primarily on whether the sheltered region contains an integer multiple of one-half the surface wavelength.

Figure 7 shows the numerically predicted amplitude at a vertical wall situated four barfield wavelengths downwave of a bar field with four bars, as in the previous examples. The incident wave has an amplitude of unity, and so an amplitude of 2 represents simple reflection. The figure shows that the amplitude at the wall can reach as high as 3.6 and as low as 1, representing a range of

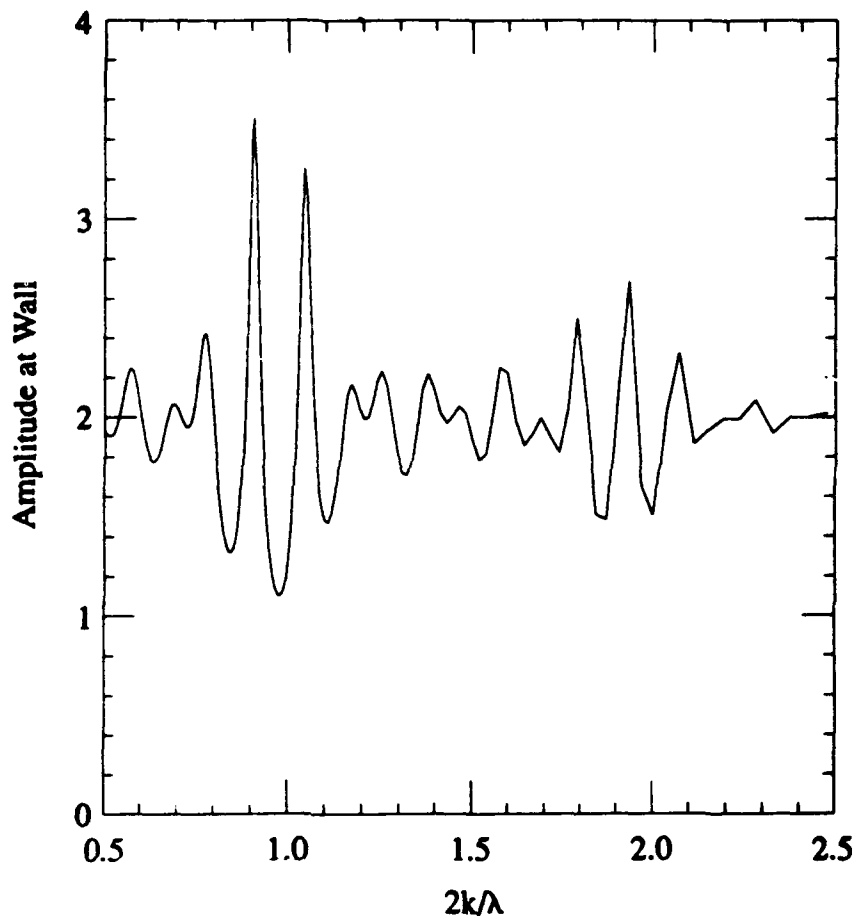


Figure 7: Wave Amplitude at End Wall of a Channel Sheltered by an Artificial Bar Field

resonance and sheltering conditions.

For the case where the channel end is primarily absorbing (due to wave breaking or frictional effects), the possibility of resonating the sheltered region is greatly reduced. This virtually guarantees that a bar field designed to shelter a beach from wind-wave band waves would not resonate the shoreline. However, as the wave frequency becomes low, even a mildly-sloped shoreline can become essentially reflective. It is thus possible that broad, low bars contribute significantly to amplifying long wave energy on the beach face. The long waves that could be amplified or resonated by this mechanism may be locally generated by nonlinear processes in the surfzone, or they may be arriving as part of the forced or free long wave climate incident from offshore. Problems of this sort need further investigation to determine the relative importance of bottom interaction in influencing the nearshore wave climate.

Acknowledgements

The work described in this paper was supported by the Office of Naval Research and the Naval Civil Engineering Laboratory through contracts N00014-86-K-0790 and N00014-89-J-1717. Both authors were affiliated with the Coastal and Oceanographic Engineering Department, University of Florida at the start of this study; use of the facilities there is greatly appreciated. Conversations with Jim Bailard, Bob Guza, and Dan Hanes were instrumental in the early stages of problem formulation.

References

- Baillard, J., DeVries, J., Kirby, J.T. and Guza, R.T., 1990, "Bragg reflection bars: A new shore protection concept?" *Proc. 21st Int'l. Conf. Coastal Engrg.*
- Benjamin, T.B., Boczar-Karakiewicz, B. and Pritchard, W.G., 1987, "Reflection of water waves in a channel with corrugated bed," *Journal of Fluid Mechanics*, 185, 249-274.
- Davies, A.G. and Heathershaw, A.D., 1984, "Surface-wave propagation over sinusoidally varying topography," *Journal of Fluid Mechanics*, 144, 419-433.
- Funke, E.R. and Mansard, E.P.D., 1980, "Measurement of incident and reflected spectra using a least squares approach," *Proc. 17th Int'l. Conf. Coastal Engrg.*, 1, 154-172.
- Kirby, J.T., 1986, "A general wave equation for waves over rippled beds," *Journal of Fluid Mechanics*, 162, 171-186.
- Mei, C.C., 1985, "Resonant reflection of surface water waves by periodic sand-bars," *Journal of Fluid Mechanics*, 152, 315-335.
- Mei, C.C., Hara, T. and Naciri, M., 1988, "Note on Bragg scattering of water waves by parallel bars on the seabed," *Journal of Fluid Mechanics*, 186, 147-162.
- Miles, J.W., 1981, "Oblique surface-wave diffraction by a cylindrical obstacle," *Dynamics of Atmospheres and Oceans*, 6, 121-123.
- Naciri, M. and Mei, C.C., 1988, "Bragg scattering of water waves by a doubly periodic seabed," *Journal of Fluid Mechanics*, 192, 51-74.

Appendix B: Bragg Reflection Breakwater: A New Shore Protection Method?

Proc. 22nd Intl. Conf. Coastal Engrng., Delft, July 2-6, 1990.

**Bragg Reflection Breakwater: A New
Shore Protection Method?**

**James A. Bailard¹, Jack DeVries², James T. Kirby³
and Robert T. Guza⁴**

ABSTRACT

The feasibility of a new type of breakwater is explored through a combined program of theoretical analysis, laboratory experiments and a prototype field test. The breakwater consists of a series of low height, shore-parallel bars which are placed just outside the surf-zone. The incident wave field is strongly reflected when the incident wave length is equal to twice the distance between adjacent bars. The breakwater acts to shelter the beach against storm wave attack and to build a tombolo sand deposit behind the breakwater. Theoretical and laboratory studies indicated that the Bragg reflection breakwater concept may have considerable merit, however, a small scale field test served to demonstrate the many practical difficulties in implementing the concept.

INTRODUCTION

The Naval Civil Engineering Laboratory (NCEL) has been involved in a multi-institutional program to explore low cost, rapidly deployable techniques for reducing beach erosion during storms. One concept under consideration is the Bragg reflection breakwater. Theoretical and

¹ Principal, Bailard Jenkins Technologies, Carpinteria, CA

² Engineer, Naval Civil Engineering Lab, Port Hueneme, CA

³ Professor, University of Delaware, Newark, DE

⁴ Professor, Scripps Institution of Oceanography, La Jolla, CA

laboratory studies have shown that a series of periodically spaced, low height bars, oriented parallel to the beach, can produce a strong reflection of the incident wave field. A resonant condition (termed Bragg reflection) occurs when the incident wave length is equal to twice the separation distance between bars.

The Bragg reflection breakwater concept involves placing a series of artificial bars just outside the surfzone. Referring to Figure 1, the effect of the bar field is two-fold: to shelter the beach from storm wave attack; and, to create a large sand volume behind the breakwater by way of the induced nearshore circulation. Both effects serve to protect the beach against storm wave attack: the first by reducing the rate of offshore sand transport, the second by increasing the erodable sand volume.

The objective of the research program was to explore the feasibility of the Bragg reflection breakwater concept through a combined program of numerical and laboratory modeling and a prototype field test. The present paper presents an overview of the program with an emphasis on the planning and results of a small scale field experiment.

BACKGROUND

Theoretical and Experimental Basis

Davies and Heathershaw (1984), Mei (1985) and others have shown that a series of low amplitude sinusoidal undulations on the seabed can be an effective reflector of surface gravity waves. The reflected wave energy varies as a function of the ratio of the incident wave length to the spacing between bottom undulations. A resonant condition, termed Bragg reflection, occurs when the incident wave length is equal to twice the distance between undulations. When resonance occurs, a small number of bars can reflect a substantial portion of the incident wave energy.

Technical Issues

At the onset of the research program, there were a number of unresolved technical issues relating to the feasibility of the Bragg reflection breakwater concept. These included: the response characteristics of non-sinusoidal bars on a sloping beach; the effects of finite bar length and the resulting wave-induced circulation; the morphological response of the beach in the presence

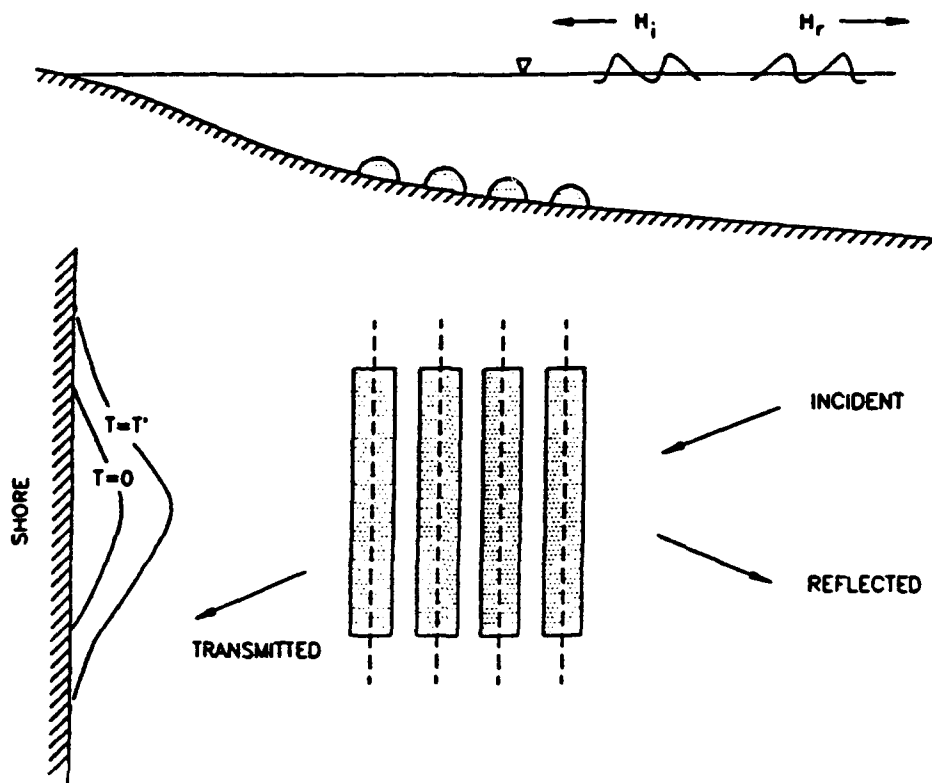


Figure 1. Schematic drawing of Bragg reflection breakwater concept.

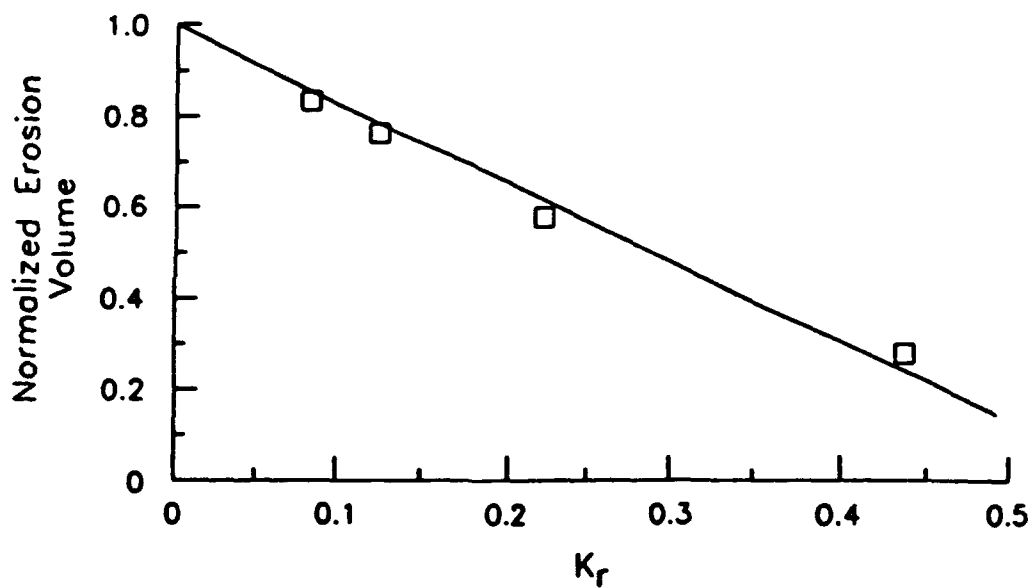


Figure 2. Beach profile response model results.

of the breakwater; the practical design, installation and recovery of a breakwater; and, the effects of waves on bar stability and scour. An additional issue was how to measure spectral wave reflection in the field.

PRELIMINARY ASSESSMENT

As a means of exploring the feasibility of the Bragg reflection breakwater concept, a series of preliminary studies were conducted. These studies were to culminate in a small scale field test of the concept. The results of the preliminary studies can be summarized as follows.

Wave and Current Modeling

Numerical and laboratory modeling studies were conducted at the University of Florida to examine the effects of bar shape, bar placement, beach slope and bar length on the reflection characteristics of a Bragg reflection breakwater. Details of these studies may be found in Anton et al. (1990). Specific results included:

- o The primary effect of beach slope is to require an adjustment in the spacing between each bars to accommodate the change in incident wave length.
- o The reflection from a non-sinusoidal bar field can be calculated by expanding the bottom shape function as a fourier series and linearly summing the response characteristics for each component of the series.
- o Finite bar length causes a longshore variation in the wave-induced setup leading to the formation of a rip current flowing outward over the bar field. The rip current acts to broaden the resonant peak.

These studies indicated that a Bragg reflection breakwater, constructed from a small number of practical-shaped (i.e. non-sinusoidal) bars, could be expected to generate a reflection coefficient in the range of 0.2 to 0.4.

Beach Response Modeling

A Bragg reflection breakwater protects a beach from storm wave attack by reducing the rate of offshore sand transport via decreased wave height and increasing the erodable sand volume via creation of a tombolo behind the breakwater. The former is a two-dimensional effect which is independent of breakwater length. The latter is a three-dimensional effect which results from the formation of a nearshore circulation cell with a rip current flowing outward over the top of the breakwater.

NCEL conducted a numerical model study to determine the impact of a Bragg reflection breakwater on the two-dimensional response of a beach profile during a simulated storm. The model study utilized an energetics-based beach profile response model developed by DeVries and Bailard (1988). The model was run for a simulated 5 day storm assuming varying wave reflection coefficients. The effectiveness of the breakwater was expressed in terms of the normalized erosion volume. This was defined as the ratio of the eroded sand volume in the presence of the breakwater divided by the eroded sand volume without the breakwater.

Model inputs were as follows:

- o Initial equilibrium beach slope = 0.03
- o Grain size = 0.4 mm
- o Storm duration = 72 hr
- o Peak wave height = 2 m
- o Peak wave period = 9 sec

Without the breakwater, the beach eroded approximately 205 cubic meters per meter of beach. Referring to Figure 2, the breakwater reduced the storm erosion volume by an amount which was inversely proportional to the wave reflection coefficient, K_r . The degree of reduction is quite significant, amounting to 35% for a reflection coefficient of 0.2.

A movable bed physical model study was conducted at the University of Florida to qualitatively examine the three-dimensional beach changes induced by a Bragg reflection breakwater. The model confirmed the presence of a nearshore circulation cell with a rip current flowing outward over the bar field. The circulation cell caused a tombolo to form behind the breakwater, with the outer edge of the tombolo perched on the shoreward-most bar.

Bar Module Tests

It was anticipated that developing a practical breakwater would be a significant design challenge. Our limited budget necessitated coming up with a breakwater which could be rapidly assembled, installed and recovered using a minimum of people and equipment. In order to explore various design and installation concepts, NCEL conducted field tests of two bar designs at a Port Hueneme beach. Both designs featured modular constructions consisting of skid-mounted bar modules which could be assembled on the beach and dragged offshore.

Referring to Figure 3, the first design consisted of a geotextile bag attached to a skid-mounted steel frame. The concept was to drag the modules into place with the bags empty, and then fill the bags with sand using a small dredge pump. When the breakwater was no longer needed, the bags could be slit, allowing the sand to disperse and the bars dragged back ashore. The advantage of this design was that the bar modules would be light and easy to move when empty, but heavy and difficult to move when full.

An attempted field test of the geotextile bar design ended in failure. Although assembling and positioning the bar module proved simple, filling the geotextile bag with a small dredge pump proved difficult. The pump was mounted on an amphibious LARC vehicle, parked in the surfzone. The principal difficulties were maintaining an adequate supply of sand to the pump and handling the intake and discharge hoses. When, after a few hours of filling, little sand had been pumped into the bag, the test was abandoned. In retrospect, the test might have been more successful had a larger, perhaps land-based dredge pump had been used. Nevertheless, the installation procedure was judged to be too cumbersome for the planned field experiment.

Referring to Figure 4, the second bar module design consisted of a corrugated steel arch attached to a skid-mounted steel frame. The concept was to assemble the modules on the beach and drag then into position. When the breakwater was no longer needed, the modules would be dragged back onto the beach and removed. The advantage of this design was that the modules were ready to go once they were moved into position. The main drawback was that the modules were relatively light weight and could be moved about by large waves. Although pinning the modules with uplift resisting anchors was considered, it was judged unnecessary for the anticipated wave climate.

The field test demonstrated that the arch module design could be rapidly assembled and installed. Provided wave heights were less than 1 m (rms), the module tended to remain in place. The primary problem was a scouring of the seabed underneath the bar module. This was caused by wave-induced flow passing through the narrow gap between the leading and trailing edges of the bar and the sand bottom. The scour depression acted to further enhance the venting flow, reducing the reflectivity of the bar module.

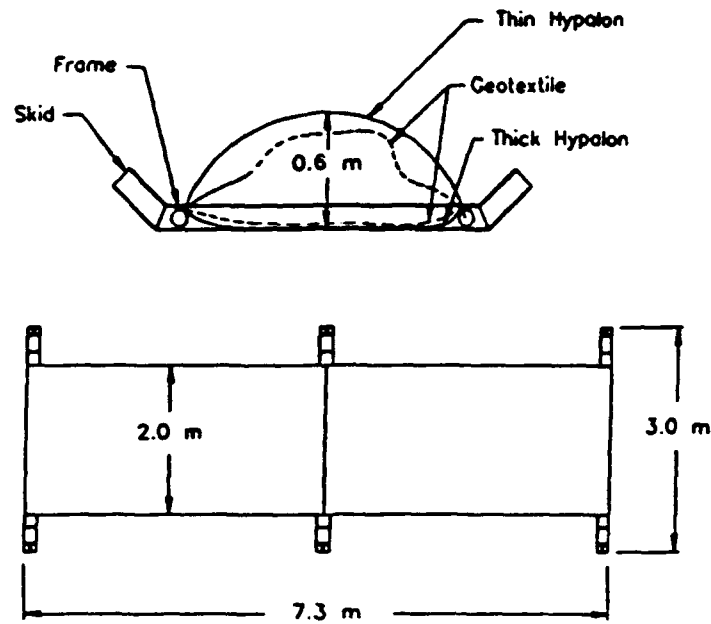


Figure 3. Geotextile bar module design.

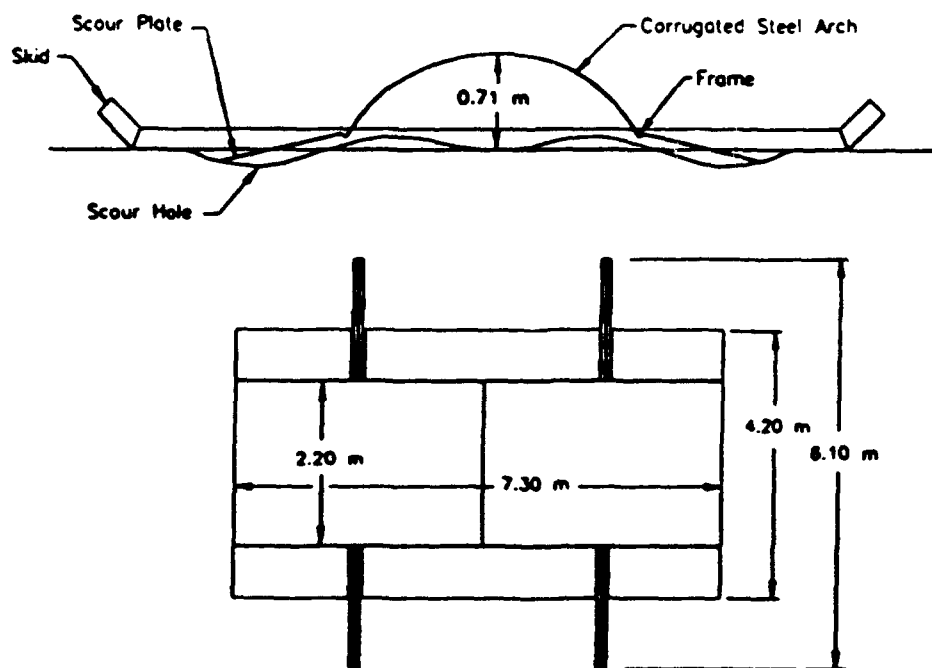


Figure 4. Steel arch bar module design used in the field test.

The venting/scour problem was solved by adding steel plates to the leading and trailing edges of the bar. The plates were attached to the bar by hinges, effectively sealing off the gap underneath the bar. Although some scour continued to occur around the bar module, the plates continued to function by dropping down into the scour depressions. After a period of two days, the scour depressions appeared to stabilize at a depth of about 0.3 m. A few days later, a significant storm passed through the area destroying the bar modules. However, the successful performance of the module prior to the storm convinced us that the steel arch design would be suitable for the planned field test.

Detection Method

An inverse method was developed to estimate the directional spectrum of the reflected wave field (see Herbers and Guza, 1990). The method requires simultaneous measurement of the incident wave field at a point offshore and the reflected wave field at a point immediately in front of the Bragg reflection breakwater. The procedure is as follows:

- o The incident wave field is estimated using the offshore wave measurements.
- o The incident wave field is transformed to shallow water using linear refraction.
- o The reflected wave field is estimated using the inshore wave measurements and subject to maximum compatibility with the refracted incident wave field.

PROTOTYPE FIELD TEST

Site Selection

In order to maximize the detectable reflected wave energy, we wanted to construct a breakwater that was significantly longer than the incident wave length and which produced a reflection coefficient of about 0.4. To minimize the size of the breakwater and therefore its cost, we decided to carry out our experiment in "super laboratory" conditions. These can be defined as significant wave heights less than 0.25 m, a wave period of about 5 seconds and an installation depth of about 1.5 meters.

A number of sites were considered for the field experiment. The desired site required small amplitude, short period waves, a long planar beach, limited public access

and good logistical support. Based on these criteria, Cape Canaveral Beach, Florida, was selected as the preferred site for the field experiment. The site was located within the confines of Cape Canaveral Air Force Base, limiting public access and providing the necessary logistical support. Two years of wave data from the site indicated that during the month of July, we could expect significant wave heights of about 0.2 m with a 5 second period.

Breakwater Design

Referring to Figure 5, the prototype Bragg reflection breakwater was composed of three bars, 90 meters long. The offshore and middle bars were 0.7 meters high and 2.2 meters wide. The inner bar was 0.6 meters high and 2.4 meters wide. The spacing between the outer and middle bar was 9 meters versus 8 meters between the middle and inner bars. The breakwater was designed to be installed in a water depth of about 0.76 meters MLW.

Referring to Figure 5, each bar module was 7.3 meters long. The modules were fabricated from a pair of corrugated steel arches attached to a steel skid-mounted frame. The frame was composed of a pair of steel angle members attached to two steel skid beams. The angle members served as attachment points for the edges of the corrugated steel arches and the a series of steel scour plates hinged to the front and rear edges of the bar. The bar modules were designed to be assembled by a small crew using a crane and hand tools. Assembly was facilitated by prefabricating the components off-site and using nuts and bolts for fasteners.

The total weight of the bar modules was approximately 3300 lb. An stability analysis indicated that the modules would remain in place without anchoring if rms wave heights were less than 1 m (assuming a wave period of 5 to 6 sec).

Anticipated Performance

Figure 6 shows a plot of the estimated reflection characteristics for the prototype breakwater. These characteristics were estimated using a computer program developed by Kirby (1987). The response function shows a broad peak centered at about 6 seconds with a reflection coefficient value of 0.4. The adjacent narrower peak is the first harmonic resulting from the non-sinusoidal shape of the bar field (i.e. discrete bars resting on a planar bottom).

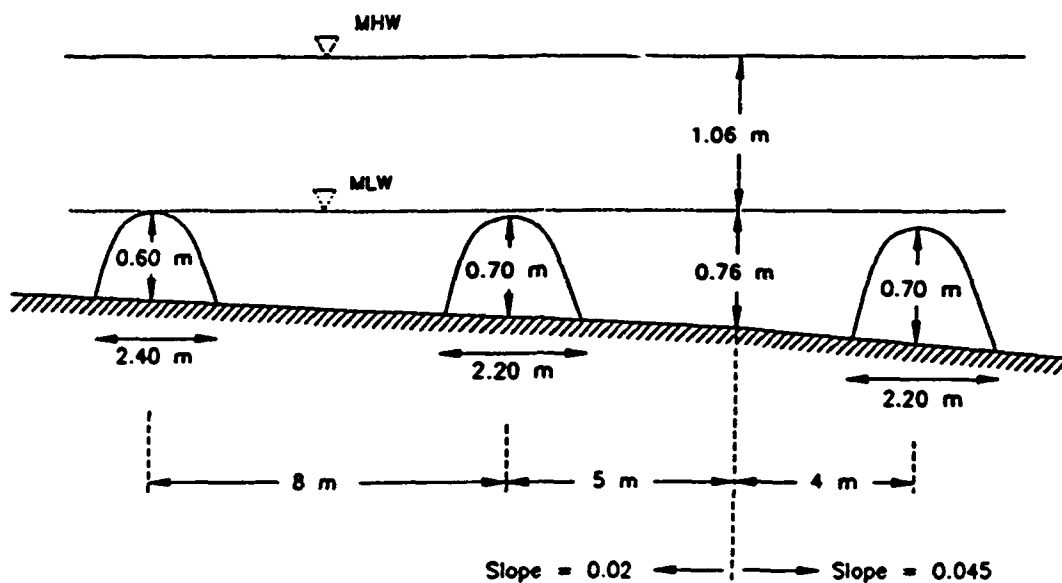


Figure 5. Bragg reflection breakwater design used in the field test.

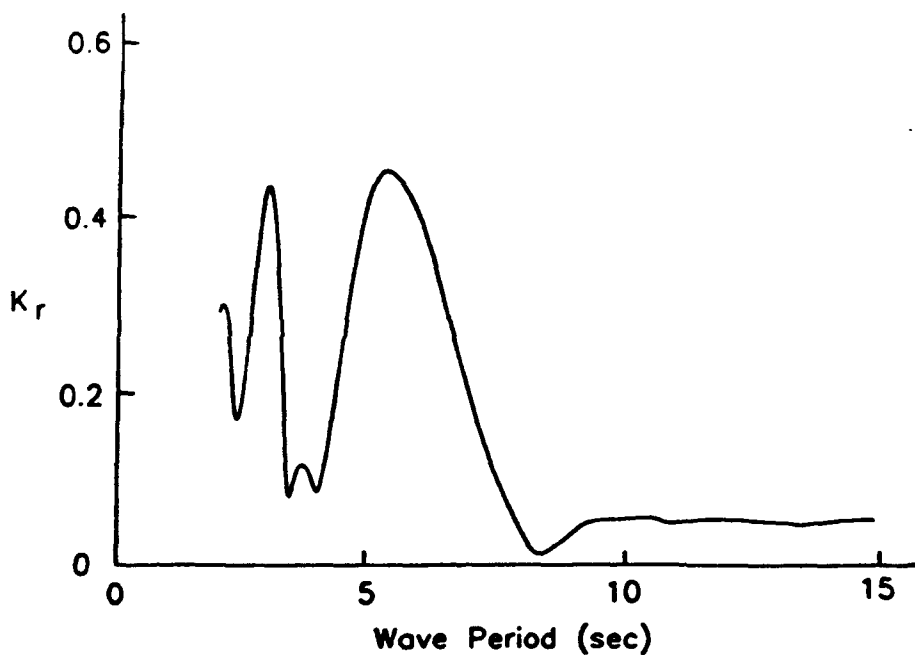


Figure 6. Estimated reflection characteristics for the field tested breakwater.

Installation and Recovery

The bar modules were assembled in a staging area located about 200 meters from the beach. After assembly, the modules were carried to the beach with a large front-end loader. The loader placed the modules on the upper beach face in groups of three, with their skids oriented perpendicular to the shore. Scour plates were attached to each module and tied up out of the way to facilitate module dragging.

Referring to Figure 7, the original installation plan called for dragging the modules into position in groups of three using a shore-based winch and a movable sheave and anchor assembly. In practice, we found that the waves at the site were too large to allow this method of installation. In particular, the LARC vehicle found it difficult to negotiate the surfzone while pulling a heavy anchor and cable. As a result, only one group of modules was installed using this technique. The rest of the modules were installed individually at extreme low tide using the front-end loader. Although rapid (all of the modules were installed in a single low tide), this alternative technique required placing the breakwater approximately 15 meters closer to shore. As a result, the breakwater was situated inside the surfzone for a substantial portion of the tidal cycle.

Monitoring Plan

A survey grid was established in the area of the breakwater and in an adjacent control area. Daily wading profiles were to be conducted in the test and control areas. These were to be supplemented by combined wading and fathometer surveys at the start and end of the experiment.

The incident directional wave spectrum was measured at a depth of 6 meters using a linear array of pressure sensors. A second array of pressure sensors and current meters was to measure the reflected wave field and the induced nearshore circulation field around the breakwater. The offshore array was constructed prior to the installation of the breakwater. The inshore array was to be constructed once the breakwater was in place. Unfortunately, this never occurred due to problems described below.

RESULTS

The Bragg reflection breakwater was deployed on 11 July 1988. During the week prior to installation, the significant wave height at the site averaged about 0.4 m.

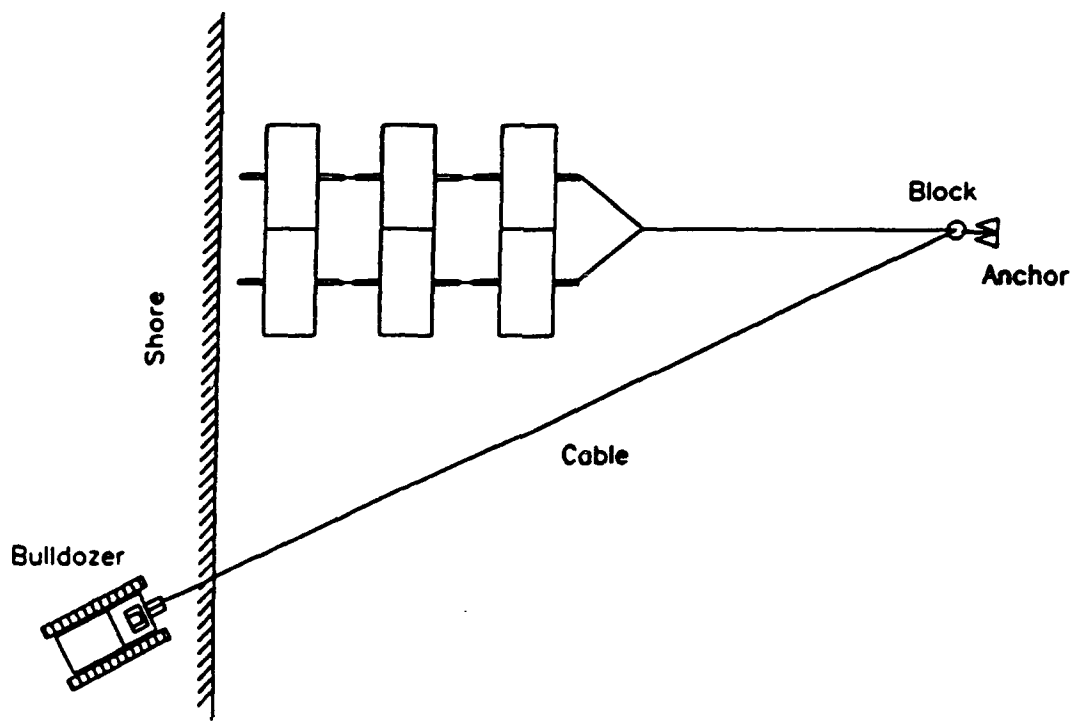


Figure 7. Planned installation method.

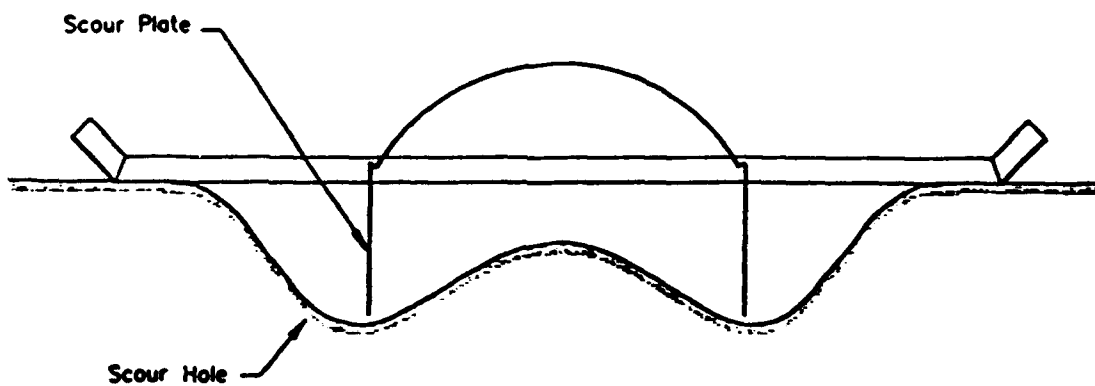


Figure 8. Observed scour pattern in field test.

This was approximately twice the anticipated wave height based on two years of measured wave data and essentially equal to the maximum design wave height for bar stability.

Immediately following breakwater installation, the significant wave height increased to about 0.6 m and remained at this level for the next 36 hours. These waves were significantly greater than the maximum design wave, causing the bar modules to slowly shift their positions. The modules rotated towards the direction of wave attack and moved shoreward about 1 to 2 m. The movement began with the outer-most bar and progressed inward through the middle and inner bars.

Another problem which developed almost immediately after installation of the breakwater was an intense scouring around the bar modules. As the tide rose, the bars were observed to be generating a significant degree of turbidity. On the following day we discovered large scour holes had formed in front of and behind the bars (see Figure 8). The scour holes slowly grew, becoming deeper and wider. Eventually they reached more than 2 meters deep, threatening the stability of the bar modules.

The observed scour was approximately an order of magnitude greater than the scour observed in the Port Hueneme tests. Since wave conditions were similar, we believe that the increased scour was attributable to the different properties of the two beach sands. At Port Hueneme, the sand was well sorted, having a median diameter of 0.25 mm and quartz and feldspar composition. At Cape Canaveral, the sand was poorly sorted, having a medium diameter of 0.14 mm and calcium carbonate composition. Apparently the lighter specific gravity of the Cape Canaveral sand, coupled with its smaller size and higher percentage of fines, resulted in increased sand suspension and enhanced scour.

After two days, the bar modules had become badly scattered. Some of the modules had shifted into their scour holes and begun to become buried. With bar burial becoming a growing problem, the decision was made to terminate the experiment and recover the bar modules while it was still possible. A bulldozer was used to pull the individual modules out of the surfzone and back up the beach face. From there, a front-end loader transported the modules back to the staging area where they were disassembled.

Because of the short duration of the breakwater deployment, the nearshore sensor array was never installed. As a result, no quantitative measurements were obtained.

Visual observations during the first few hours of deployment indicated that some wave reflection was occurring as evidenced by a standing wave pattern in front of the breakwater.

CONCLUSIONS

Theoretical and laboratory studies have indicated that the Bragg reflection breakwater concept may have merit as an expedient shore protection method. The wave sheltering produced by a small number of bars was found to significantly reduce the estimated erosion volume due to a model storm. The small scale field test, however, served to demonstrate many of the difficulties that will need to be overcome before the Bragg reflection breakwater concept becomes practical. Bar stability and seabed scour appear to be the most troubling problems. Further tests are needed to determine the overall merit of the concept.

REFERENCES

- Anton, J.P., Kaihatu, J.M., Kirby, J.T. and McSherry, T.R. (1990). "Bragg reflection from isolated and finite-length bars," Proc. 22nd International Conference on Coastal Engineering, The Hague, NL.
- Davies, A.G. and Heathershaw, A.D. (1984). "Surface-wave propagation over sinusoidally varying topography," Journal of Fluid Mechanics, Vol. 144, pp 419-443.
- DeVries, J. and Bailard, J.A. (1988). "A simple beach profile response model," Proc. IAHR Symposium on Math Modeling of Sediment Transport in the Coastal Zone, Copenhagen, DK.
- Herbers, T.C. and Guza, R. T. (1990). "Estimation of directional wave spectra from multi-component observations," Journal of Physical Oceanography, in review.
- Kirby, J.T. (1987). "A program for calculating the reflectivity of beach profiles," Univ. of Florida Report No. UFL/COEL-87/004, 43 pp.
- Mei, C.C. (1985). "Resonant reflection of surface water waves by periodic sand bars," Journal of Fluid Mechanics, Vol. 152, pp 315-335.

ACKNOWLEDGEMENTS

This research was funded by the Office of Naval Research

Appendix C: Considerations in Using Bragg Reflection for Storm Erosion Protection

J. Waterway, Port, Coastal and Ocean Engrng., 118, 62-74, 1992.

CONSIDERATIONS IN USING BRAGG REFLECTION FOR STORM EROSION PROTECTION

By James A. Ballard,¹ Member, ASCE, Jack W. DeVries,² and James T. Kirby,³ Member, ASCE

ABSTRACT: It has been suggested that Bragg reflection, the combined coherent wave reflection from a few low-lying shore-parallel bars, might be used to protect a beach against storm-wave attack. Numerical models are used to examine two issues relating to the feasibility of this concept: the degree of erosion protection provided by reflecting a portion of the incident wave energy, and the degree of wave reflection that can be generated by a bar field of varying geometry. The results show that a Bragg-reflection bar field must reflect about one-quarter of the incident wave energy to provide a significant measure of storm erosion protection. Bar fields with uniform spacing are capable of producing the required magnitude of wave reflection, but lack sufficient bandwidth. Bandwidth can be increased by staggering the spacings between bars, however, this produces a concurrent decrease in wave-reflection magnitude. Bragg-reflection bar fields appear capable of providing a limited measure of storm erosion protection along U.S. Gulf Coast and Atlantic Coast beaches, but their bandwidth may be too limited for use along Pacific Coast beaches.

INTRODUCTION

Davies (1980) suggested that the combined action of a few low-lying shore-parallel bars could reflect a significant portion of the incident wave energy, thus protecting the beach behind the bars. This phenomenon, dubbed Bragg reflection after a similar phenomenon in optics, has received considerable attention in the recent literature. Theoretical and laboratory studies have shown that wave energy can indeed be reflected by a Bragg-reflection bar field; however, the following question remains: is it practical to use Bragg reflection to protect a beach against storm wave attack? There are many issues beyond mere reflection that have a bearing on this question.

For Bragg reflection to be a useful shore-protection method, a bar field must be relatively simple to construct, it must produce a significant degree of erosion protection, and it must be adaptable to a wide range of wave and beach conditions. Bailard et al. (1990) addressed elements of the first issue. This paper addresses elements of the second and third issues via application of two numerical beach-profile response models and a numerical wave-reflection model.

BACKGROUND

In a series of three papers, Davies (1980, 1982a, 1982b) considered the two-dimensional interaction between surface waves and a fixed pattern of undulations on the seabed. Each undulation reflects a small amount of wave energy, with the combined reflection from a series of undulations being

¹Prin., James Bailard & Assoc., 1150 Bailard Ave., Carpinteria, CA 93013.

²Engr., Naval Civ. Engrg. Lab., Port Hueneme, CA 93043.

³Prof., Univ. of Delaware, Newark, DE 19716.

Note. Discussion open until June 1, 1992. To extend the closing date one month, a written request must be filed with the ASCE Manager of Journals. The manuscript for this paper was submitted for review and possible publication on February 25, 1991. This paper is part of the *Journal of Waterway, Port, Coastal, and Ocean Engineering*, Vol. 118, No. 1, January/February, 1992. ©ASCE, ISSN 0733-950X/92/0001-0062/\$1.00 + \$.15 per page. Paper No. 1433.

either coherent or destructive, depending on the phase relationship. The latter is a function of the ratio of the surface wavelength to the spacing between bed undulations. Davies found that the coefficient of wave reflection was oscillatory with respect to the wavelength-to-spacing ratio. He also found that a resonant condition occurred when the surface wavelength was exactly twice the spacing of the bed undulations. Thus, it appeared that for certain wave conditions, a few shore-parallel bars might reflect a substantial portion of the incident wave energy.

In support of these findings, a series of laboratory experiments (Heathershaw 1982; Davies and Heathershaw 1984) were undertaken to measure the reflection of monochromatic waves from a series of sinusoidal bed undulations. The results confirmed Davies's theoretical predictions for all but the resonant condition.

Mei (1985) developed an alternate theory that applied to the resonant reflection condition. Later, Hara and Mei (1987) extended this work to include the nonresonant case as well. In the meantime, Kirby (1986) developed a general wave-equation solution that was applicable to both resonant and nonresonant conditions.

Directional Waves and Sloping Bottom

Most of the work on Bragg reflection has been done in two dimensions using normally incident, monochromatic waves. The issue of nonnormal incidence was briefly addressed, in theory, by Mei (1985). His results indicated that, relative to the normally incident case, the effective bar spacing was increased by an amount proportional to the divergence of the incident-wave angle.

The effect of beach slope on the Bragg-reflection process was considered by both Mei (1985) and Kirby (1986). Both found that a sloping bed had the effect of altering the ratio of the local wavelength to the spacing between bed undulations. By varying the spacings between undulations to account for the local change in wavelength, results were obtained that were identical to the constant depth case.

Nonsinusoidal Undulations

A sinusoid is not a practical shape for an artificial Bragg-reflection bar field. Kirby (1987) and Mei et al. (1988) suggested that reflection from nonsinusoidal undulations could be calculated by expanding the shape function of the bar field as a Fourier series. Kirby and Anton (1990) developed an extension to the nonresonant interaction theory of Davies and Heathershaw (1984) that allowed calculation of wave reflection from the individual Fourier components of the bottom undulations. A series of laboratory experiments were conducted to verify their theoretical results. They found that for a series of smooth bumps on an otherwise flat bottom, the peak reflection was reduced slightly relative to an equivalent sinusoidal bottom.

These studies provide the groundwork for consideration of Bragg reflection as a shore-protection alternative. Bragg reflection appears to be a workable concept in theory and in the laboratory, but is it a reasonable means to protect a natural beach?

PERFORMANCE CRITERIA

Laboratory studies have shown that a Bragg-reflection bar field will modify the incident-wave field, triggering a process leading to the formation of

a tombolo behind the bar field (Kirby and Anton 1990). The process begins with the bar field reflecting a portion of the incident-wave energy. The resulting wave sheltering produces a long shore gradient in the wave-driven radiation stress, causing lateral inflows behind the bar field and a seaward-flowing rip current at its center. Laboratory experiments have suggested qualitatively that this circulation cell will cause sand to accumulate behind the bar field, leading to the formation of a tombolo.

It can be hypothesized that a Bragg-reflection bar field will protect a beach against storm-wave attack in three ways: by reducing the volume of sand eroded during the storm as a result of wave sheltering; by providing additional sand volume available for erosion via formation of a tombolo; and by restricting the loss of sand offshore via formation of a perched beach. This paper deals with only the first protective mechanism; however, it should be noted that the other two mechanisms may have a significant bearing on the ultimate feasibility of the Bragg-reflection bar concept.

Beach Erosion Protection

The effect of a Bragg-reflection bar field in reducing the volume of sand eroded from a beach by storm waves was investigated using two numerical beach-profile response models. The first model was developed by Kriebel (1982) and subsequently included in the Automated Coastal Engineering System (1989), published by the U.S. Army Engineers Coastal Engineering Research Center. The model is based on the assumption that the beach profile evolves towards a shape having a uniform distribution of wave-energy dissipation. In general, the model has been shown to do a good job of predicting erosion, but a poorer job of predicting accretion (Kriebel 1986; Birkemeier et al. 1987).

The second beach-profile response model was developed by DeVries and Bailard (1988). The model is based on Bagnold's (1963) energetics sediment-transport concepts, as generalized by Bailard (1981). Although its principal use has been as a research tool for understanding cross-shore sediment-transport processes, the model has been found to exhibit realistic erosion and accretion behavior (Bailard 1985).

These models were used to predict the volume of sand eroded from an initially planar beach during an idealized two-day storm (see Fig. 1). For simplicity, it was assumed that the sole effect of the Bragg-reflection bar field was to reduce the incident-wave height. The transmitted-wave height behind the bar field was related to the incident-wave height by a reflection coefficient, K_r , defined as

$$H_t^2 = (1 - K_r^2)H_i^2 \dots\dots\dots (1)$$

where H_t = transmitted-wave height; and H_i = incident-wave height. Base-line conditions (i.e., no bar field present) were computed using a wave-reflection coefficient equal to zero.

Storm erosion volumes were computed for a range of sediment sizes, initial beach slopes, incident-wave heights, wave periods, and wave-reflection coefficients (see Tables 1 and 2). The response of the beach was computed in terms of a normalized erosion volume, V_n , defined as

$$V_n = \frac{V_r}{V_0} \dots\dots\dots (2)$$

where V_r = erosion volume with wave reflection (i.e., with a bar field

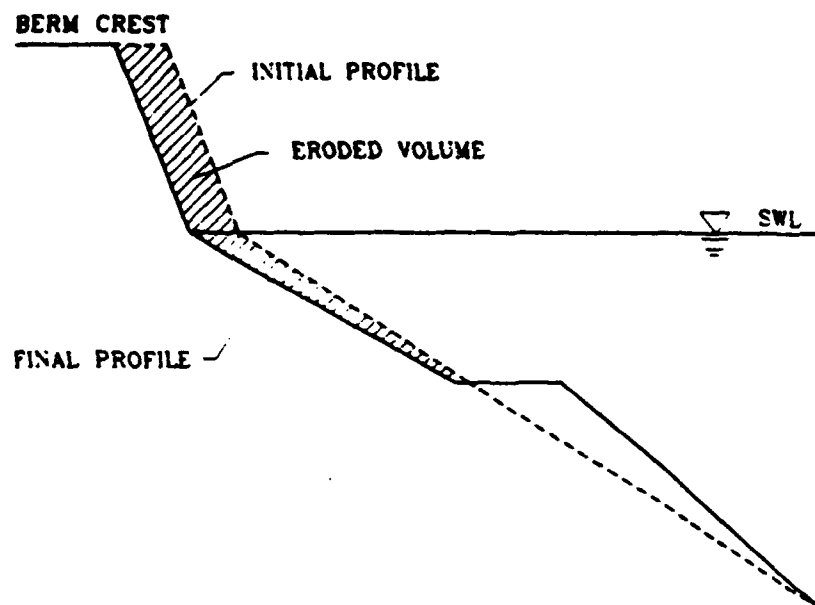


FIG. 1. Schematic Diagram of Beach-Profile Response to Storm-Wave Attack

TABLE 1. Parameter Values for Beach-Profile Models

Variable (1)	(2)	(3)	(4)	(5)
Wave height* (m)	2.00	3.00	—	—
Wave period* (sec)	6.00	8.00	12.00	—
Grain size* (mm)	0.20	0.40	0.60	—
Foreshore slope*	0.02	0.03	0.04	0.05
Reflection coefficient*	0.20	0.50	0.80	0.95

*Used in all combinations.

TABLE 2. Parameter Values for Beach-Profile Models

Constant (1)	(2)
Storm duration (hr)	48.0
Berm height (m, SWL)	8.0
Slope of berm face	0.08
Offshore slope	0.02*
Initial depth of slope intercept (m, SWL)	-2.0*
Drag coefficient	0.005*
Bedload efficiency	0.13*
Suspended load efficiency	0.01*

*DeVries and Bailard (1989) model only.

present); and V_0 = erosion volume without wave reflection (i.e., baseline conditions).

For both beach-profile response models, the normalized erosion volume was found to be a strong function of the reflection coefficient and a weaker function of the sediment-grain size, the near-shore beach slope and the incident-wave height. The incident-wave period was found to have a negligible effect on the normalized erosion volume.

Fig. 2 shows a plot of the predicted normalized erosion volume as a function of the wave-reflection coefficient. Due to the weak dependency of the erosion volume on the sediment grain size, beach slope, and incident wave height, there was considerable scatter in the predicted erosion volumes for each model. To simplify interpretation, only the average and extreme values from each model were plotted in Fig. 2. For both models, averaging was done over all cases producing erosion of the beach.

Reflection Bandwidth

A Bragg-reflection bar field will typically reflect wave energy over a relatively narrow range of wave periods. To be an effective shore-protection device, a bar field must reflect wave energy over the full range of storm-wave periods anticipated at a given beach. A survey was made of typical wave climates along three U.S. coastlines to determine the required bandwidths for potential Bragg-reflection bar fields. Utilizing data from Thompson (1977) and Jensen (1983), wave periods were noted for past storms having a recurrence interval of 2 years or less. Table 3 contains a list of the range of wave periods for Atlantic Coast, Gulf Coast, and Pacific Coast storms. Gulf Coast storms have the narrowest range of wave periods (5–9 s), with Atlantic Coast storms having a somewhat wider range (6–11 s), and Pacific Coast storms having the widest range (6–17 s). Normalizing these wave-period ranges by their central wave period, the normalized bandwidths of storms are approximately 0.70 for Gulf Coast and Atlantic Coast beaches, and 1.0 for Pacific Coast beaches.

REFLECTION PERFORMANCE

In assessing the anticipated performance of a Bragg-reflection bar field, a few practical limits were placed upon its configuration. First, it was as-

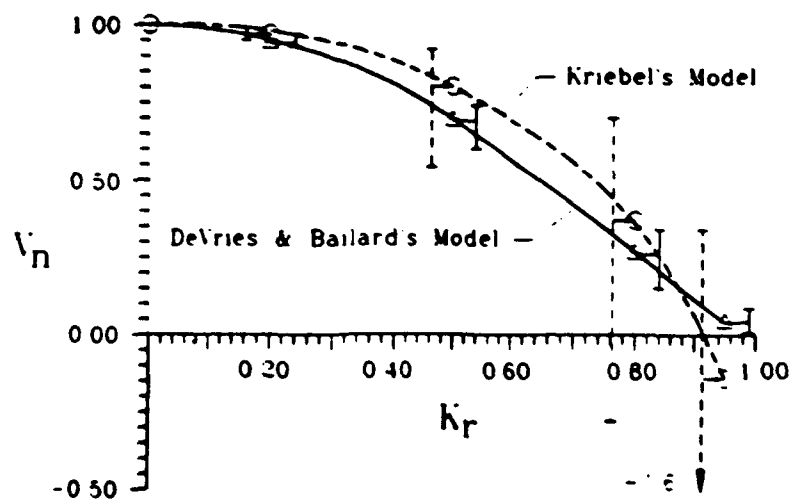


FIG. 2. Predicted Normalized Beach-Erosion Volume versus Wave Reflection Coefficient for Two Beach-Profile Response Models

TABLE 3. Wave Period Ranges for Commonly Occurring Storms along U.S. Coastlines

Site (1)	Atlantic Coast (2)	Gulf Coast (3)	Pacific Coast (4)
Range (s) BW/T_o	6-11 0.71	5-9 0.71	6-17 1.00

Note: Data from Jensen (1983) and Thompson (1977).

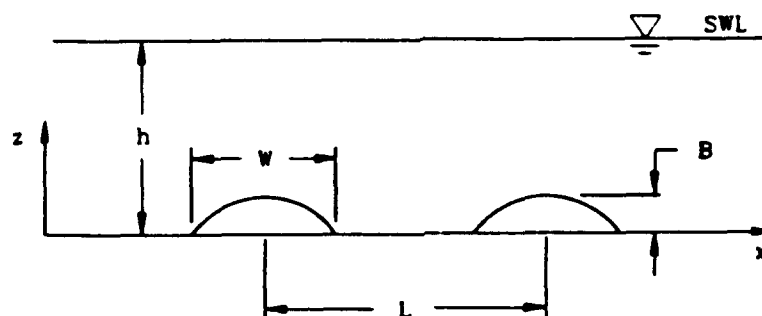


FIG. 3. Definition Diagram for Uniformly Spaced Bar Geometry

sumed that the bar-height-to-water-depth ratio, B/h , could not exceed 0.5. Beyond this value, the bars begin to look more like submerged breakwaters than undulations on the seafloor. Second, it was assumed that a bar field could include no more than 9 bars. Even with this limitation, seaward bars tend to become large on beaches having moderate slopes (for constant B/h ratio). Finally, it was assumed that the bar field resided in shallow water. This last assumption ensures that the wave-reflection characteristics of the bar field are solely functions of the bar height-to-depth ratio, B/h , the bar width-to-spacing ratio, W/L , and the total number of bars.

Uniform Bar Spacing

The reflection characteristics of Bragg-reflection bar fields having a uniform spacing between bar elements were investigated using Kirby's (1987) numerical wave-reflection model. For simplicity, constant depth was assumed, however, the same results could have been obtained by adjusting the bar spacing to account for wave shoaling on a sloping bottom.

Referring to Fig. 3, the bar field consisted of cosine-shaped bumps on an otherwise flat bed such that the shape of the bottom, $z(x)$, can be described as:

$$z(x) = B \sin \left[\frac{\pi}{W} \left(x - nL + \frac{W}{2} \right) \right]; \quad \left(nL - \frac{W}{2} \leq x \leq nL + \frac{W}{2} \right) \quad (3a)$$

$$z(x) = 0; \quad \text{otherwise} \quad (3b)$$

where B = bar height; W = bar width; L = bar spacing; and n = number of the bar element.

Wave-reflection properties were estimated for three different Bragg-reflection bar fields over a range of bar height-to-depth ratios (B/h) and bar width-to-bar spacing ratios (W/L). Results were computed for bar fields consisting of three, five, and nine elements.

Fig. 4 is a plot of the normalized reflection bandwidth as a function of the ratios B/h and W/L for each bar field. The normalized bandwidth was defined as the width of the principal wave-reflection peak (in s) at the half-value of the peak reflection coefficient, divided by the central wave period (see Fig. 5).

Fig. 6 is a plot of the effective wave-reflection coefficient as a function of the ratios B/h and W/L for each bar field. The effective wave-reflection coefficient was defined as the average value of the reflection coefficient over the bandwidth of the principal reflection peak (see Fig. 7).

Staggered Bar Spacing

Bragg-reflection bar fields with uniform bar spacings have relatively narrow bandwidths ($0.1 < BW/T_0 < 0.5$). These bandwidths are less than the normalized bandwidths of frequently occurring storms on most U.S. beaches ($0.7-1.0$), thus limiting the utility of a uniformly spaced bar field. It is possible, however, to alter the bandwidth of a Bragg-reflection bar field by staggering the spacings between bar elements.

Kirby (1987) briefly considered the idea of staggered bar spacings and found that the bandwidth of a Bragg-reflection bar field could be increased, but only at the expense of reducing the wave-reflection coefficient. In the present study this concept was further explored by systematically varying the spacing geometry of three Bragg-reflection bar fields.

Effective wave-reflection coefficients and reflection bandwidths were calculated for three-, five-, and nine-element bar fields having constant B/h

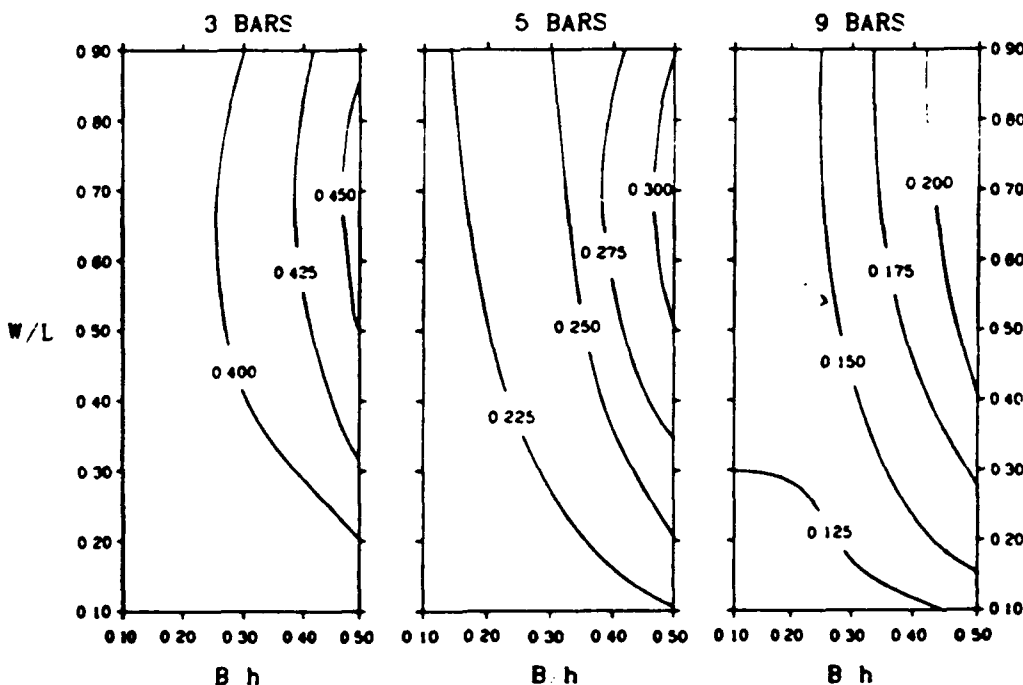


FIG. 4. Dimensionless Reflection Bandwidth (BW/T_0) versus Bar-Width-to-Bar-Spacing Ratio (W/L) and Bar-Height-to-Water-Depth Ratio (B/h) for Uniformly Spaced Bar Fields Composed of 3, 5, and 9 Elements

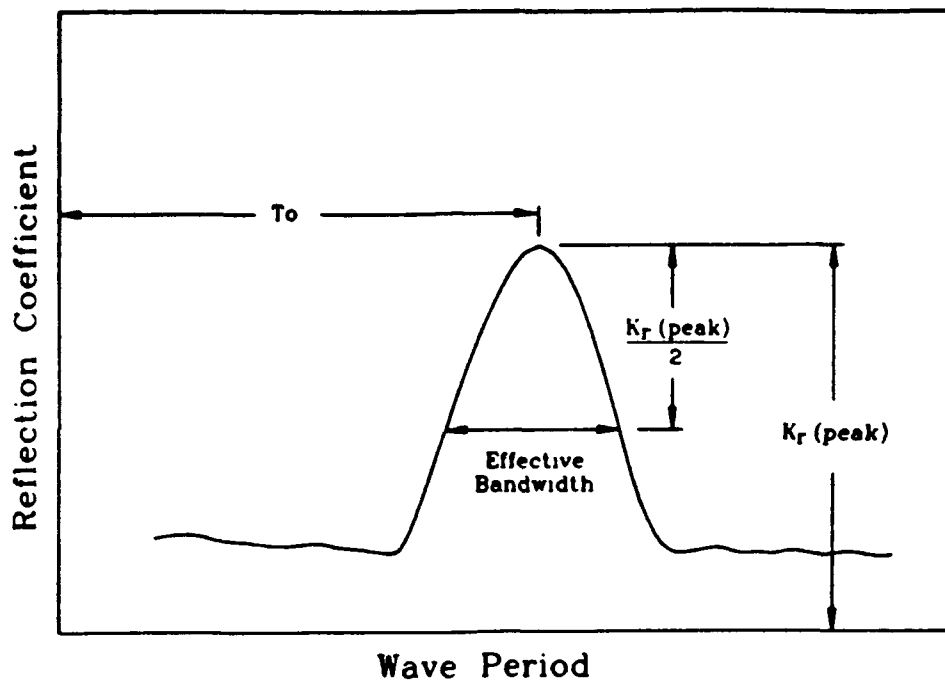


FIG. 5. Definition Diagram for Effective Wave-Reflection Bandwidth

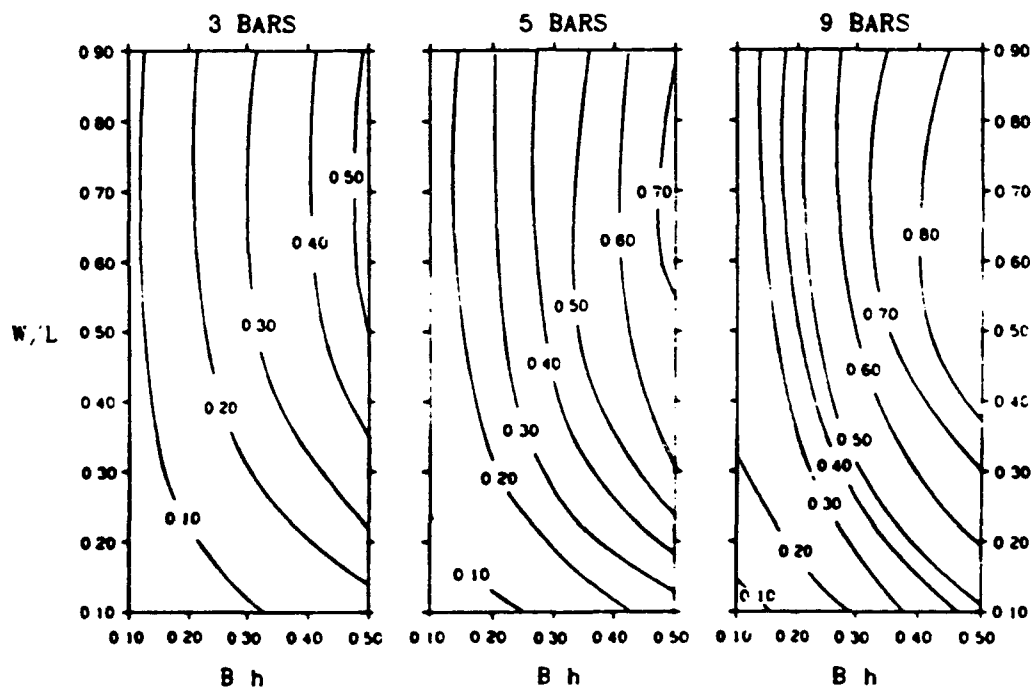


FIG. 6. Effective Coefficient of Wave Reflection ($K_{r, \text{effective}}$) versus Bar-Width-to-Bar-Spacing Ratio (W/L) and Bar-Height-to-Water-Depth Ratio (B/h) for Uniformly Spaced Bar Fields Composed of 3, 5, and 9 Elements

and W/L ratios of 0.3 and 0.4, respectively. The geometries of the bar fields were varied, as shown in Fig. 8, by applying a stretching parameter, Δ , defined as follows:

$$L' = L(1 \pm n\Delta); \quad n = 1, 2, 3, 4 \dots \dots \dots (4)$$

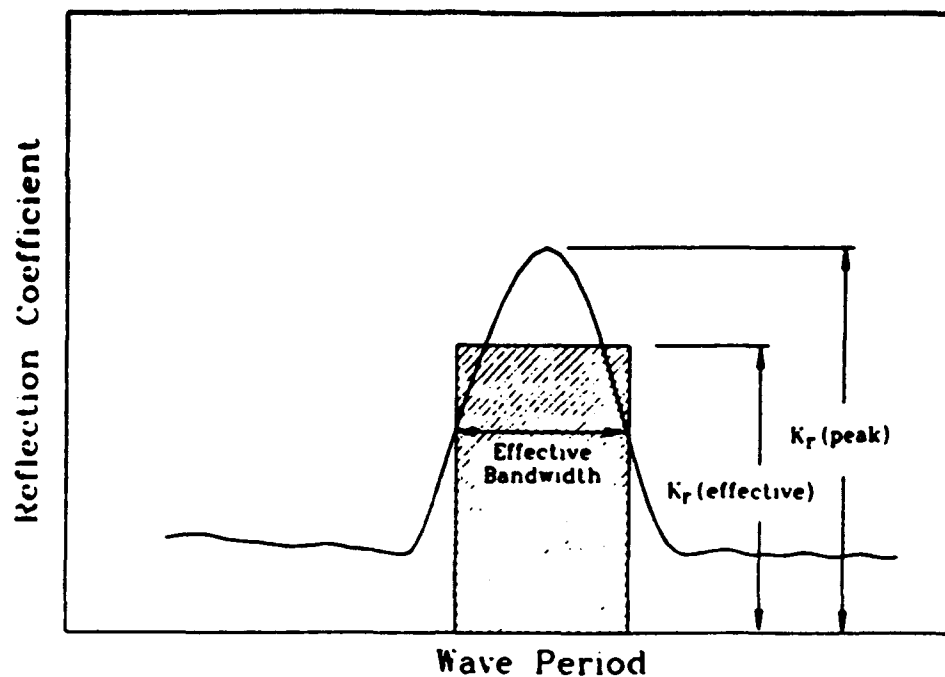


FIG. 7. Definition Diagram for Effective Coefficient of Wave Reflection

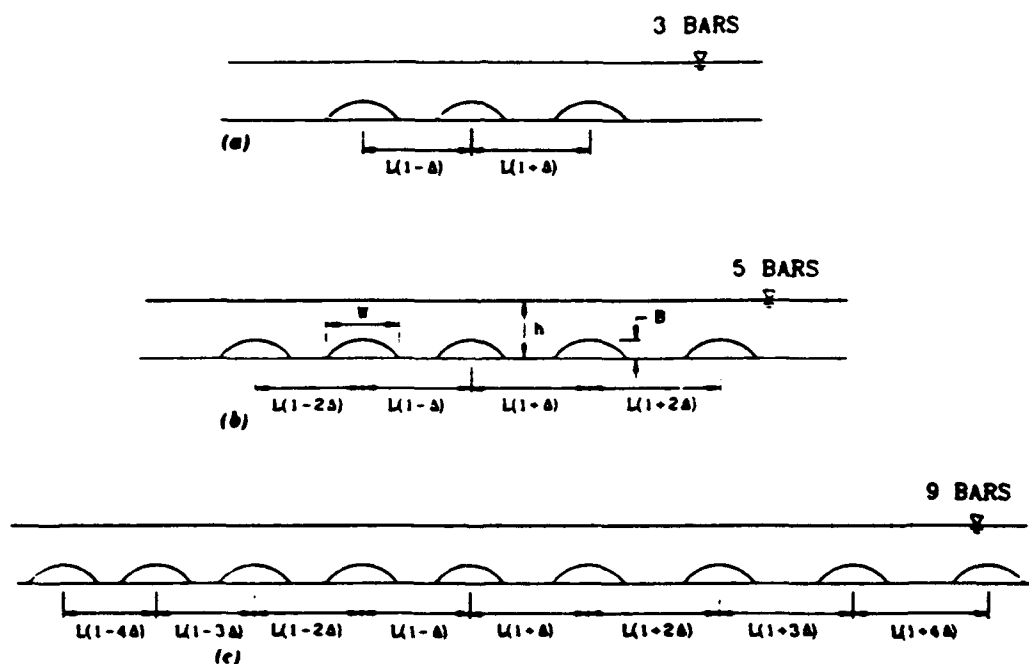


FIG. 8. Definition Diagram for Staggered Spaced Bar Geometries

where L' = the local staggered bar spacing; and L = the equivalent uniform bar spacing defined as the overall width of the bar field divided by the number of bar spaces.

Fig. 9 shows a plot of the predicted bandwidths for each bar field as a function of the stretching parameter, Δ . Fig. 10 shows a plot of the predicted wave-reflection coefficient for each bar field as a function of the stretching parameter. In both figures, the predicted bandwidths and wave-reflection

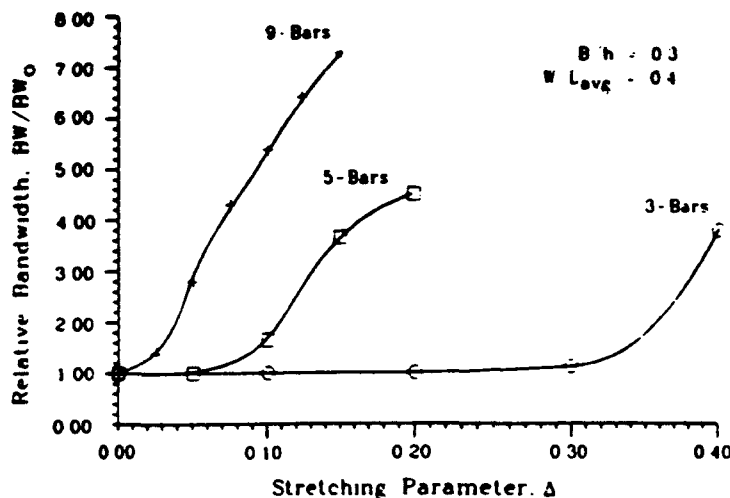


FIG. 9. Relative Bandwidth (BW/BW_0) versus Bar Geometry Stretching Parameter (Δ) for Staggered Bar Fields

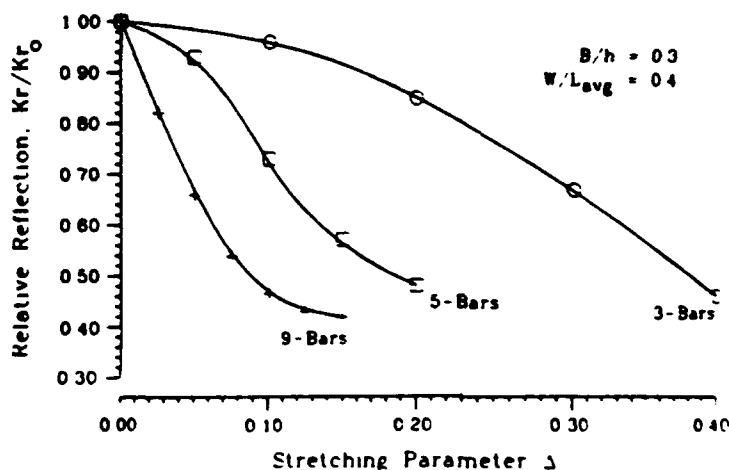


FIG. 10. Relative Wave Reflection Coefficient (K/K_0) versus Bar Geometry Stretching Parameter (Δ) for Staggered Bar Fields

coefficients have been normalized by their corresponding values for uniform bar spacings.

Alternative staggered bar geometries were also evaluated, however, the best results were quantitatively similar to those in Figs. 9 and 10. Similarly, the ratio B/h was found to have a relatively small influence on these results.

COMMENT

The aforementioned results suggest that a Bragg-reflection bar field reduces storm erosion approximately in proportion to the percentage of wave energy that it reflects. Referring to Fig. 2, a bar field having a modest wave-reflection coefficient of 0.2 will reduce the predicted storm erosion volume by about 4%. Similarly, a bar field having a wave-reflection coefficient of 0.5 will reduce the predicted storm erosion volume by about 25%. Consequently, as a guideline, it appears that a Bragg-reflection bar field must

produce a wave-reflection coefficient of about 0.5 in order to be an effective shore-protection device.

Referring to Figs. 4 and 6, Bragg-reflection bar fields having uniformly spaced bar elements are capable of producing the desired level of wave reflection ($K_r = 0.5$), but lack sufficient bandwidth for practical application. Bar fields having a small number of elements have a wide (although insufficient) bandwidth, but a modest level of wave reflection. Bar fields having a large number of elements have a high level of wave reflection, but very narrow bandwidths.

To be of practical use along U.S. coastlines, a Bragg-reflection bar field must have a dimensionless bandwidth of at least 0.7. Fig. 4 indicates that the maximum bandwidths produced by the uniformly spaced Bragg-reflection bar fields range from a high of 0.45 (3 bars) to a low of 0.20 (9 bars). These bandwidths can be significantly increased by staggering the spacing between bar elements (see Fig. 9), but this also decreases the wave-reflection magnitudes (see Fig. 10).

Assuming that data in Figs. 9 and 10 can be applied to B/h ratios between 0.1 and 0.5, and W/L ratios between 0.3 and 0.9 (spot checks indicate that this is approximately true), maximum bandwidths and wave-reflection coefficients were estimated for staggered bar fields consisting of three, five, and nine elements. Referring to Table 4, it was found that minimally acceptable performance (i.e., a wave-reflection coefficient of 0.5 and a normalized bandwidth of 0.7) was just possible using a nine-element staggered bar field having a B/h ratio of 0.5, a W/L ratio of 0.6, and a Δ -value of 0.07.

These findings suggest that a Bragg-reflection bar field may have some potential as a shore-protection device for Gulf Coast and Atlantic Coast beaches, but little potential for Pacific Coast beaches. Considering just the effects of two-dimensional wave sheltering, the number and size of the bar elements required to produce a significant level of storm erosion protection will make construction of a Bragg-reflection bar field a significant undertaking. The difficulty and expense of constructing an effective Bragg-reflection breakwater could easily approach that of a conventional detached breakwater, however, the latter has greater bandwidth and wave-reflection capabilities.

The foregoing findings are based on a consideration of simple two-dimensional wave sheltering. Other mechanisms that may provide additional erosion protection include: the formation of a tombolo behind the bar field, and the formation of a perched beach. The tombolo would provide additional sand to the beach profile, thus reducing the magnitude of the induced shoreline retreat. The perched beach may result from the retention of eroded

TABLE 4. Maximum Available Bandwidths for Staggered Bar Fields

Site (1)	Required bandwidth (s) (2)	Available Bandwidth ^a		
		Three bars (s) (3)	Five bars (s) (4)	Nine bars (s) (5)
Atlantic Coast	5.0	3.2	3.4	5.2
Gulf Coast	6.0	3.8	4.2	6.4
Pacific Coast	12.0	5.2	5.8	8.6

^aCalculated assuming $K_r = 0.5$.

sand against the shoreward bar element, limiting the induced shoreline retreat.

CONCLUSIONS

Bragg-reflection bar fields appear capable of providing a limited measure of storm-erosion protection on Gulf Coast and Atlantic Coast beaches. Sufficient bandwidth can be obtained by staggering the spacing between bar elements; however, adequate levels of wave reflection will require more than just a few low-lying bars.

Numerical model results indicate that a staggered nine-element bar field is necessary to provide a 25% reduction in storm erosion volume for Gulf Coast and Atlantic Coast beaches. To produce this measure of protection, the bar elements must have a height of approximately half the local water depth. The difficulty in constructing a bar field with this number of large bar elements suggests that the Bragg-reflection bar concept may not be practical for most beaches.

Laboratory studies indicate that a Bragg-reflection bar field may produce a tombolo or a perched beach condition. Although outside the scope of this study, these effects may significantly enhance the ultimate feasibility of the Bragg-reflection bar concept.

ACKNOWLEDGMENTS

This work was supported by the Office of Naval Research (ONR). Dr. Bailard's work was performed while an employee at the Naval Civil Engineering Laboratory. Dr. Kirby's work was supported by ONR grant numbers N00014-89-J-1717 and N00014-86-K-0790.

APPENDIX I. REFERENCES

- Automated coastal engineering system.* (1989). U.S. Army Corps of Engrs. Coastal Engrg. Res. Ctr., Vicksburg, Miss.
- Bagnold, R. A. (1963). "Mechanics of marine sedimentation." *The sea: Ideas and observations*, Vol. 3, Interscience Publishing, New York, N.Y., 507-553.
- Bailard, J. A. (1981). "An energetics total load sediment transport model for a plane sloping beach." *J. Geophys. Res.*, 86(11), 10938-10954.
- Bailard, J. A. (1985). "Simple models for surfzone sediment transport." *Tech. Note Number N-1740*, Naval Civ. Engrg. Lab., Port Hueneme, Calif.
- Bailard, J. A., DeVries, J. W., Kirby, J. T., and Guza, R. T. (1990). "Bragg reflection breakwater: A new shore protection method?" *Proc. 22nd Int. Conf. on Coastal Engrg.*, ASCE, New York, N.Y., 1702-1715.
- Bierkemeier, W. A., Kraus, N. C., Scheffner, N. W., and Knowles, S. C. (1987). "Feasibility study of quantitative erosion models for use by the Federal Emergency Management Agency in the prediction of coastal flooding." *Tech. Report Number TR-87-8*, U.S. Army Corps of Engrs. Coastal Engrg. Res. Ctr., Vicksburg, Miss.
- Davies, A. G. (1980). "Some interactions between surface water waves and ripples and dunes of the seabed." *Tech. Report Number 108*, Inst. of Oceanographic Sci., Taunton, U.K.
- Davies, A. G. (1982a). "On the interaction between surface waves and undulations on the seabed." *J. Mar. Res.*, 40(Jul.), 331-368.
- Davies, A. G. (1982b). "The reflection of wave energy by undulations on the seabed." *Dynamics of Atmospheres and Oceans*, 6(4), 207-232.
- Davies, A. G., and Heathershaw, A. D. (1988). "Surface-wave propagation over sinusoidally varying topography." *J. Fluid Mech.*, 144, 419-443.
- DeVries, J. W., and Bailard, J. A. (1989). "A simple beach profile response model."

- Proc. Symp. on Mathematical Modelling of Sediment Transport in the Surfzone*, Int. Association of Hydr. Res. (IAHR), Delft, The Netherlands, 215-224.
- Hara, T., and Mei, C. C. (1987). "Bragg scattering of surface waves by periodic bars: Theory and experiment." *J. Fluid Mech.*, 178(May), 59-76.
- Heathershaw, A. D. (1982). "Seabed-wave resonance and sand bar growth." *Nature*, 296(25), 343-345.
- Jensen, R. E. (1983). "Atlantic Coast hindcast, shallow-water significant wave information." *WIS Report Number 9*, U.S. Army Corps of Engrs., Waterways Experiment Station, Vicksburg, Miss.
- Kirby, J. T. (1986). "A general wave equation for waves over rippled beds." *J. Fluid Mech.*, 162(Jan.), 171-186.
- Kirby, J. T. (1987). "A program for calculating the reflectivity of beach profiles." *Contract Report Number UFL/COEL-87/004*, Univ. of Florida, Gainesville, Fla.
- Kirby, J. T., and Anton, J. P. (1990). "Bragg reflection of waves by artificial bars." *Proc. 22nd Int. Conf. on Coastal Engrg.*, ASCE, New York, N.Y., 757-768.
- Kriebel, D. L. (1982). "Beach and dune response to hurricanes," thesis presented to Univ. of Delaware, Newark, Del., in partial fulfillment of the requirements for the degree of Master of Science.
- Kriebel, D. L. (1986). "Verification study of a dune erosion model." *Shore and Beach*, 54(3), 13-21.
- Mei, C. C. (1985). "Resonant reflection of surface waves by periodic sandbars." *J. Fluid Mech.*, 152(Mar.), 315-335.
- Mei, C. C., Hara, T., and Naciri, M. (1988). "Note on Bragg scattering of water waves by parallel bars on the seabed." *J. Fluid Mech.*, 186(Jan.), 147-162.
- Thompson, E. F. (1977). "Wave climate at selected locations along U.S. coasts." *Tech. Report Number 77-1*, U.S. Army Corps of Engrs., Coastal Engrg. Res. Ctr., Vicksburg, Miss.

APPENDIX II. NOTATIONS

The following symbols are used in this paper:

- B = bar height;
 BW = bandwidth;
 BW_0 = bandwidth with uniformly spaced bars;
 C_f = drag coefficient for bed;
 h = water depth;
 H_i = incident-wave height;
 H_t = transmitted-wave height;
 K_r = wave-reflection coefficient;
 K_{r0} = reflection coefficient with uniformly spaced bars;
 L = spacing between bar crests;
 n = number of bar element;
 T_0 = wave period at central reflection peak;
 V_n = normalized beach-erosion volume, V/V_0 ;
 V_0 = beach-erosion volume without wave reflection;
 V_r = beach-erosion volume with wave reflection;
 W = bar width;
 x = horizontal distance;
 z = vertical elevation;
 Δ = staggered bar stretching parameter;
 ϵ_b = bed-load efficiency;
 ϵ_s = suspended load efficiency; and
 π = 3.14.

Appendix D: A Note on Bragg Scattering of Surface Waves by Sinusoidal Bars

to be submitted to *Physics of Fluids*.

A note on Bragg scattering of surface waves by sinusoidal bars

James T. Kirby
Center for Applied Coastal Research
Department of Civil Engineering
University of Delaware
Newark, DE 19716

Abstract

The reflection of linear surface waves by sinusoidal bottom undulations is considered in the case where the incident wave is not necessarily close to the resonant frequency. For finite detuning away from the resonant frequency, two previous solutions are shown to give results which are inconsistent with direct numerical solutions, especially when the results are extended to oblique incidence. The correction to the methods is given, and various consequences of the new results are examined.

1 Introduction

In recent years, the problem of the reflection of surface waves by undular bottom features has drawn considerable attention, owing primarily to the mechanism's possible relation to coastal morphology. Kirby (1986) has derived an extension to the usual mild-slope equation (Berkhoff, 1972) which provides a theoretical umbrella for most of the existing analytical results. Davies and Heathershaw (1984) solved for the reflection coefficient for the case of weak reflection (far from resonance) and sinusoidal bars in otherwise constant depth. Their solution was recovered from Kirby's equation by Kirby and Anton (1990), who also provided the extension to the case of oblique incidence over the bar field. Close to the resonant condition, where the bar wavenumber is twice the wavenumber component of the surface wave in the direction normal to bar crests, Mei (1985) provided a solution using a multiple scales approach. His solution was extended to oblique incidence by Dalrymple and Kirby (1986) and Mei et al (1988, hereafter referred to as MHN). Kirby (1986) showed that Mei's analysis could be obtained from the extended mild-slope formulation. Further explication of the problem (along with some additional solution techniques) may be found in Davies et al (1989), Kirby (1989), and Benjamin et al (1987). As in these papers, we restrict our attention here to the case of perfectly sinusoidal bars.

The resonant reflection solution of Mei proceeds by assuming that the waves are described by carrier waves which are exactly in resonance with the bar field, together with amplitudes which vary slowly in both space and time, to account for both frequency-wavenumber detuning and slow evolution over the bar field. The analysis results in a

set of perfectly tuned, coupled evolution equations for the wave amplitudes; these may be solved for the reflection coefficient and for the wave heights over the bar in the case of time-periodic motions.

For the case of finite, arbitrary detuning, it is natural to extend the approach given by Mei to consider the frequency and wavenumber detuning as part of the carrier wave; as a result, the coupled amplitude equations become explicitly detuned, but may still be easily solved for the case of periodic waves. Liu (1987) and Yoon and Liu (1987, referred to as YL) took this approach in two related studies. Liu considered the resonant reflection of linear monochromatic waves in a channel with corrugated sides and bottom, while YL considered the scattering of incident cnoidal waves by a sinusoidal bar field in the context of Boussinesq theory. (The latter problem has also been addressed by Kirby and Vengayil, 1988). For the case of normal incidence on the bar field, Liu's solution gave "cut-off" conditions (demarcating the boundary between exponential and sinusoidal behavior of the incident and reflected wave envelopes) which differed markedly from the values given by Mei (1985). These differences were attributed to the effect of finite detuning.

In this note, we formulate the problem of detuned scattering by a field of sinusoidal bars, and obtain a solution with different properties than would be found using the methods in Liu and YL. In section 2, a new formulation of the detuned-interaction theory is developed. This is followed in section 3 by a discussion of previous results and of their breakdown in the oblique incidence case. The methods of Liu and YL are extended to the oblique incidence case in the Appendix. In section 4, numerical results are used to establish the validity of the present formulation. We also show that the resonant interaction theory of Mei (1985) is reasonably robust for the entire range of physically relevant cases.

2 Solution of the generalized mild-slope equation for detuned resonance

In this section, we present a perturbation solution of the equation of Kirby (1986) which differs from the previous detuned interaction results given by Liu and YL. The derivation here follows the notation of MHN closely, although the governing modulation equations are arrived at by a different method. We consider the case of a patch of sinusoidal bars $\delta(x)$ given by

$$\delta(x) = D \sin(\lambda x); \quad \lambda = \frac{2\pi}{L} \quad (1)$$

where L is the bar wavelength and D is the bar amplitude. A finite patch of n bars rests in the interval $0 \leq x \leq nL$, superimposed on a uniform depth h . We generalize the previous results somewhat by considering the case of oblique incidence on the bar field, and take θ

to represent the angle between x and the incident wavenumber vector. The general two-dimensional form of the governing equation is then written as

$$\nabla \cdot (p \nabla \tilde{\phi}) + k^2 C C_g \tilde{\phi} = 0 \quad (2)$$

where

$$p = C C_g - \frac{g \delta(x)}{\cosh^2 kh} \quad (3)$$

and where the angular frequency ω , wavenumber k , phase speed C , and group velocity C_g are determined based on the mean depth h and the actual (tuned or detuned) wave period. For obliquely-incident waves, we take

$$\tilde{\phi} = \phi(x) e^{im y}; \quad m = k \sin \theta. \quad (4)$$

The governing equation is reduced to the second-order ODE in x ;

$$\phi_{xx} + \frac{p_x}{p} \phi_x + \gamma^2 \phi = 0 \quad (5)$$

where the factor γ^2 is given by

$$\gamma^2 = k^2 p^{-1} C C_g - m^2 \quad (6)$$

which, for the case of small bottom perturbations, may be approximated by

$$\gamma^2 = l^2 + \frac{g k^2 \delta}{C C_g \cosh^2 kh}; \quad l = \sqrt{k^2 - m^2} = k \cos \theta \quad (7)$$

As in Kirby (1986), we seek coupled first order equations of the form

$$\phi_x^+ = i \gamma \phi^+ + F(\phi^+, \phi^-) \quad (8)$$

$$\phi_x^- = -i \gamma \phi^- - F(\phi^+, \phi^-) \quad (9)$$

where the total wave field is divided into incident and reflected components,

$$\phi = \phi^+ + \phi^- \quad (10)$$

and $+$ ($-$) denotes the incident (reflected) wave. Substituting (8)-(10) in (5) leads to the result

$$F = -\frac{(\gamma p)_x}{2\gamma p} (\phi^+ - \phi^-). \quad (11)$$

To the leading order of approximation in powers of δ , the coefficients in (8) and (9) are given by

$$\gamma = l \left(1 + \frac{g \delta}{2 C C_g \cosh^2 kh \cos^2 \theta} \right) \quad (12)$$

$$\frac{(\gamma p)_x}{2\gamma p} = -\frac{2\alpha \Omega_0 \delta_x}{k C_g D} \quad (13)$$

where

$$\alpha = \frac{\cos 2\theta}{\cos^2 \theta} \quad (14)$$

and

$$\Omega_0 = \frac{gk^2 D}{4\omega \cosh^2 kh}. \quad (15)$$

Note that Ω_0 here differs from the value given in Mei (1985) in that it is evaluated at the detuned wavenumber rather than the resonant wavenumber. We also note that no approximations have been made in obtaining the basic form of the coupled equations (8) and (9); the splitting is reversible and no information has been suppressed. We introduce the explicit form of δ_x :

$$\delta_x = \frac{\lambda D}{2} (e^{i\lambda x} + e^{-i\lambda x}) \quad (16)$$

and seek a solution for slowly-varying incident and reflected waves of the form

$$\phi^+ = A(x)e^{ilx} = A(x)e^{ik \cos \theta x}; \quad \phi^- = B(x)e^{-ilx} = B(x)e^{-ik \cos \theta x}, \quad (17)$$

Following Liu and YL, we construct an approximate detuned-interaction model by substituting (17) in (8)-(9) and retaining terms which come closest to satisfying resonance conditions. This leads to the coupled evolution equations

$$A_x = -\frac{\Omega_0 \alpha \cos \theta}{C_g} \left(\frac{k_{res}}{k} \right) B e^{i\beta x} \quad (18)$$

$$B_x = -\frac{\Omega_0 \alpha \cos \theta}{C_g} \left(\frac{k_{res}}{k} \right) A e^{-i\beta x} \quad (19)$$

where

$$k_{res} = \frac{\lambda}{2 \cos \theta} \quad (20)$$

is the resonant wavenumber, and

$$\beta = \lambda - 2k \cos \theta \quad (21)$$

is the detuning parameter, as introduced in Liu and YL. For $l = k \cos \theta = \lambda/2$, we recover the exactly-resonant interaction equations following from MHN, equation (2.5). The detuned equations differ from the results in MHN by the inclusion of the factor (k_{res}/k) , which introduces an asymmetry in the coupling coefficient. We see that waves with lower wavenumbers (indicating relatively shallower water) become more strongly coupled, as may be expected on physical grounds.

We can increase the correspondence between the results of MHN and the present derivation by introducing a detuning wavenumber

$$K = k - k_{res} \quad (22)$$

and a corresponding frequency parameter

$$\Omega = KC_g \quad (23)$$

Note that Ω again differs from Mei's Ω since detuning is finite and the relation between the detuned wavenumber and the detuned frequency here is not linear, except in the limit of extremely shallow water. The detuning parameter β may now be written as

$$\beta = -2K \cos \theta. \quad (24)$$

We introduce the transformation

$$\begin{pmatrix} A \\ B \end{pmatrix} = \begin{pmatrix} \tilde{A} e^{-iK \cos \theta} \\ \tilde{B} e^{iK \cos \theta} \end{pmatrix} \quad (25)$$

and obtain the coupled equations

$$\tilde{A}_x = iK \cos \theta \tilde{A} - \frac{\Omega_0 \alpha \cos \theta}{C_g} \left(\frac{k_{res}}{k} \right) \tilde{B} \quad (26)$$

$$\tilde{B}_x = -iK \cos \theta \tilde{B} - \frac{\Omega_0 \alpha \cos \theta}{C_g} \left(\frac{k_{res}}{k} \right) \tilde{A} \quad (27)$$

We may reduce these to two second-order equations for \tilde{A} and \tilde{B} :

$$\begin{pmatrix} \tilde{A} \\ \tilde{B} \end{pmatrix}_{xx} + P^2 \begin{pmatrix} \tilde{A} \\ \tilde{B} \end{pmatrix} = 0 \quad (28)$$

The parameter P is determined from

$$P = \frac{\Omega_0 \cos \theta}{C_g} \left[\left(\frac{\Omega}{\Omega_0} \right)^2 - \alpha^2 \left(\frac{k_{res}}{k} \right)^2 \right]^{1/2} \quad (29)$$

and may be either real or imaginary depending on the term in square brackets. The expression for P here is also similar to the expression given in MHN, with the exception of the appearance of the k_{res}/k ratio. The cutoff condition in the solution corresponds to the value $P = 0$.

Equations (28) are solved with the boundary conditions

$$\tilde{A}(0) = A_0; \quad \tilde{B}(nL) = 0 \quad (30)$$

which indicates an incident wave amplitude of A_0 at the start of the bar field and a reflection of zero at the downwave end. The solution is given by

$$A(x) = A_0 e^{-iK \cos \theta x} \frac{PC_g \cos P(nL - x) - i\Omega \cos \theta \sin P(nL - x)}{PC_g \cos nPL - i\Omega \cos \theta \sin nPL} \quad (31)$$

and

$$B(x) = A_0 e^{iK \cos \theta x} \frac{\Omega_0 \alpha (k_{res}/k) \cos \theta \sin P(nL - x)}{PC_g \cos nPL - i\Omega \cos \theta \sin nPL}. \quad (32)$$

The reflection coefficient upwave of the bar field is given by

$$R = \left| \frac{B(0)}{A_0} \right| = \left| \frac{\Omega_0 \alpha(k_{res}/k) \cos \theta \sin nPL}{PC_g \cos nPL - i\Omega \cos \theta \sin nPL} \right| \quad (33)$$

We illustrate the present solution in comparison to the resonant solution of MHN by plotting contours of reflection coefficient as a function of θ and $2k \cos \theta / \lambda$, where resonance occurs at $2k \cos \theta / \lambda = 1$. The solution of MHN is implemented exactly as given in their paper, with K specified based on the chosen wavenumber parameter and Ω computed from $\Omega = KC_{g(res)}$. The choice of $2k \cos \theta / \lambda$ as a plotting parameter is inconvenient from a design point of view, where a fixed range of wave periods would lead to consideration of a fixed range of $2k/\lambda$. This alternate choice will be followed below; it is avoided in the initial comparisons here since the resonance curve goes to large values of $2k/\lambda$ as θ increases.

To maintain correspondence with experimental results given in Davies and Heathershaw (1984), we choose $n = 4$, $D/h = 0.32$, $D = 5\text{cm}$, $L = 1\text{m}$, and $h = 15.625\text{cm}$. Solutions are computed for the parameter range $.25 \leq 2k \cos \theta / \lambda \leq 1.75$, $0^\circ \leq \theta \leq 85^\circ$. Solutions for the resonant theory of MHN are shown in Figure 1. The symmetry of the theory about the resonance condition $2k \cos \theta / \lambda = 1$ is apparent, as is a tendency for the solution to die out for large values of θ . Figure 2 shows reflection coefficient contours and the locus of the cutoff condition for the present analytic theory. The results here are markedly asymmetric about the resonance condition. Agreement between the two analytic solutions is good, both for reflection coefficients and cutoff conditions, up to $\theta = 55^\circ$. For larger θ 's and for values of $2k \cos \theta / \lambda < 0.5$ and > 1.5 , the asymmetry of the solution becomes marked and the two approximate solutions deviate.

The apparent agreement between the cutoff conditions predicted here and the conditions predicted by the Mei (1985) and MHN theory is in marked contrast to the large deviation between cutoffs seen in comparing the theory of Liu and Mei (1985) (see section 4 in Liu). Direct numerical determination of the detuning β corresponding to the cutoff condition has been made for the bar geometry considered here, but with a range of D/h values. The cutoff condition on the high frequency side of resonance is compared to Mei's (1985) theory in Figure 3, where we plot the % error in Mei's result relative to the present theory. The results typically agree to within 1% or so. In contrast, Liu shows deviations on the order of 50% between his and Mei's predicted cutoffs.

For angles less than about 60° , we will evaluate the disagreement between the approximate solutions here by comparison with numerical solutions for the full problem. We close this section by remarking that both of the approximate solutions studied here would be expected to break down far from resonance, since the effect of neglected non-resonant terms in the equations would become as important as the effects of the retained terms.

3 Comparison with previous results

In this section, we compare the present results to the results obtained by extending the derivation techniques used in Liu and YL. Those derivations are described in Appendix A. The resulting derivations produce coupled equations with the same form as equations (18)-(19) above, and hence we can consider the correspondence between the form of the coupling coefficients, the values of the factor P and loci of the cutoff conditions, and numerical values of predicted reflection coefficients. We limit the comparison here to an examination of the coupling coefficients and, in particular, to the determination of the zeroes of those coefficients, where we see a decoupling between the wave and bar fields. Both the Liu and YL theories have the interesting feature of predicting decoupling for normally incident waves at a finite value of the parameter $2k/\lambda$. When extended to oblique incidence, both theories produce patterns of decoupling which are at odds with the present theory, with the MHN resonant theory, with the nonresonant theory of Kirby and Anton (1990), and with numerical results.

The interaction coefficient for the present theory may be written as

$$\frac{\Omega_0 \cos 2\theta}{C_g \cos \theta} \left(\frac{k_{res}}{k} \right) \quad (34)$$

which has a zero at $\theta = 45^\circ$ for all incident wave frequencies. This result also was found by MHN for the resonant case, and is a feature of a wide range of non-resonant scattering theories for small obstacles (see Kirby and Anton, 1990, for a review). The locus of the zero in the present coupling coefficient is shown in Figure 4 along with the locus of the resonance curve $2k/\lambda = 1/\cos \theta$.

The coupling coefficient α_1 obtained from the YL derivation has zeroes on the curve $2k/\lambda = 2 \cos \theta$, shown in Figure 4. The intersection of this curve with the resonance curve occurs at $\theta = 45^\circ$ and $2k/\lambda = \sqrt{2}$, as does the curve for the zeroes of the present theory. Away from this intersection, the predicted zeroes deviate markedly.

For the second theory of Appendix A, the interaction coefficient α_2 leads to decoupling on a curve $2k/\lambda = \sqrt{2}/\cos \theta$, which lies to the right of the resonant interaction curve in Figure 4 and doesn't intersect it anywhere.

The two theories described in Appendix A clearly predict patterns of wave-bottom interaction which are at odds with the remaining body of theory on this problem. This result points out the sensitivity of the results here to the method of derivation; in particular, theories which neglect terms of the order of terms that appear eventually in the equations to be solved (A_{xx} and B_{xx} here) lead to incorrect results. The splitting method employed by Kirby (1986) and Kirby and Vengayil (1988) appears to be a robust method.

4 Numerical results

Numerical solutions are obtained for the parameter range $0.5 \leq 2k/\lambda \leq 2.5$, $0^\circ \leq \theta \leq 85^\circ$, using second-order accurate centered finite differences applied to (5). Boundary conditions for the numerical problem are discussed in Kirby (1989). Results for the $n = 4$ Davies and Heathershaw barfield are shown in Figure 5. We see that the numerically predicted solution shows nearly total reflection at large angles of incidence, as well as very small reflection at $\theta = 45^\circ$, as predicted by the analytic theories developed here. The reflection coefficient does not drop identically to zero for $\theta = 45^\circ$ owing to the effect of nonresonant modes in the solution which are not accounted for in the analytic approaches.

In Figure 6, reflection coefficients for normally incident waves obtained numerically, from Mei's solution, and from the present analytical solution are compared. The numerical solution (solid line) is seen to obtain a somewhat higher maximum than in the analytic solutions, and the maximum is shifted to a slightly lower wavenumber. The two analytic solutions agree at resonance but deviate slightly away from resonance. The numerical solution also indicates that reflection is slightly stronger for the first lobe on the short wave side of the main resonance, in contrast to the prediction of the present analytic theory. The solution of Mei is therefore a somewhat more accurate representation of the numerical solution, although the two analytic results agree more closely with each other than they do with the numerical result. Overall, the deviation between the numerical and analytical results would not be resolvable within the accuracy of the Davies and Heathershaw (1984) data set.

5 Effects of frictional damping

The propagation of waves over a bar field is affected by a number of mechanisms which are not included in the analysis presented above. YL and Vengayil and Kirby (1988) have discussed some of the consequences of nonlinear interaction on the scattering process. In real applications, it is expected that a number of dissipative mechanisms could come into play. Bottom boundary layer damping would affect the waves moderately, causing a small decrease in the transmitted and reflected waves predicted by the theory described above. For bars fronting a beach face in relatively shallow water, the protruding bar crests could also induce breaking of steep incident waves, leading to significant reduction of incident energy over the bar field.

Here, we consider the effect of laminar frictional damping on the predicted reflection coefficient. Following Booij (1981) and Kirby (1986), we may extend the generalized mild-

slope equation to include damping effects according to

$$\tilde{\phi}_{tt} + W\tilde{\phi}_t - \nabla \cdot (p\nabla\tilde{\phi}) + (\omega^2 - k^2CC_g)\tilde{\phi} = 0 \quad (35)$$

or, for time-harmonic waves,

$$\nabla \cdot (p\nabla\tilde{\phi}) + k^2CC_g\tilde{\phi} + i\omega W\tilde{\phi} = 0 \quad (36)$$

Here, W is a generalized complex damping term. Following the derivation in section 2 leads to the coupled evolution equations

$$\tilde{A}_x = -\frac{W}{2C_g \cos \theta} \tilde{A} + iK \cos \theta \tilde{A} - \frac{\Omega_0 \alpha \cos \theta}{C_g} \left(\frac{k_{res}}{k} \right) \tilde{B} \quad (37)$$

$$\tilde{B}_x = \frac{W}{2C_g \cos \theta} \tilde{B} - iK \cos \theta \tilde{B} - \frac{\Omega_0 \alpha \cos \theta}{C_g} \left(\frac{k_{res}}{k} \right) \tilde{A} \quad (38)$$

where we have assumed that the dissipative effects act uniformly and equally on the incident and reflected waves. The new dissipative term may be absorbed in the previous derivation by defining a new complex detuning factor

$$\beta' = \beta - i\frac{W}{C_g \cos \theta} = -2K \cos \theta - i\frac{W}{C_g \cos \theta} \quad (39)$$

From this point, the derivations in section 2 follow through exactly, with the exception that the definition of P in (29) is replaced by

$$P = \frac{\Omega_0 \cos \theta}{C_g} \left[\left(\frac{\Omega}{\Omega_0} \right)^2 + i\frac{\Omega W}{\Omega_0^2 \cos^2 \theta} - \left(\frac{W}{2\Omega_0 \cos^2 \theta} \right)^2 - \alpha^2 \left(\frac{k_{res}}{k} \right)^2 \right]^{1/2} \quad (40)$$

For the case of laminar bottom boundary layer damping, an expression for W is given by (Liu, 1986)

$$W = (1 - i) \frac{gk^2}{\omega \cosh^2 kh} \sqrt{\frac{\nu}{2\omega}} \quad (41)$$

For laminar damping alone, the effects on the results given above are quite small, owing to the relatively short length of the bar field. The reflection coefficients with damping can be either smaller or larger than the coefficients without damping, due to the effect that damping has on the wave speed and wavelength. It is not anticipated that local damping over the bar field has any significant effects in any of the available laboratory data sets.

6 Discussion

The results of this and previous studies have shown that numerical solutions of a generalized mild-slope equation may be used to model the reflection of waves from simple (nearly sinusoidal) bar fields. A body of analytic approximations are also now available for providing estimates in the same situation.

Several recent studies have indicated that bottom configurations having multiple Fourier components can lead to additional reflection peaks appearing at difference wavenumbers resulting from the interaction of two or more individual bottom components (Belzons et al, 1991). This situation is not handled properly by the existing generalized mild-slope equation. The problem of these subharmonic resonances is being pursued further by the present author in the context of a generalization of the mild-slope equation to handle the presence of non-propagated modes.

Acknowledgement. This work was supported by the Office of Naval Research, contract N00014-90-J-1678.

Appendix A. Extension of Liu and YL results to the case of obliquely incident waves

The problem of specifying the evolution equations for the detuned interaction between surface waves and the sinusoidal bar field has been considered previously by Liu and YL, as well as by Kirby and Vengayil (1988). The study of Liu was restricted to normal incidence of linear waves in a channel with both bottom and side-wall corrugations, while the theory of YL was for the same channel configuration but for weakly nonlinear, weakly dispersive waves obeying the Boussinesq equations. Here, we consider the case of normal or oblique incidence of linear dispersive waves over an infinitely wide bar field, as in section 2, and extend the theories of Liu and YL accordingly. Section 3 of the main text gives a comparison between various features of these extended results and the results in section 2.

The YL approach is conceptually simpler than the Liu approach, and so we follow it first. We start by rewriting the governing equation as

$$\nabla^2 \tilde{\phi} + k^2 C C_g \tilde{\phi} = \frac{gk}{\omega C_g \cosh^2 kh} (\delta \nabla^2 \tilde{\phi} + \delta_x \tilde{\phi}_x) \quad (A1)$$

where we have used the fact that the mean depth is taken to be uniform and the bar field varies as $\delta(x)$ only. Employing the separation (4) in the main text reduces (A1) to

$$\phi_{xx} + l^2 \phi = \frac{gk}{\omega C_g \cosh^2 kh} (\delta \phi_{xx} + \delta_x \phi_x - m^2 \phi) \quad (A2)$$

We now make the separation into incident and reflected waves with slowly varying amplitudes, as specified in (10) and (17). These are substituted directly into (A2) without a prior splitting. An apparent ordering is made which equates the importance of slow derivatives of A and B with terms that are first order in δ . Terms of $O(\delta^2)$ are then dropped. Then, substituting the expression (1) for δ and retaining terms closest to resonance leads to the coupled equations

$$A_x = -\frac{\Omega_0}{C_g} \alpha_1 B e^{i\beta x} \quad (A3)$$

$$B_z = -\frac{\Omega_0}{C_g} \alpha_1 A e^{-i\beta z} \quad (\text{A4})$$

where

$$\alpha_1 = (\cos \theta)^{-1} \left(2 \left(\frac{k_{res}}{k} \right) \cos^2 \theta - 1 \right) \quad (\text{A5})$$

and where all other notations are as in the main text. The resulting model is similar in form to (18)-(19) in the main text, except for a change in the interaction coefficient. We remark that the principle reason for the differences between the present model and the model in the main text arises due to neglect of terms involving the factors δA_x and δB_x . If these terms were retained by effectively dividing through by the quantity p as in the main text, the resulting model would be equivalent.

For the case of normal incidence and in the limit of long wave theory, in interaction coefficient becomes

$$\frac{\Omega_0}{C_g} \alpha_1 \rightarrow \frac{D}{4h} (\lambda - k) \quad (\text{A6})$$

as in YL. At resonance, this reduces to $\lambda D/8h$ as in Kirby and Vengayil (1988), but it disagrees with their theory (again, based on a splitting procedure) away from resonance.

Turning to the work of Liu, we rewrite (A2) as

$$(p\phi_x)_x + l^2 C C_g \phi = 0 \quad (\text{A7})$$

We then employ the Liouville transformation

$$\phi = p^{-1/2} \zeta \quad (\text{A8})$$

and obtain

$$\zeta_{xx} - \frac{1}{2} p^{-1} p_{xx} \zeta + l^2 p^{-1} C C_g \zeta = 0 \quad (\text{A9})$$

Retaining terms to $O(\delta)$, this becomes

$$\zeta_{xx} + l^2 \zeta - \frac{4\Omega_0}{DkC_g} \left(\frac{\delta_{xx}}{2} + l^2 \delta \right) \zeta = 0. \quad (\text{A10})$$

We then employ the split into incident and reflected waves according to

$$\zeta = \psi^+(x) e^{ilx} + \psi^-(x) e^{-ilx}. \quad (\text{A11})$$

Direct substitution and the neglect of second-order terms in the slow derivatives leads to the set of coupled equations

$$\psi_x^+ = -\frac{\Omega_0}{C_g} \alpha_2 \psi^- e^{i\beta x} \quad (\text{A12})$$

$$\psi_x^- = -\frac{\Omega_0}{C_g} \alpha_2 \psi^+ e^{-i\beta x} \quad (\text{A13})$$

where

$$\alpha_2 = \cos \theta \left(2 \left(\frac{k_{res}}{k} \right)^2 - 1 \right) \quad (\text{A14})$$

For the case of normal incidence, the interaction coefficient in (A12-A13) reduces to

$$\frac{\Omega_0}{C_g} \alpha_2 \rightarrow \frac{\Omega_0}{k^2 C_g} \left(\frac{\lambda^2}{2} - k^2 \right) \quad (\text{A15})$$

as in Liu.

The main drawback in the derivation of (A12-A13) lies in the fact that the amplitudes ψ^+ and ψ^- are not properly decoupled. For example, compare the transformed incident wave to an untransformed form:

$$\psi^+ e^{ilx} = p^{1/2} A e^{ilx} \quad (\text{A16})$$

Taking x derivatives of both sides of (A16) leads to the expression

$$\psi_x^+ = p^{1/2} A_x + \frac{1}{2} p^{-1/2} p_x A. \quad (\text{A17})$$

We see that the derivative of ψ^+ contains a term which would resonate with the reflected, B wave, indicating that the incident-reflected wave separation is incomplete in this method.

References

- Belzons, M., Rey, V. and Guazzelli, E., 1991, "Subharmonic Bragg resonance for surface water waves", submitted to *Europhysics Letters*.
- Benjamin, T. B., Boczar-Karakiewicz, B. and Pritchard, W. G., 1987, "Reflection of water waves in a channel with corrugated bed", *J. Fluid Mech.*, 185, 249-274.
- Berkhoff, J. C. W., 1972, "Computation of combined refraction-diffraction", *Proc. 13th Intl. Conf. Coastal Engrng.*, Vancouver, 471-490.
- Dalrymple, R. A. and Kirby, J. T., 1986, "Water waves over ripples", *J. Waterway, Port, Coastal and Ocean Engrng.*, 112, 309-319.
- Davies, A. G. and Heathershaw, A. D., 1984, "Surface-wave propagation over sinusoidally varying topography", *J. Fluid Mech.*, 144, 419-443.
- Davies, A. G., Guazzelli, E. and Belzons, M., 1989, "The propagation of long waves over an undulating bed", *Phys. Fluids*, A 1, 1331-1340.
- Kirby, J. T., 1986, "A general wave equation for waves over rippled beds", *J. Fluid Mech.*, 162, 171-186.
- Kirby, J. T. and Vengayil, P., 1988, "Non-resonant and resonant reflection of long waves in varying channels", *J. Geophys. Res.*, 93, 10782-10796.
- Kirby, J. T., 1989, "Propagation of surface waves over an undulating bed", *Phys. Fluids*, A 1, 1898-1899.
- Kirby, J. T. and Anton, J. P., 1990, "Bragg reflection of waves by artificial bars", *Proc. 22nd Int. Conf. Coastal Engrng.*, Delft, 757-768.
- Liu, P. L.-F., 1986, "Viscous effects on evolution of Stokes waves", *J. Waterway, Port, Coast. and Ocean Engrng.*, 112, 55-63.
- Liu, P. L.-F., 1987, "Resonant reflection of water waves in a long channel with corrugated boundaries", *J. Fluid Mech.*, 179, 371-381.
- Mei, C. C., 1985, "Resonant reflection of surface water waves by periodic sandbars", *J. Fluid Mech.*, 152, 315-335.
- Mei, C. C., Hara, T. and Naciri, M., 1988, "Note on Bragg scattering of water waves by parallel bars on the seabed", *J. Fluid Mech.*, 186, 147-162.

Yoon, S. B. and Liu, P. L.-F., 1987, "Resonant reflection of shallow-water waves due to corrugated boundaries", *J. Fluid Mech.*, 180, 451-469.

List of Figures

1	Reflection coefficient and cutoff condition: solution of Mei, Hara and Naciri.	16
2	Reflection coefficient and cutoff condition: present solution.	17
3	% error in detuning parameter β based on Mei's theory and detuning parameter β based on present theory, for the cutoff condition.	18
4	Comparison of loci of zero reflection: - - - - -, present solution; - - - - -, Liu solution;, YL solution. ———, resonance curve.	19
5	Reflection coefficient computed numerically from (5).	20
6	Reflection coefficient at normal incidence. —, numerical solution, - - - -, present analytical solution,, Mei, Hara and Naciri solution.	21

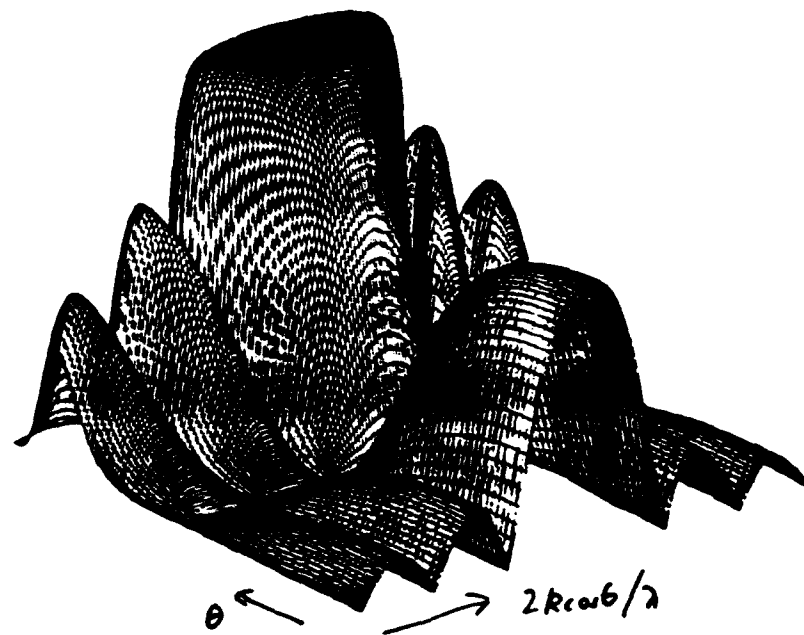
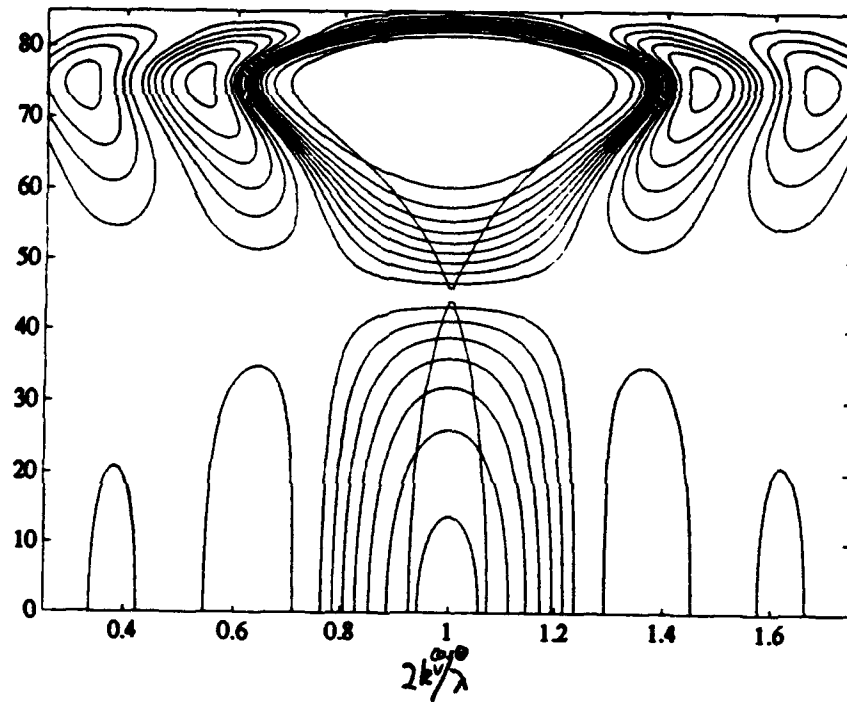


Figure 1: Reflection coefficient and cutoff condition: solution of Mei, Hara and Naciri.

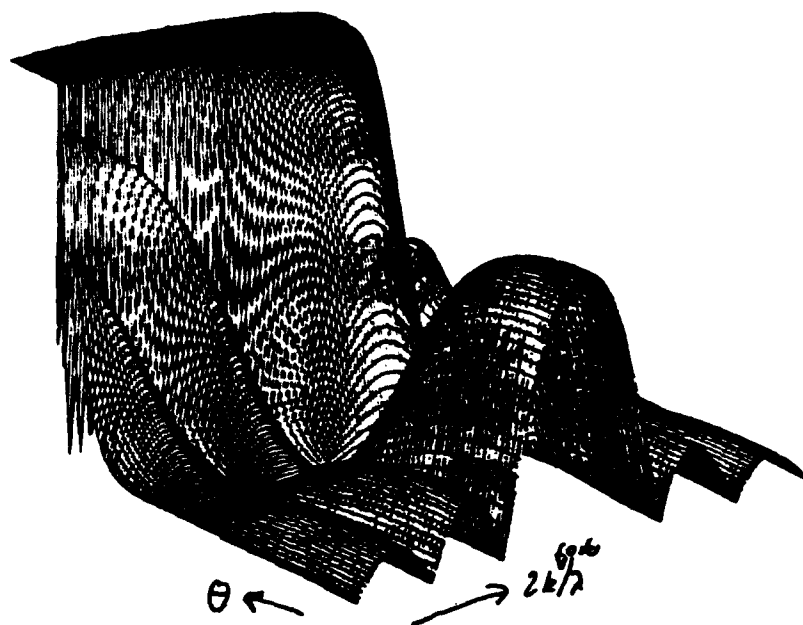
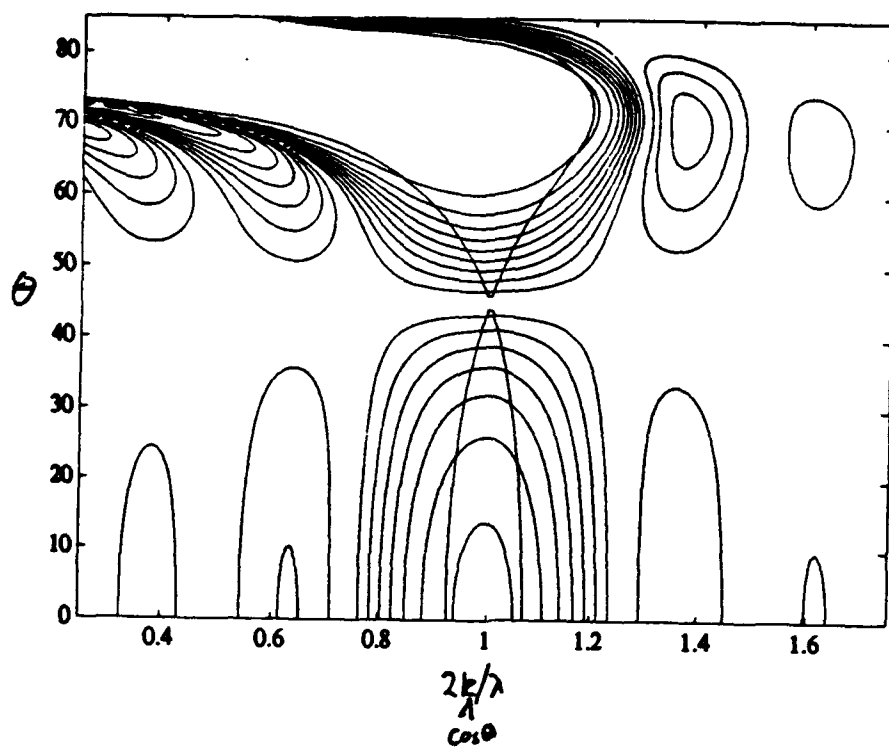


Figure 2: Reflection coefficient and cutoff condition: present solution.

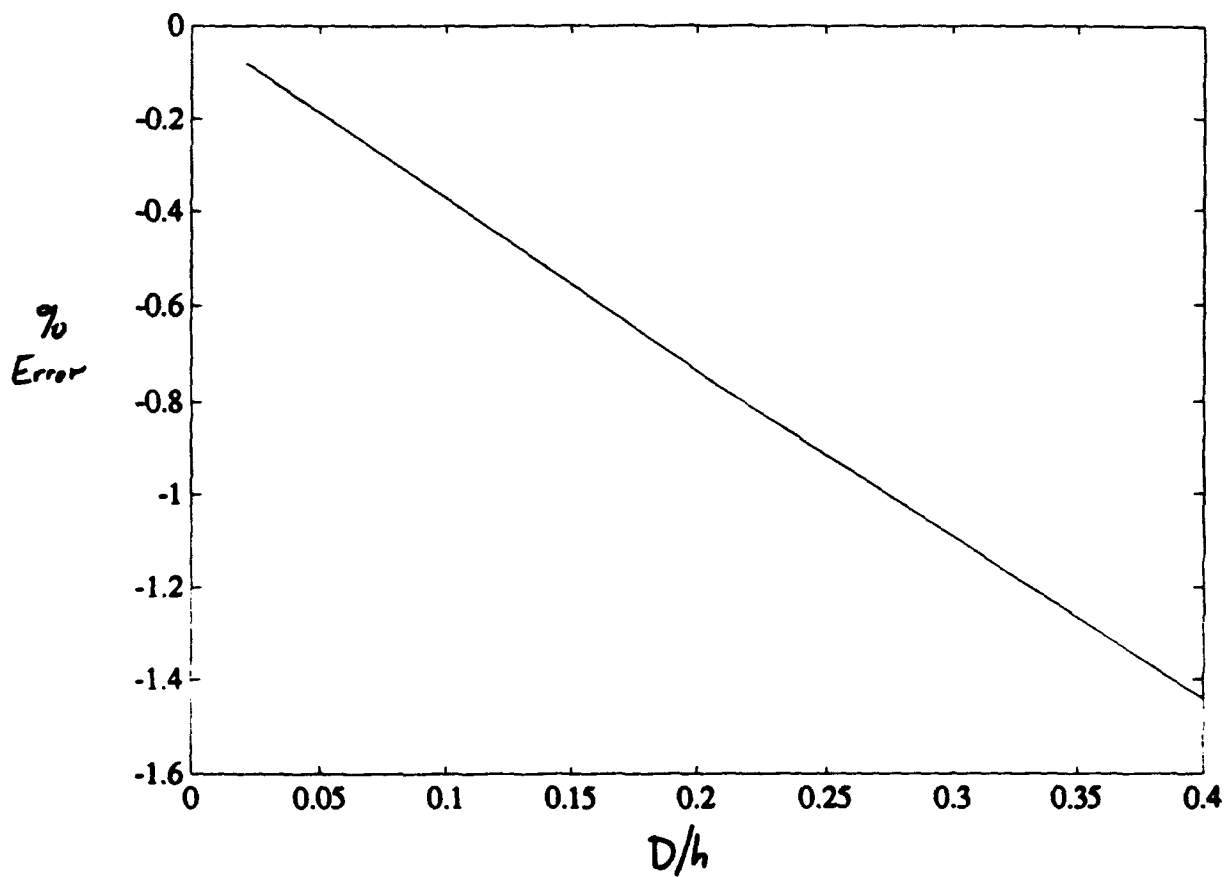


Figure 3: % error in detuning parameter β based on Mei's theory and detuning parameter β based on present theory, for the cutoff condition.

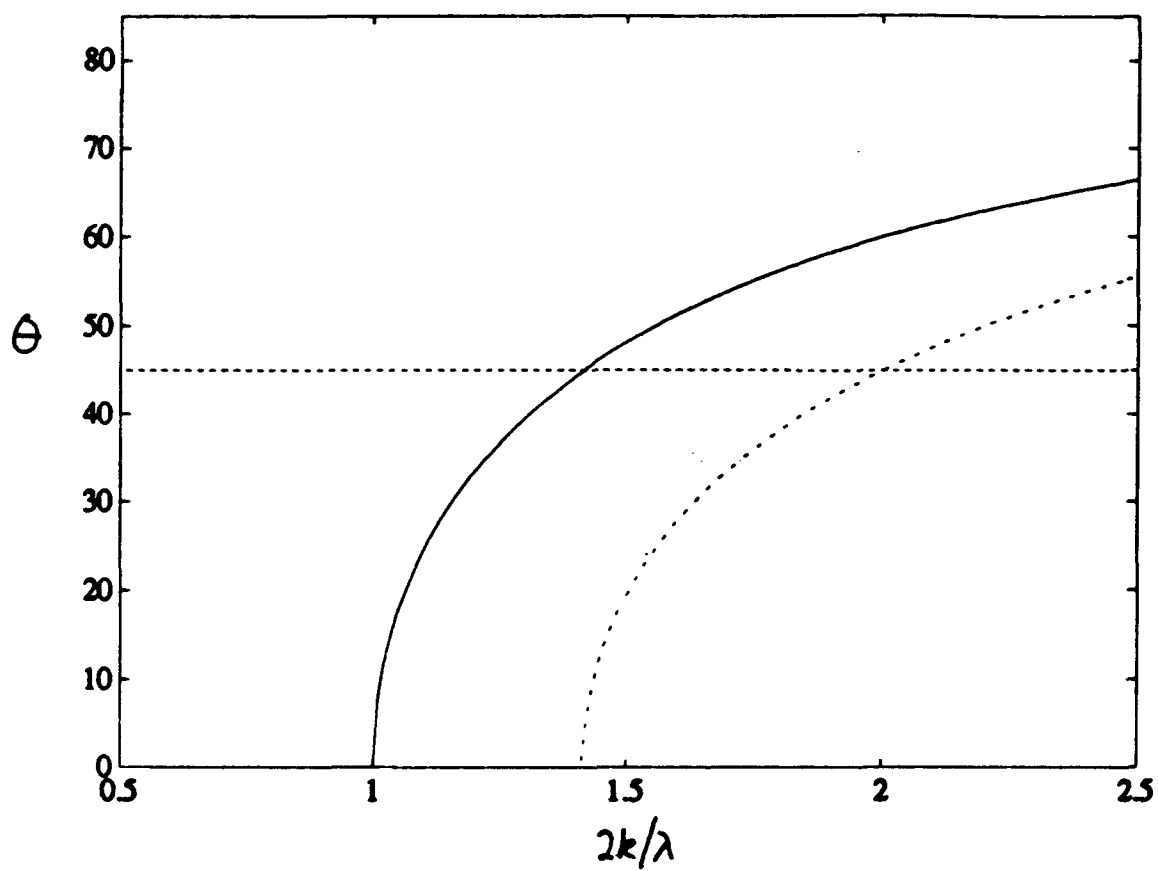


Figure 4: Comparison of loci of zero reflection: - - - - -, present solution; - · - · - · -, Liu solution; · · · · ·, YL solution. ———, resonance curve.

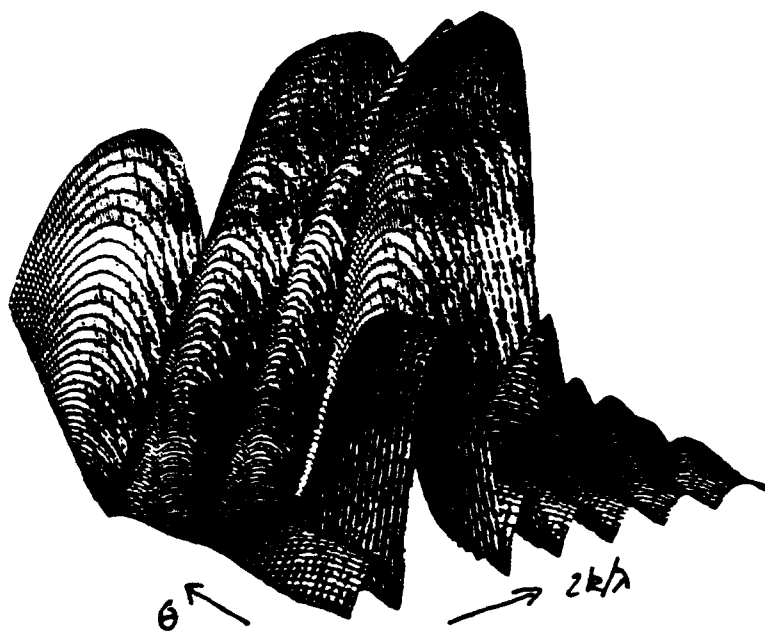
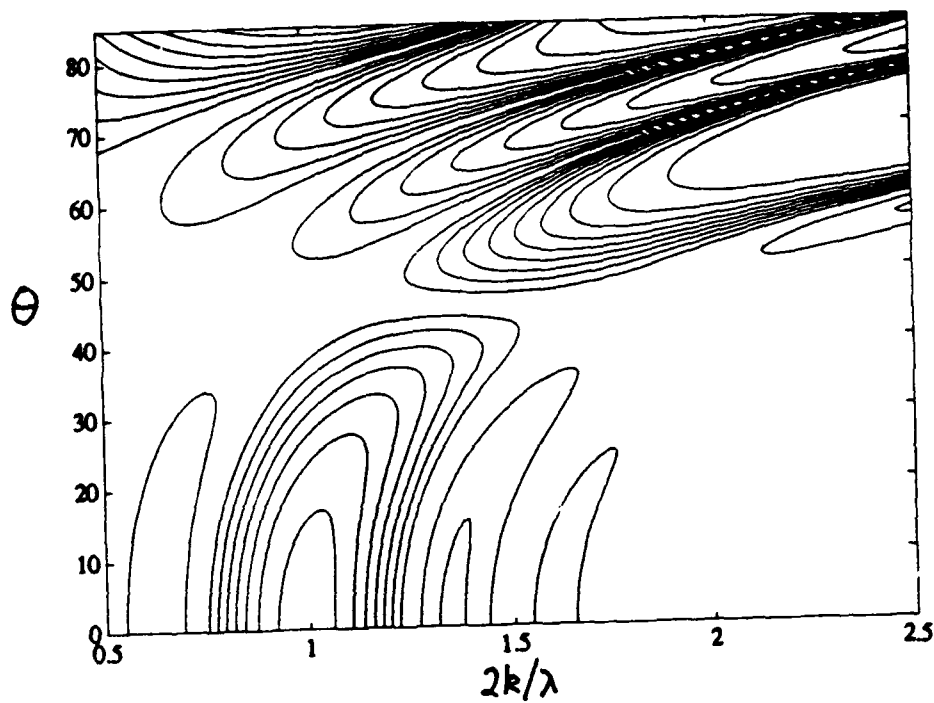


Figure 5: Reflection coefficient computed numerically from (5).

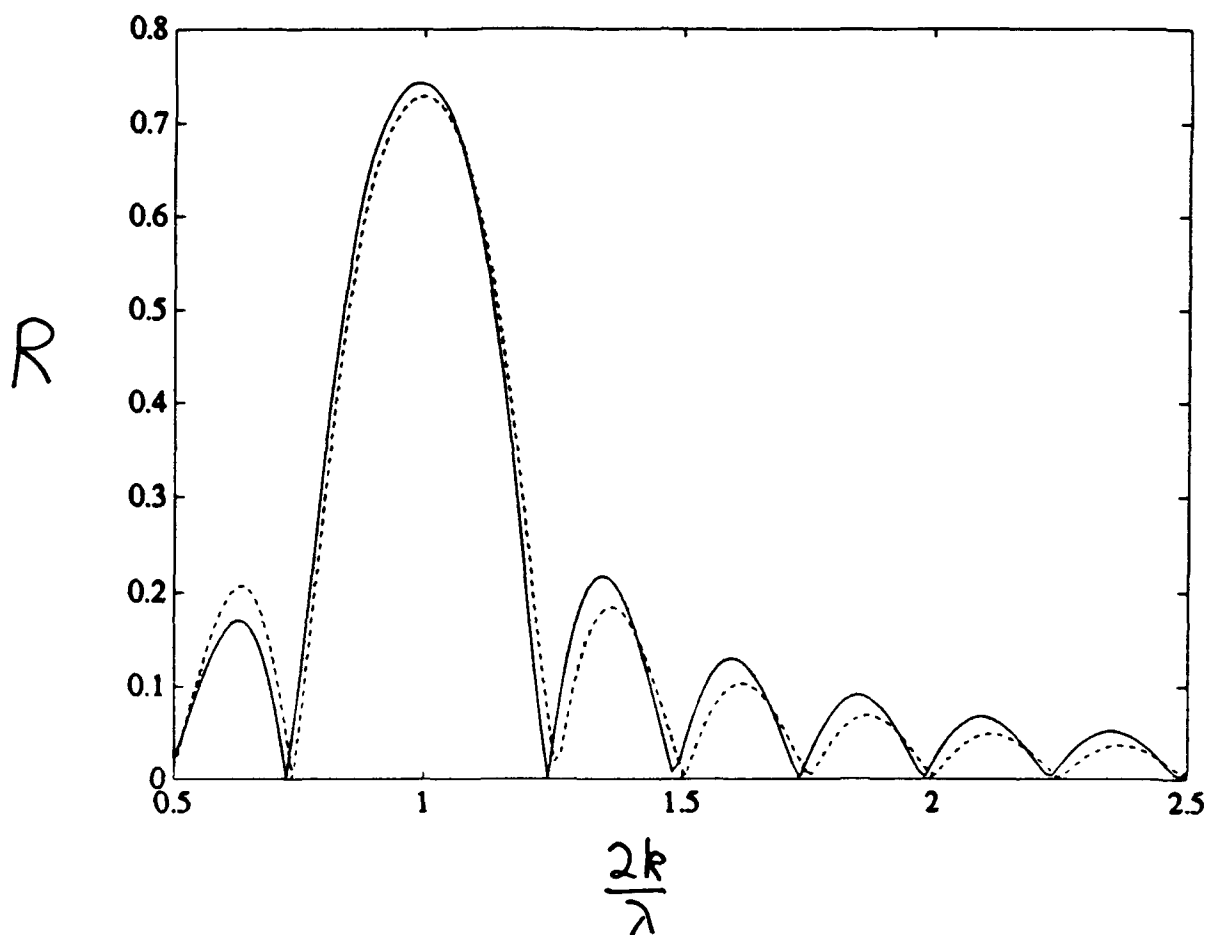


Figure 6: Reflection coefficient at normal incidence. —, numerical solution, - - - - , present analytical solution, ·····, Mei, Hara and Naciri solution.

Appendix E: A Discrete Angular Spectrum Model for Non-linear Shallow Water Waves. Part 1. Waves in Laterally Uniform Domains

submitted to *J. Fluid Mechanics*

A Discrete Angular Spectrum Model for Nonlinear Shallow Water Waves. Part 1. Waves in Laterally Uniform Domains

James T. Kirby

Center for Applied Coastal Research, Department of Civil Engineering
University of Delaware, Newark, Delaware 19716

Abstract

This paper describes the development of a model for the shoaling and refraction of an incident directional spectrum over beach topography. The present model is limited to topography which varies only in the on-offshore direction, but no restriction is made on allowed angles of incidence with respect to the shore-normal direction. Several approximations for restricted directional bandwidth are discussed, and several numerical examples are presented which illustrate the growth of significant harmonics resulting from the interaction of waves travelling at different directions. The model is verified in comparison to laboratory data for Mach reflection of cnoidal waves from a vertical plane wall. It is shown that the model provides a more accurate representation of the evolving wave field than does an earlier parabolic approximation, using the same laboratory data.

1 Introduction

As ocean surface waves propagate towards shore, they pass through a shoaling zone prior to breaking in which nonlinear interactions become strong and can significantly modify the wave train. This zone is characterized by weak frequency dispersion, since waves become relatively long compared to local water depth. In addition, the weak dependence on wavelength in the wave phase speed leads to the occurrence of strong nonlinear interactions at second-order in wave height. The combined effects of weak dispersion and nonlinearity may be modelled by the Boussinesq equations (discussed below in section 2), which serve as a reasonably accurate general purpose model for the domain in question as long as waves do not become too high.

Since the area being studied here can be quite extensive in comparison to the characteristic wavelength of the waves being modelled, the choice of an efficient numerical solution technique is crucial. The Boussinesq equations may be successfully solved by time-stepping techniques (Wu and Wu, 1983; Rygg, 1988 for example), but these methods are too inefficient for the spatial and temporal spans being considered in applications to an open coastal zone. Instead, various prior studies have found that it is efficient to decompose the time-dependent wave train into a stack of frequency components by Fourier decomposition, and then solve for the spatial evolution of each frequency mode. This is exactly the same kind

of manipulation that is done in Fourier analysis of data, and is valid as long as the wave train satisfies the requirements for the transform to exist. In field applications, the Fourier decomposition into a finite set of discrete frequencies under the assumption of periodicity is exactly the same as applying an FFT to data. Assumptions about stationarity of the process are implicit and should be kept in mind when determining if the present approach is useful.

The solution for the spatial behavior of each frequency component is itself involved. A number of studies (Freilich and Guza, 1984; Elgar and Guza, 1985 and 1986 and subsequent contributions) have considered only the shoreward propagation in one space dimension, and have shown that the resulting one-dimensional, first-order coupled mode equations are capable of modelling the evolution of the spectrum and bispectrum of shoaling waves, as verified by comparison with field measurements. Liu, Yoon and Kirby (1985; referred to here as LYK) alternately proposed a parabolic model for the shoreward propagation of each frequency component over two-dimensional topography, and verified the method in comparison to a laboratory experiment on the focussing of periodic long waves by topography. The parabolic model approach has never been used to study a field application, although such work is presently underway (Freilich et al, 1990b).

In this study, we derive a model for the evolution of each frequency mode in two dimensions, based on the angular spectrum approach. This approach has been applied to the study of intermediate depth waves by Dalrymple and Kirby (1988) and Dalrymple et al (1989). For the case of linear theory, the angular spectrum is usually posed as the continuous Fourier transform of the wave field in the longshore direction. Here, in keeping with the mental framework associated with the discrete transforms being employed in time, we impose longshore periodicity as well and obtain a discrete spectrum in longshore wavenumber. This frequency - longshore wavenumber spectrum is subsequently referred to as the *discrete angular spectrum*, as referred to in the title of this paper.

In section 2, we describe the reduction of the Boussinesq equation to a general model for the on-offshore behavior of each wave train resulting from Fourier decomposition of time and longshore direction. In this derivation, bathymetry is assumed to be uniform in the longshore direction. In section 3, this general formulation is restricted to the case of waves propagating towards shore, and the angular spectrum is introduced as the slowly varying amplitude of each component wave. The evolution equations are described. An equation describing the gain or loss of energy in each shoaling wave mode is derived, and an angular bispectrum is introduced which could be used to study the strength of coupling across a range of wave directions. Several reductions of the full model are considered which would reflect a narrowing of allowed range of wave directions in the modelled wave field.

In section 4, we introduce some simple examples which illustrate the strength of interaction that may occur between waves travelling in different directions, relative to interactions occurring in waves travelling in the same direction. In particular, the characteristic hexagonal stem and saddle structure associated with solutions for short crested waves (Segur and Finkel, 1985) is seen to be related to the presence of a strong second-harmonic component resulting from the interaction of the two obliquely interacting primary waves. (This observation would also follow from an examination of the spectrum of a Genus 2 KP equation solution (Segur and Finkel), but this interpretation has not been discussed extensively before.)

The model developed here is applicable both to simple periodic waves generated in the laboratory environment and to irregular, "random" waves in the field environment. In this paper, we concentrate on a model verification conducted from the first viewpoint. In section 5, the model is tested against laboratory data obtained by Hammack, Scheffner and Segur (1990) who investigated the development of a Mach stem arising during the glancing-angle reflection of a cnoidal wave by a vertical wall. The model developed here is tested against the laboratory data along with an existing model based on the parabolic approximation described in LYK. (The case of Mach reflection of a cnoidal wave has been studied using the parabolic approximation by Yoon and Liu (1989); however, no comparison to data was provided in that study.) The spectral model is shown to give a more accurate representation of the data than the parabolic model over the entire range of angles of incidence considered.

2 The basic model

We first establish the form of a model for waves in a laterally unrestricted domain. A Cartesian coordinate system is adopted which has x pointed in the onshore direction and y pointing alongshore. Depth is assumed to vary as $h(x)$ only. We take as a starting point the variable depth Boussinesq equations as given by Peregrine (1967):

$$\eta_t + \nabla \cdot (h\mathbf{u}) + (\epsilon)\nabla \cdot (\eta\mathbf{u}) = 0 \quad (1)$$

$$\mathbf{u}_t + (\epsilon)\mathbf{u} \cdot \nabla \mathbf{u} + g\nabla\eta = (\mu^2)\left\{\frac{h}{2}\nabla(\nabla \cdot (h\mathbf{u}_t)) - \frac{h^2}{6}\nabla(\nabla \cdot \mathbf{u}_t)\right\} \quad (2)$$

Here, η is the surface displacement and \mathbf{u} is the horizontal wave-induced velocity. The equations are kept in dimensional form; the scaling parameters ϵ for nonlinearity and μ^2 for weak dispersion are present only schematically and will be subsequently dropped. We will assume that either bottom slope or the amplitude of bottom features (as scaled by water depth) are also small and hence the model will be developed to leading order in nonlinearity, dispersion, and domain inhomogeneity. This leads to immediate neglect of bottom slope effects in the dispersive terms of (2). Using the linear portion of (1), we may then write (2) in the reduced form

$$\mathbf{u}_t + \mathbf{u} \cdot \nabla \mathbf{u} + g\nabla\eta + \frac{h}{3}\nabla\eta_{tt} = 0. \quad (3)$$

We now make the following assumptions. First, the model will be applied to time-periodic wave trains, where periodicity is in the sense of either a regular wave train, or of a discrete FFT over a finite length of sampled data. This assumption has been routinely applied in the spectral sense in the one-directional shoaling model of Freilich and Guza (1984) (see also Elgar and Guza; 1985, 1986). Its interpretation in the regular wave case is straightforward, with the wave being separated into its harmonic components (Rogers and Mei, 1978; LYK).

Secondly, the wave field will be assumed to be periodic in the transverse y direction. This corresponds again to a fixed longshore wavelength in the regular wave case, or to periodicity over a long spatial interval in the spectral sense.

The governing equations are first split into coupled elliptic models for separate harmonic components. Following LYK, we write the surface displacement and velocity as

$$\eta = \sum_{n=0}^N \frac{\eta_n(x, y)}{2} e^{-in\omega t} + c.c. \quad (4)$$

$$\mathbf{u} = \sum_{n=0}^N \frac{\mathbf{u}_n(x, y)}{2} e^{-in\omega t} + c.c. \quad (5)$$

Substitution of (4) and (5) in (1) and (3) and subsequent elimination of the velocity leads to the following model equation for the η_n in the horizontal plane:

$$n^2 \omega^2 \eta_n + \nabla \cdot (G_n \nabla \eta_n) + [n.l.t.]_n = 0; \quad n = 1, \dots, N \quad (6)$$

Here, $[n.l.t.]_n$ denotes the nonlinear interactions with other discrete frequency components which are sorted by means of the rules for triad interactions applied to the time dependence. The term is given in Appendix A. The mode $n = 0$ corresponding to the steady, wave-induced setdown is neglected since it is at most second order in the largest wave amplitudes present (see LYK). Also,

$$G_n(x) = gh(x) - \frac{1}{3} n^2 \omega^2 h^2(x). \quad (7)$$

We now apply a spectral transform to the y dependence of the wavefield, assuming propagation is to be considered in the on-offshore ($\pm x$) direction. We consider here the case of an unbounded lateral domain and a wavefield which is periodic over the basic interval L . We then represent $\eta_n(x, y)$ as

$$\eta_n(x, y) = \sum_{m=-M}^M \eta_n^m(x) e^{im\lambda_0 y} \quad (8)$$

where

$$\lambda_0 = \frac{2\pi}{L}. \quad (9)$$

Substituting (8) in (6) and neglecting x - derivatives of small terms in G_n then leads to a set of coupled second-order ODE's for the η_n^m , given by

$$\begin{aligned} \frac{G_n}{gh} \eta_{n,xx}^m + \frac{h_x}{h} \eta_{n,x}^m + (\gamma_n^m)^2 \eta_n^m + \frac{1}{3} m^2 n^2 \lambda_0^2 k^2 h^2 \eta_n^m + \frac{1}{gh} [n.l.t.]_n^m &= 0; \\ n = 1, \dots, N; \quad m = -M, \dots, M. \end{aligned} \quad (10)$$

where $[n.l.t.]_n^m$ now represents triad interactions satisfying resonance conditions in t and y . The nonlinear term is again given in Appendix A. Here, k is the wavenumber determined by the lowest order dispersion relation

$$\omega^2 = gk^2 h. \quad (11)$$

Also,

$$(\gamma_n^m)^2 = n^2 k^2 - m^2 \lambda_0^2 \quad (12)$$

For fixed n, k, λ_0 , large values of m will make γ_n^m imaginary, which corresponds to modes which are exponential rather than oscillatory in x in the linear approximation. In the linear case, the presence of these modes in the initial conditions would be interpreted in the same

light as the presence of evanescent modes in the general wavemaker problem (see Dalrymple and Kirby, 1988). However, the interpretation in the case of possible nonlinear forcing of the offshore portion of trapped modes in the nearshore region is non-trivial and will need to be considered carefully in applications where the inclusion of this effect is desired. In addition, nonlinearity could force the propagation of modes that would not be present in a linearized wave field, and which could affect a detailed representation of an individual wave. At present, the range of M at each value of n may be restricted to $M_n \leq nk/\lambda_0$ in order to eliminate forcing of these modes arbitrarily.

3 Shoaling waves

The model developed in the previous section allows for the onshore and offshore propagation of the directional spectrum components. For the remainder of the present paper, attention is restricted to waves propagating onshore, or in the positive sense with respect to the x coordinate.

3.1 The Model Equations

Based on the linear, nondispersive portion of the model (10), we assume that the incident wave may be written in the form

$$\eta_n^m(x) = A_n^m(x) e^{in \int k \tilde{\gamma}_n^m dx} \quad (13)$$

where it is assumed that the x dependence of A , k and $\tilde{\gamma}$ is on a slow scale of $O(\epsilon)$, and where

$$\tilde{\gamma}_n^m = (1 - (\frac{m}{n})^2 (\frac{\lambda_0}{k})^2)^{1/2} = \frac{\gamma_n^m}{nk} \quad (14)$$

(where the positive root is taken). The amplitudes A represent the discrete angular spectrum being considered here, and are allowed to vary owing to refraction, shoaling, dispersion and nonlinear interaction. (It would be possible to absorb shoaling and refraction effects by the use of the usual linear refraction formulae; this step is not taken here.) Substitution of (13) in (10) leads to the spectral model for incident waves, given by

$$\begin{aligned} & \tilde{\gamma}_n^m A_{n,x}^m + \frac{(kh \tilde{\gamma}_n^m)_x}{2kh} A_n^m - \frac{1}{6} i n^3 k^3 h^2 A_n^m \\ & + \frac{ink}{8h} \left\{ \sum_{l=1}^{n-1} \sum_{p=P_1}^{P_2} I_{n,l}^{m,p} A_l^p A_{n-l}^{m-p} e^{i \int \Theta_{n,l}^{m,p} dx} + 2 \sum_{l=1}^{N-n} \sum_{p=P_3}^{P_4} J_{n,l}^{m,p} A_l^{p*} A_{n+l}^{m+p} e^{i \int \Upsilon_{n,l}^{m,p} dx} \right\} = 0; \\ & n = 1, \dots, N; \quad m = -M_n, \dots, M_n. \end{aligned} \quad (15)$$

Here, $(\cdot)^*$ denotes the complex conjugate. The limits of summation $P_1 - P_4$ are given by

$$\begin{aligned} P_1 &= \max(-M_l, -M_{n-l} + m) \\ P_2 &= \min(M_l, M_{n-l} + m) \\ P_3 &= \max(-M_l, -M_{n+l} - m) \\ P_4 &= \min(M_l, M_{n+l} - m) \end{aligned} \quad (16)$$

The interaction coefficients I and J are given by

$$I_{n,l}^{m,p} = 1 + [\tilde{\gamma}_l^p \tilde{\gamma}_{n-l}^{m-p} + \frac{p}{l} \frac{m-p}{n-l} (\frac{\lambda_0}{k})^2] \cdot [1 + (\frac{m}{n})^2 (\frac{\lambda_0}{k})^2 + \frac{(l \tilde{\gamma}_l^p + (n-l) \tilde{\gamma}_{n-l}^{m-p})^2}{n^2}] \quad (17)$$

$$J_{n,l}^{m,p} = I_{n,-l}^{m,-p}. \quad (18)$$

The phase arguments Θ and Υ represent the basic mismatch in the x direction of the triads chosen based on perfect matching in y and t . Generally, the only components which experience complete resonance in the long wave limit must have parallel propagation directions; all obliquely interacting components are somewhat detuned. The phase arguments are given by

$$\Theta_{n,l}^{m,p} = lk\tilde{\gamma}_l^p + (n-l)k\tilde{\gamma}_{n-l}^{m-p} - nk\tilde{\gamma}_n^m \quad (19)$$

$$\Upsilon_{n,l}^{m,p} = \Theta_{n,-l}^{m,-p} \quad (20)$$

The spectral model (15) is a set of coupled first order ODE's which are solvable by standard techniques. Results presented in sections 4 and 5 were obtained using a standard 4th-order Runge-Kutta scheme with fixed step size and no error checking. Presently, extensions of the model using error control and adaptive step size are being tested and will likely be the vehicle for further field testing of the model beyond the scope of the present study.

The model developed here allows for coupling and energy transfer between spectral modes with different directions and frequencies as the wave field evolves in the shoreward direction. For the case when modes with real wavenumbers $\tilde{\gamma}_n^m$ are retained, an energy equation for each mode may be constructed by multiplying (15) by A_n^{m*} and adding the resulting equation to its complex conjugate, to get

$$\begin{aligned} & \tilde{\gamma}_n^m |A_n^m|^2 + \frac{(kh\tilde{\gamma}_n^m)_x}{kh} |A_n^m|^2 \\ & - \frac{nk}{4h} \left\{ \sum_{l=1}^{n-1} \sum_{p=P_1}^{P_2} I_{n,l}^{m,p} \operatorname{Im}(B_{l,n-l}^{p,m-p} e^{i \int \Theta_{n,l}^{m,p} dx}) + 2 \sum_{l=1}^{N-n} \sum_{p=P_3}^{P_4} J_{n,l}^{m,p} \operatorname{Im}((B_{l,n}^{p,m})^* e^{i \int \Upsilon_{n,l}^{m,p} dx}) \right\} = 0 \end{aligned}$$

$n = 1, \dots, N; \quad m = -M_n, \dots, M_n \quad (21)$

The quantity B introduced here is given by

$$B_{n,l}^{m,p} = A_n^m A_l^p (A_{n+l}^{m+p})^* \quad (22)$$

and may be thought of as being a discrete representation of a *directional bispectrum*. Analysis of the magnitude of this term should provide a measure of the strength of nonlinear coupling across a range of directions in a field spectrum. This aspect of the analysis is not pursued further here. In (21), the first appearance of the directional bispectrum corresponds to coupling between the present mode n and modes of lower frequency; the present wave takes the role of a sum wave in a higher-harmonic excitation. The second appearance of bispectral coupling corresponds to cases where the present mode has either the lowest or middle frequency in a triad.

3.2 Approximations for small angles of incidence

Parabolic modeling schemes have drawn a reasonable amount of interest as a way of computing wave fields in the coastal environment. Since these models presuppose a narrow range of wave propagation directions relative to the full 180° band allowed here, it is of some interest to see how the present model could be reduced in scope to correspond to the assumptions made in developing the parabolic approximation. (Note that the parabolic model computations presented in section 5 were made using the standard model in physical space, and are not an application of the results derived here).

We consider first the effect of assuming that the spread of wave directions about a central angle is small. In particular, we choose the central angle as $\theta = 0^\circ$, coincident with the x axis. The effect of having waves propagating at close to normal incidence is to lengthen the longshore interval needed in order to assume spatial periodicity. Thus, λ_0/k in (14-20) would be effectively small. Further restricting attention to small angle deviations from the normal direction limits consideration to relatively small values of m . Consequently, the $\bar{\gamma}$ may be approximated according to

$$\bar{\gamma}_n^m = 1 - \frac{1}{2} \left(\frac{m}{n} \right)^2 \left(\frac{\lambda_0}{k} \right)^2 + O \left(\frac{\lambda_0}{k} \right)^4 \quad (23)$$

which is consistent with the usual small-angle form of the parabolic approximation. The resulting modifications to the phase arguments and interaction coefficients are given by (to the same level of approximation)

$$\begin{aligned} I_{n,l}^{m,p} &= 3 - \left(\frac{\lambda_0}{k} \right)^2 \frac{(ml - np)^2 (n^2 + ln - l^2)}{n^2 l^2 (n - l)^2} \\ &= \frac{3}{\left(1 + \frac{1}{3} \left(\frac{\lambda_0}{k} \right)^2 \frac{(ml - np)^2 (n^2 + ln - l^2)}{n^2 l^2 (n - l)^2} \right)} \end{aligned} \quad (24)$$

$$\Theta_{n,l}^{m,p} = -\frac{\lambda_0^2}{2k} \left[\frac{(ml - np)^2}{nl(n - l)} \right] \quad (25)$$

where the second form in equation (24) results from the need to avoid a zero arising at finite angles in the first approximation. This model then corresponds to the case where angular variations between interacting wave components are small, but where no direct correspondence is made between the smallness of this dependence and the other small parameters in the problem. A further reduction in complexity would occur if we were to make the full set of restrictions appropriate to the parabolic approximation of the KP equation (Kadomtsev-Petviashvili, 1970), which is available in variable depth form from LYK. Carrying the ordering restrictions to their fullest extreme, we would conclude that, since the nonlinear terms are already of small size, only $O(1)$ information should be retained

in their coefficients. This further assumption reduces the coefficient I to

$$I_{n,l}^{m,p} = 3 \quad (26)$$

for all components of the wave train.

To date, the various forms of small-angle approximations have not been fully tested for their ability to model the general (unrestricted angle) evolution of a wave train. The existence of various approximations of the full governing equations leads to the question of whether the approximate interaction coefficients may be applied in a directional wave calculation with finite directional bandwidth. For example, if the presence of detuning effectively nullifies the nonlinear interaction in a particular triad before the point is reached where the interaction coefficient deviates significantly from one of its small-angle forms, then the small-angle forms may be retained in the full governing equations and sums over transverse mode numbers may be limited to the bandwidth contributing to resonance. Support for this hypothesis is fragmented, but comes from both numerical and experimental results indicating the large angular range for which the KP equation produces reasonably valid results. For example, Kirby et al (1988) have demonstrated that the KP model accurately describes reflection of solitary waves by a wall, in comparison with data obtained by Melville(1980) and with numerical solutions of the full Boussinesq theory by Funakoshi (1981). However, these computations are limited to the near field of the start of the reflecting wall and do not adequately describe far field behavior. The reflection pattern is reproduced for angles of incidence well beyond the critical angle for producing a Mach stem, as defined theoretically by Miles (1977), at least for short distances in a wave channel. Similarly, Hammack et al (1989) have demonstrated that the theory of Segur and Finkel (1985) for KP solutions of biperiodic (short-crested) waves may be applied accurately to wave trains having essentially no apparent scale distinction in the underlying $x - y$ parallelogram.

The determination of the validity of the KP approximation relative to the full Boussinesq equation will require careful studies with models of the present type and with time-dependent studies for transient phenomena. The results in section 4 and 5 are a start towards such a study, and indicate that the range of validity of the small angle approximations may be quite limited, when actual computational evolution of the wave field is considered.

4 Analysis for a simplified wave field

Before moving to model - data comparison, we consider a simple example which illustrates the strength of possible triad interactions occurring between waves travelling at different directions, relative to interactions occurring between waves travelling in the same direction. For this example, we consider the case of the oblique interaction of two synchronous $n = 1$ modes oriented at $\pm\theta$ with respect to x ($m = \pm 1$, representing a linear short-crested wave train), which interact to form $2n = 2$ modes oriented with x ($m = 0$, the sum interaction) and at $\pm\theta$ with respect to x ($m = \pm 2$, the self-interaction of each linear mode). Water depth is assumed to be constant. We further assume that the oblique modes are equal in amplitude ($A_1^1 = A_1^{-1}, A_2^2 = A_2^{-2}$) and obtain a reduced set of three equations. For this reduced case involving only one wave-angle θ , it is convenient to express λ_0 in terms of k and θ . We take $\lambda_0 = k \sin \theta$ for $n = 1, m = \pm 1$. We further nondimensionalize all A 's by $A_1(0)$ and x by k^{-1} and obtain the equations

$$\gamma A_{1,x}^1 - \frac{i}{6}\mu^2 A_1^1 + \frac{i}{4}\epsilon(J A_1^{1*} A_2^0 e^{i\Theta x} + 3 A_1^{1*} A_2^2) = 0 \quad (27)$$

$$A_{2,x}^0 - \frac{4i}{3}\mu^2 A_2^0 + \frac{i}{2}\epsilon I (A_1^1)^2 e^{-i\Theta x} = 0 \quad (28)$$

$$\gamma A_{2,x}^2 - \frac{4i}{3}\mu^2 A_2^2 + \frac{3i}{4}\epsilon (A_1^1)^2 = 0 \quad (29)$$

where

$$\gamma = \cos \theta \quad (30)$$

$$J = 1 + \cos \theta (6 - 4 \cos \theta) \quad (31)$$

$$I = 3 - 5 \sin^2 \theta + 2 \sin^4 \theta \quad (32)$$

$$\Theta = 2(1 - \cos \theta) \quad (33)$$

Equations (27-29) admit a corresponding conservation law

$$2 \cos \theta (|A_1^1|^2 + |A_2^2|^2) + \frac{J}{I} |A_2^0|^2 = \text{constant} \quad (34)$$

For the case of a small angle approximation consistent with the information in equations (24) and (25), we obtain the approximations $\cos \theta \rightarrow 1 - \frac{1}{2} \sin^2 \theta$, $J \rightarrow 3 + \sin^2 \theta$, $I \rightarrow 3/(1 + (5/3) \sin^2 \theta)$ and $\Theta \rightarrow \sin^2 \theta$. For the parabolic model used in section 5, I and J further reduce to $I = J = 3$. The resulting evolution is expected to be dependent on $\mu^2 = (kh)^2$, $\epsilon = A_1(0)/h$ and θ . We are interested in testing the approximate models as θ increases for fixed values of μ^2 and ϵ , and in studying the resulting interactions. Figure 1 gives plots of $I(\theta)$, $J(\theta)$ and $\Theta(\theta)$ and their small angle approximations over the range $0^\circ \leq \theta \leq 90^\circ$.

4.1 Steady solutions

The three coupled evolution equations may be solved simply for the case of a steady wave of permanent form. Letting

$$\begin{aligned} A_1^1 &= \alpha \exp\left(\frac{i\mu^2 x}{6\gamma}\right) \\ A_2^0 &= \beta \exp\left(\frac{4}{3}i\mu^2 x\right) \\ A_2^2 &= \rho \exp\left(\frac{4}{3}\frac{i\mu^2 x}{\gamma}\right) \end{aligned} \quad (35)$$

leads to elimination of the dispersive terms and gives the revised equations

$$\gamma \alpha_x + \frac{i\epsilon J}{4} \alpha^* \beta e^{i\Delta_1 x} + \frac{3i\epsilon}{4} \alpha^* \rho e^{i\Delta_2 x} = 0 \quad (36)$$

$$\beta_x + \frac{i\epsilon I}{2} \alpha^2 e^{-i\Delta_1 x} = 0. \quad (37)$$

$$\gamma \rho_x + \frac{3i\epsilon}{4} \alpha^2 e^{-i\Delta_2 x} = 0. \quad (38)$$

where

$$\Delta_1 = \Theta + \frac{4}{3}\mu^2 - \frac{1}{3}\frac{\mu^2}{\gamma} \quad (39)$$

$$\Delta_2 = \frac{\mu^2}{\gamma} \quad (40)$$

We then seek steady solutions of the form

$$\alpha = a e^{i\delta_1 x}; \quad \beta = b e^{i\delta_2 x}; \quad \rho = c e^{i\delta_3 x} \quad (41)$$

where a, b, c are real amplitudes and the δ 's are phases. Defining $\epsilon = A_1^1(0)/h$, we then take $a = 1$. Substitution of (41) in (36-38) and use of the properties of the amplitudes leads to the conditions

$$\delta_2 - 2\delta_1 + \Delta_1 = 0, \quad (42)$$

$$\delta_3 - 2\delta_1 + \Delta_2 = 0. \quad (43)$$

with

$$\delta_1 = -\frac{\epsilon J b}{4\gamma} - \frac{3\epsilon c}{4\gamma}; \quad \delta_2 = -\frac{\epsilon I}{2b}; \quad \delta_3 = -\frac{3\epsilon}{4\gamma c} \quad (44)$$

The solution is then given by

$$c = \frac{3\epsilon b}{2\gamma[I\epsilon + 2\Delta'_1 b]}, \quad (45)$$

where $\Delta'_1 = \Delta_2 - \Delta_1$, and a cubic equation for b given by

$$(2J\Delta'_1)b^3 + \left(\epsilon I J + \frac{4\gamma\Delta_1\Delta'_1}{\epsilon} + \frac{9\epsilon}{2\gamma}\right)b^2 + [2\gamma I(\Delta_1 - \Delta'_1)]b - \epsilon\gamma I^2 = 0. \quad (46)$$

In the parameter ranges of interest ($0 \leq (\mu^2, \epsilon) \leq 0.5$, $0^\circ \leq \theta \leq 90^\circ$), the roots of (46) are typically real and distinct. However, only one root leads to a positive value for c and hence a co-directional, in-phase harmonic for each individual primary wave. This root is taken to be the physically plausible solution.

As $\theta \rightarrow 90^\circ$, the solutions of (46) become difficult to evaluate numerically. $\theta = 90^\circ$ represents primary waves travelling in opposite directions; these waves do not interact at leading order (Rogers and Mei, 1978) and hence b drops to 0 in this limit. Therefore, solutions for c are obtained directly from a truncated, two equation model, which gives

$$\delta_1 = -\frac{3\epsilon c}{4\gamma}; \quad \delta_3 = -\frac{3\epsilon}{4\gamma c}; \quad c = \frac{1}{2} \left(2 + \left(\frac{2\mu^2}{3\epsilon} \right)^2 \right)^{1/2} - \frac{\mu^2}{3\epsilon} \quad (47)$$

where the positive root for c is chosen. This result is utilized if either of the coefficients of the zeroth and first order terms in (46) fall below 10^{-5} in absolute value. This limit does not have a great deal of practical importance in the present context.

Figure 2 presents solutions for the harmonic amplitudes b and c for $\mu^2 = 0.36$ and a range of ϵ and θ values. The value of μ^2 is chosen to correspond approximately to the tests in section 5. The most striking feature of the result is that the amplitude b of the sum-wave component at normal incidence exceeds the amplitude c of the inline second harmonics of each oblique primary wave for sufficiently small angles of incidence. This result is not immediately intuitive, since any triad based on oblique components would necessarily be more detuned than the corresponding triad based on second-harmonic resonance. See Figure 3 for the geometry of several hypothetical detuned triads whose component lengths are determined from the lowest order relation (11). The results in Figure 2 indicate that the result of the detuned triad interaction actually dominates the higher harmonic contents for angles of intersection between the two primary waves as large as $50^\circ - 60^\circ$. Of course, the conclusion that detuned interactions are dominating over more closely tuned interactions is an artifact, in this case, of the assumption that the component wavenumbers are given by the linear non-dispersive theory. In a permanent-form wave, nonlinearity distorts all component wavenumbers in such a way that components satisfying resonance conditions in frequency and longshore wavenumber also satisfy resonance conditions in on-offshore wavenumber. If this were not true, the components would have different wavelengths in the x direction and permanent form would not be retained. The short crested wave field computed here could be regarded as being a truncated form of the Genus 2 KP solution of Segur and Finkel (1985) in the event that the intersection angle of the two primary waves approaches zero (and KP scaling restrictions are satisfied). Conversely, retaining higher harmonics and determining solutions of the full problem would provide the large angle extension of the KP solution.

Figure 4 shows a plot of two periods of the wavefield for the case $\mu^2 = .36, \epsilon = .1, \gamma = 0.88$, which corresponds reasonably closely to the test condition CR38 discussed in section 5. For this case, $b = 0.15522$ and $c = 0.18204$; the in-line and center angle second harmonic components are nearly balanced. The resulting wave field exhibits the hexagonal form characteristic of short-crested shallow water waves, as discussed in Segur and Finkel (1985) and Hammack et al (1989). Wavefields dominated by the center angle component b give the appearance of being long crested with phase jumps confined to a more narrow saddle region; see Figure 8 below. In contrast, wavefields dominated by inline harmonics would instead appear more diamond shaped, as is the case in linear theory; see Figure 9 below.

In order to get an idea of how much the solution of a small-angle approximation would deviate from the predictions of the full theory, we have recomputed the solution for b and c for the parameters used to obtain the solution in Figure 2. The solution is obtained using the small angle values for γ and Θ and the parabolized values of $I = J = 3$, which represents the most extreme reduction of the theory in terms of directional resolution, barring reduction to one-dimension. Results are shown in Figure 5. The figure is similar to Figure 2 except that the plots of b and c seem to be stretched out along the θ axis; the waves behave as if the angle between the primary components is less than it actually is. This is due to the fact that the small angle estimate of the value of γ drops off less quickly than does the true value, and to the fact that the use of $I = J = 3$ causes the nonlinear interactions to behave more like they would at vanishingly small angle of incidence than would be expected. Note that tests in section 5 cover a corresponding range of θ 's up to about 45° ; deviations between the full solution and the parabolic form are significant in this range.

4.2 Unsteady evolution

The results for steady periodic waves indicate that nonlinear interactions can distort the underlying components of the wave train to the extent that components that would be expected to be only weakly tuned based on linear parameters are actually dominant parts of the wave. In this section, we consider instead the unsteady evolution of similar wave trains, in which second harmonics are allowed to grow from zero amplitude. We are interested in the competition between the growing second-harmonic amplitudes and the dependence of the evolution on the intersection angle between the primary components. The numerical experiments described here are similar in spirit to the studies of second-harmonic generation in one space dimension performed by Mei and Unluata (1972) and Boczar-Karakiewicz (1972), with the exception that the two-dimensionality of the problem introduces a set of competing second harmonics. Depending on the angle of incidence of each primary with respect to the x axis, one of the two possible second-harmonic components may become

dominant in the harmonic generation process. The dominance corresponds closely to which of the components b or c takes on the larger value in the steady solution; larger values of b indicate that the sum-wave interaction will become dominant, larger values of c indicate that the in-line components will be dominant, and values of b and c which are close in magnitude indicate that the two harmonics will evolve in a complex fashion with neither being dominant. An illustration of these effects is given in Figure 6, which shows the pattern of second harmonic evolution for the case of $\mu^2 = 0.36$, $\epsilon = 0.1$ over an x distance of 100 water depths. The pattern shifts from one where the sum-wave interaction dominates the wave field evolution at small angles, to one where the in-line components dominate and the sum wave is only of minor importance at large angles.

The complexity of the wave field evolution at intermediate angles is of interest, and sensitive laboratory experiments on this topic could provide a way of discriminating between the detailed accuracy of various future versions of schemes like the one developed here. The relevance of these results to natural events is in question, though. Recent computational tests using a one-dimensional model (Elgar et al, 1990) have shown that an evolving triad (or degenerate triad involving a primary component and its second harmonic) is unstable to broad-banded noise and would thus not be expected to be manifested in the natural wave field which has arrived after travelling some distance. This result does not invalidate the use of second-harmonic generation tests in the laboratory as a means of studying model accuracy.

Finally, use of the full model (15) with a large number N of components retained would allow for the generation of a more complex pattern of higher harmonics; the resulting wave fields are not qualitatively different from the ones shown here and still exhibit recurrence or quasi-recurrence.

5 Comparison with Data and a Parabolic Model Approximation

In order to verify the basic computational model provided by (15) and to test whether the present angular spectrum provides a more accurate representation of the wave field relative to earlier parabolic models (LYK; Yoon and Liu, 1989), we have compared model predictions to laboratory data obtained by Hammack et al (1990) for the case of glancing, or Mach, reflection of a cnoidal wave by a vertical wall. The experimental tests were conducted using the directional wave maker at the Coastal Engineering Research Center, Vicksburg, MS. A prior use of this facility to study the properties of intersecting cnoidal waves is described in Hammack et al (1989), referred to here as HSS.

5.1 Layout of Experimental Facility

For the tests considered here, the wave basin was operated with a water depth of 20cm in a constant depth region extending 12.55m in front of the wavemaker, after which a beach with 1:30 slope provided an efficient wave absorber giving little reflection. The basin floor was leveled to a tolerance of 0.01 ft in order to remove some of the spatial irregularity of the waves reported in HSS resulting from local refraction effects. For the Mach stem tests, two parallel false walls were installed perpendicular to the wavemaker axis in order to provide a closed channel. The channel walls were situated 13.26m apart, which fixes the width of the numerical domain to be considered.

Instrumentation and data acquisition are described in HSS, and readers are referred there for greater detail. In the present tests, an array of 18 wave gages were installed in the basin as shown in Figure 7. In this figure, the directional wavemaker occupies the y -axis, and the channel sidewalls lie along the x -axis and the line $y = -13.26m$. The positions of the gages are given in Table 1. The linear gage array 13 - 9 - 8 - 7 - 6 - 4 - 3 - 2 - 1 provides a transect perpendicular to the reflecting sidewall which allows a determination of the width and structure of the Mach stem and additional crests in the reflection pattern. This array is used to provide most of the information described below. An additional array 18 - 17 - 16 - 15 - 14 - 13 - 5 provides measurements of the evolution of the reflected stem wave along the wall. For each gage, data consists of a time series of 1250 points with a sampling rate of 25Hz.

5.2 Specification of the Incident Wave

The generation of oblique cnoidal waves using the directional wavemaker has been described in HSS. In the present laboratory tests, waves were initially specified as having a wavelength of 2m and a crest elevation 4cm above mean water level. The algorithms given by Goring and

Raichlen (1980) were used to generate a time series of paddle displacement corresponding to one-dimensional generation. Oblique waves were then generated by phase lagging adjacent paddles. The relation between paddle phase shift angle β and directed wave angle α is given by

$$\beta = \arcsin(\alpha L/360W) \quad (48)$$

where L is the wave length and $W = 45\text{cm}$ is the individual paddle width. Tests were conducted for six paddle phase lags, and are denoted $CRxx0204$, where xx denotes paddle phase lag. Note that (48) corrects a typographic error appearing in HSS. Table 1 gives a list of α and β values for the six tests.

Prior to running the Mach reflection experiments, the nominally 4cm high wave was generated in the normally incident direction (traveling parallel to sidewalls) in order to study its characteristics. It was found that the wave actually had a crest elevation close to 3.3cm above mean water level. This value was used to specify incident waves in the numerical computation, along with a wave period of 1.478s as specified by KdV cnoidal wave theory. We note that it is impossible to tell whether the value of 3.3cm was invariant under changes of angle of incidence in the laboratory experiment. Variation of this quantity would add an untraceable source of error in model-data comparison.

It has been shown (Kirby, 1990) that spectral models of the type described here (with lowest order non-dispersive results used to develop dispersive and nonlinear terms) have one-dimensional solutions that correspond exactly to solutions of the modified KdV-type equation

$$\eta_t + c\eta_x - \frac{3}{2h}\eta\eta_x - \frac{h^2}{6c^2}\eta_{ttt} = 0 \quad (49)$$

In order to account for this factor, input data for the computational models was specified as follows. First, KdV theory was used to determine a waveheight and wave period corresponding to the wave described above. Then, a Fourier series solution of the modified KdV equation (49) was performed using that waveheight and period to specify the solution. This solution led to a predicted wavelength of 1.9977m , which is only slightly less than the KdV prediction of 2m . (Recall, however, that the 2m value was for a crest elevation of 4cm rather than 3.3cm). This wavelength was then used in (48) along with the phase lag angle α in order to determine the directed angle β for each test. A table of resulting angles is given in Table 2.

The computed wave angle and the Fourier coefficients derived from the solution of (49) were used to compute the surface displacement for oblique cnoidal waves along the boundary $x = 0\text{m}$ corresponding to the wavemaker. For parabolic model calculations, information in the range $-13.26\text{m} \leq y \leq 0\text{m}$ was used to start the computation. The model was run with reflective sidewalls at $y = 0, -13.26\text{m}$. For the spectral model, a periodic interval

was constructed by using a mirror image about $y = 0m$; the computational domain thus corresponds to the region $-13.26m \leq y \leq 13.26m$. The computed waveform was then Fourier transformed over this interval and the resulting frequency-wavenumber spectrum was fed into the spectral model. (It is noted that the problem as stated could be handled directly by means of a cosine transform over the true model domain; this was not done because of the reprogramming of the basic model that would have been required.)

For the examples shown here, the parabolic model was run with a grid spacing $\Delta x = \Delta y = 0.0625m$, and $N = 9$ frequency components were used. Tests were performed for two cases for both half the grid spacing and twice the number of harmonics to insure that convergence was adequate for the parameters finally used. In the spectral model, we used $N = 9$ and $M = 64$. The large value of M insures that all freely propagating modes of the solution are retained for the highest harmonic considered. The forward grid space step was also $\Delta x = 0.0625m$. Again, these parameters were found to give sufficient convergence of solutions when compared to runs with smaller grid steps and more retained frequency components.

5.3 Results

Results of model calculations are presented here in two forms: gray level contour plots of instantaneous surface over the model basin, and time series computed from model output and compared to experimental data. The gray level plots are actually of the quantity $-\partial\eta/\partial x$, and the pictures thus mimic the visual image that would be obtained in an overhead photograph resulting from lighting at a low angle from the direction of the wavemaker. (This is similar to the photographic arrangement in HSS). In all cases, the gray level plots from parabolic model computations are similar to those from spectral model computations, and only spectral model results are shown. Figure 8 presents results for the test CR150204, which clearly shows the evolution of a wide Mach stem wave along the reflecting boundary. In contrast, Figure 9 shows the other extreme example of test CR580204, where the angle of incidence is about 45° and the reflection pattern is regular (i.e., nearly linear superposition.)

In order to compare time series from experiment and model calculations, the following procedure is used. First, after allowing some time for nearly periodic motion to be established in the experiment, a reference time t_0 is established at the position of a wave crest at gage 13 ($x = 11m, y = -0.07m$). This start time is used for all other gages as well, in order to maintain synchronization. Then, a start time is also established for the model-predicted time series by identifying a crest at model gage 13. Synchronization between model and data time series is thus based on correlating the series at a gage location, rather than (more correctly) correlating at the wavemaker. This step is necessary since the wavemaker control

is not available and since absolute time in the model-constructed time series is arbitrary.

After determining the synchronous start times for model and data at gage 13, time series were plotted for the transect along the wall (gages 18-17-16-15-14-13-5) and perpendicular to the wall (gages 13-9-8-7-6-4-3-2-1). Aside from the presence of experimental errors, a correct model result would be indicated by complete agreement between model and data time series at each gage. As examples, two periods of time series for the perpendicular transect are shown in Figure 10 for the spectral model predictions for CR150204. The plot shows a stem developed near the wall in the area spanned by gages 13-9-8-7, beyond which there is a clear phase lead at each subsequent gage, indicating the approach of the incident wave at a small angle of incidence. In this plot, model predictions are indicated by solid lines and experimental data by dashed lines. At the opposite extreme, Figure 11 shows spectral model predictions and data for the case CR580204. This figure indicates the structure of a short crested wave field, with one complete diamond over the range of gages 13-9-8-7-6-4-3, whereas the signal in gages 3-2-1 indicating a strong progressive phase lag, corresponding to a wave travelling *away from* the wall at close to 45°. The structure of the plots in Figures 10 and 11 may be further clarified by comparing them to the contour plots in Figures 8 and 9, respectively.

In order to quantify the comparison between model predictions and measurements, a standard correlation coefficient ρ was calculated for each time series on the perpendicular transect. For $i=1, \dots, I$ corresponding to the discrete time series over two wave periods and $j = 1, \dots, 9$ corresponding to the 9 gages, we first define a correlation for each gage by

$$\rho_j = \frac{C_{12j}}{\sigma_{1j}\sigma_{2j}} \quad (50)$$

where subscripts 1 and 2 refer to data and model, respectively, and where

$$C_{12j} = \frac{1}{I} \sum_{i=1}^I \eta_{1j}(i) \eta_{2j}(i) \quad (51)$$

$$\sigma_{lj} = \sqrt{\frac{1}{I} \sum_{i=1}^I \eta_{lj}(i) \eta_{lj}(i)}; \quad l = 1, 2 \quad (52)$$

are measures of covariance of model and data signals and of the individual standard deviations. Table 3 gives values of ρ_j for the nine gages for both spectral and parabolic models, as well as a composite average $\bar{\rho}$ given by

$$\bar{\rho} = \frac{1}{9} \sum_{j=1}^9 \rho_j \quad (53)$$

which becomes a measure of accuracy at each angle of incidence. A plot of $\bar{\rho}$ versus incident angle β is given in Figure 12. The plot indicates that the correlation for the spectral model

is high and does not fall off with increasing angle until the last test, CR58. This would be expected, since the model does not have any restriction on angle of incidence. The loss of correlation in CR58 relative to the other tests is due to the strong apparent mismatch in phase on the last three gages 3-2-1 in Figure 11, which biases the overall average low (see results for this test in Table 3). In contrast, the correlation between parabolic model and data is weaker and falls off progressively with increasing angle except for an anomalous agreement on the last test, CR58. We remark here that the standard correlation coefficient ρ , which penalizes mismatches in wave phase heavily, can also give high values of correlation when information is in phase, even though there is strong disagreement between details of the compared time series. To illustrate this effect, the parabolic model time series are compared to data in Figure 13 for CR58. The mismatch in crest structures is striking, but the waves are phased relatively correctly and so the correlation coefficient becomes high.

In order to provide an independent check on these results, an rms error measure was constructed for the comparison. This measure e is given by

$$e_j = \sqrt{\frac{\frac{1}{I} \sum_{i=1}^I (\eta_{2,j}^2(i) - \eta_{1,j}^2(i))}{\frac{1}{I} \sum_{i=1}^I (\eta_{1,j}^2(i))}} \quad (54)$$

for each gage, where the normalization of the mean square error is with respect to the true (data) standard deviation. A composite value \bar{e} for each angle or test is constructed from the ratio of the rms error for all points divided by the total standard deviation for all points. Table 4 gives the computed error estimates for all tests, and Figure 14 shows the composite error as a function of incidence angle for the two models. In this case, the trend towards increasing error with increasing angle is clear in the parabolic model results. The spectral model also shows an increasing trend in this case, which would not necessarily be expected.

One possible reason for an increase in error in the spectral model as wave angle becomes large rests in the fact that the reflected wave crests at the wall and in the short-crested wave pattern away from the wall result from the interaction between waves that are colliding head on to the same extent as they are interacting colinearly. Tests and analysis of head on collision and vertical wall reflection of solitary waves have indicated that the leading order theory (as in the Boussinesq model employed here) is not capable of predicting the height of the runup or maximum elevation, or the phase lag associated with the opposite-going interaction. See Su and Mirie (1980) for an example of this type of analysis. Effects of this nature may be present in the experiments being considered here. Figure 15 displays the comparison of the time series on the transect 18-17-16-15-14-13-5 along the wall for test CR580204, using spectral model results. Synchronization is again with respect to gage 13. It is clear that the height of the wave along the wall is underpredicted by the model, as may be expected for the case of low-order Boussinesq theory with waves interacting at

large angles. This underestimation of the crest height could in turn have a detrimental effect on the prediction of phase speed; the picture indicates that the model waves are relatively slower than the experimental waves. The discrepancies between model and data on the transect along the wall are even more drastic for the parabolic model, as would be expected.

In the comparisons made above, no attempt was made to find a relative alignment of model and data results that would minimize error in each case, or to define an error measure that is "best" in any sense. The results of the comparison generally indicate that the spectral model is better capable of modelling the mach reflection than is the parabolic model.

6 Discussion

We have described the development of a solution technique for the Boussinesq model of long waves, based on a discrete representation of the angular spectrum for waves incident towards shore from the ocean. The model is similar in intent to the parabolic model developed earlier by LYK, with the exception that the present model does not impose a restriction on the range of directions that can be accurately modelled. This advantage is counterbalanced (at this stage of development) by the need to impose periodic boundary conditions on the modelled problem. This restriction must be alleviated before the various representations of angular spectrum models (present model; Dalrymple and Kirby, 1988; Dalrymple et al, 1989) become generally applicable as coastal wave models.

A simple application of the angular spectrum model in section 4 showed that nonlinear interactions between modes travelling in different directions can interact strongly to produce a significant mode travelling at an intermediate direction. In the example here, it was shown that the amplitude of second harmonic waves resulting from the sum interaction of two intersecting primary waves may actually exceed the amplitude of the in-line second harmonics resulting from self-interaction in each primary wave. This result would seem to be counter-intuitive, since the interaction between modes travelling at different directions would seem to be weaker than the interaction between modes with similar frequencies travelling in the same direction. In the overall interplay of the nonlinear interactions, this simple picture does not win out, either for the case of steady solutions or solutions evolving by means of harmonic generation. A recent paper (Freilich et al, 1990a) has shown evidence that distinct peaks resulting from higher-harmonic generation by sum interactions of waves travelling in different directions are observable in measured field data. Initial indications are that the parabolic modelling scheme (as in LYK) is capable of modelling this interaction and reproducing the measured directional spectra after shoaling (Freilich et al, 1990b). A comparison of the present and the parabolic modelling schemes and their application to field data are underway and will be reported separately.

Finally, comparison of the present model, a parabolic model and laboratory data indicates that differences do occur between predictions of a small-angle approximation and the fully directional expansion employed here, and that the deviation is apparent even at small angles of incidence. This result indicates that the further development of the angular spectrum model is worth pursuing as a means of providing accurate prediction of coastal wave fields. The first extension of the present model to include weak longshore topographic variation and on-offshore reflection is presently underway and will be described shortly.

Appendix A: Nonlinear terms

The nonlinear term $[n.l.t.]_n$ appearing in (6) is given by

$$\begin{aligned}
 [n.l.t.]_n = & -\frac{g}{4k^2} \left\{ \sum_{l=1}^{n-1} \frac{1}{l(n-l)} \nabla \cdot [\nabla \eta_l \cdot \nabla (\nabla \eta_{n-l}) + \nabla \eta_{n-l} \cdot \nabla (\nabla \eta_l)] \right. \\
 & - 2 \sum_{l=1}^{N-n} \frac{1}{l(n+l)} \nabla \cdot [\nabla \eta_l^* \cdot \nabla (\nabla \eta_{n+l}) + \nabla \eta_{n+l} \cdot \nabla (\nabla \eta_l^*)] \Big\} \\
 & - \frac{n^2 g k^2}{4} \left\{ \sum_{l=1}^{n-1} \eta_l \eta_{n-l} + 2 \sum_{l=1}^{N-n} \eta_l^* \eta_{n+l} \right\} \\
 & + \frac{g n^2}{4} \left\{ \sum_{l=1}^{n-1} \frac{\nabla \eta_l \cdot \nabla \eta_{n-l}}{l(n-l)} - 2 \sum_{l=1}^{N-n} \frac{\nabla \eta_l^* \cdot \nabla \eta_{n+l}}{l(n+l)} \right\} \quad (A1)
 \end{aligned}$$

The term $[n.l.t.]_n^m$ appearing in (10) is given by

$$\begin{aligned}
 [n.l.t.]_n^m = & -\frac{g}{4k^2} \left\{ \sum_{l=1}^{n-1} \frac{1}{l(n-l)} \left[\sum_p ((\eta_{l,x}^p \eta_{n-l,x}^{m-p})_{xx} - \lambda_0^2 m^2 \eta_{l,x}^p \eta_{n-l,x}^{m-p} - \lambda_0^2 p(m-p) (\eta_l^p \eta_{n-l}^{m-p})_{xx} \right. \right. \\
 & \left. \left. + \lambda_0^4 p(m-p) m^2 \eta_l^p \eta_{n-l}^{m-p} \right] \right. \\
 & - 2 \sum_{l=1}^{N-n} \frac{1}{l(n+l)} \left[\sum_p ((\eta_{l,x}^{p*} \eta_{n+l,x}^{m+p})_{xx} - \lambda_0^2 m^2 \eta_{l,x}^{p*} \eta_{n+l,x}^{m+p} + \lambda_0^2 p(m+p) (\eta_l^{p*} \eta_{n+l}^{m+p})_{xx} \right. \\
 & \left. \left. - \lambda_0^4 p(m+p) m^2 \eta_l^{p*} \eta_{n+l}^{m+p} \right) \right] \Big\} \\
 & - \frac{n^2 g k^2}{4} \left\{ \sum_{l=1}^{n-1} \left[\sum_p (\eta_l^p \eta_{n-l}^{m-p}) \right] + 2 \sum_{l=1}^{N-n} \left[\sum_p (\eta_l^{p*} \eta_{n+l}^{m+p}) \right] \right\} \\
 & + \frac{g n^2}{4} \left\{ \sum_{l=1}^{n-1} \frac{1}{l(n-l)} \left[\sum_p (\eta_{l,x}^p \eta_{n-l,x}^{m-p} - p(m-p) \lambda_0^2 \eta_l^p \eta_{n-l}^{m-p}) \right] \right. \\
 & \left. - 2 \sum_{l=1}^{N-n} \frac{1}{l(n+l)} \left[\sum_p (\eta_{l,x}^{p*} \eta_{n+l,x}^{m+p} + p(m+p) \lambda_0^2 \eta_l^{p*} \eta_{n+l}^{m+p}) \right] \right\} \quad (A2)
 \end{aligned}$$

Acknowledgements

The author would like to thank the Office of Naval Research for support for this study through grants N00014-89-J-1717 and N00014-90-J-1678, and Joe Hammack, Norm Scheffner and Harvey Segur for their very generous donation of experimental data prior to their own analysis or publication of it. James Kaihatu performed the parabolic model computations and the parabolic model - data comparisons.

References

- Boczar-Karakiewicz, B., 1972, "Transformation of wave profile in shallow water - a Fourier analysis", *Arch. Hydrotechniki*, 19, 197-210.
- Dalrymple, R.A. and Kirby, J.T., 1988, "Models for very wide-angle water waves and wave diffraction", *J. Fluid Mech.*, 192, 33-50.
- Dalrymple, R.A., Suh, K. D., Kirby, J.T. and Chae, J. W., 1989, "Models for very wide-angle water waves and wave diffraction. Part 2. Irregular bathymetry", *J. Fluid Mech.*, 201, 299-322.
- Elgar, S. and Guza, R.T., 1985, "Shoaling gravity waves: comparisons between field observations, linear theory, and a nonlinear model", *J. Fluid Mech.*, 158, 47-70.
- Elgar, S. and Guza, R.T., 1986, "Nonlinear model predictions of bispectra of shoaling surface gravity waves", *J. Fluid Mech.*, 167, 1-18.
- Elgar, S., Freilich, M. H. and Guza, R. T., 1990, "Recurrence in truncated Boussinesq models for nonlinear wave in shallow water", *J. Geophys. Res.*, in press.
- Freilich, M.H. and Guza, R.T., 1984, "Nonlinear effects on shoaling surface gravity waves", *Phil. Trans. Roy. Soc. Lond.*, A 31, 1-41.
- Freilich, M.H., Guza, R.T. and Elgar, S., 1990a, "Observations of nonlinear effects in directional spectra of shoaling gravity waves", *J. Geophys. Res.*, in press.
- Freilich, M.H., Guza, R.T. and Elgar, S., 1990b, personal communication.
- Funakoshi, M., 1981, "On the time evolution of a solitary wave reflected by an oblique wall", *Rep. Res. Inst. Applied Mech.*, 29, 79-93.
- Goring, D.G. and Raichlen, F., 1980, "The generation of long waves in the laboratory", *Proc. 17th Intl. Conf. Coastal Engrng.*, Sydney.
- Hammack, J., Scheffner, N. and Segur, H., 1989, "Two-dimensional periodic waves in shallow water", *J. Fluid Mech.* 209, 567-589. (referred to in the text as HSS).
- Hammack, J., Scheffner, N. and Segur, H., 1990, personal communication.
- Kadomtsev, B.B. and Petviashvili, V.I., 1970, "On the stability of solitary waves in weakly dispersing media", *Sov. Phys. Dokl.*, 15, 539-541.

- Kirby, J. T., 1990, "Intercomparison of truncated series solutions for shallow water waves", submitted to *J. Waterway, Port, Coastal and Ocean Engrng.*
- Kirby, J.T. and Vengayil, P., 1988, "Non-resonant and resonant reflection of long waves by topography", *J. Geophys. Res.*, 93, 10782-10796.
- Kirby, J.T., Philip, R. and Vengayil, P., 1988, "One- dimensional and weakly two-dimensional waves in varying channels: numerical examples", in K. Horikawa and H. Maruo (eds), *Nonlinear Water Waves*, 357-364, Springer.
- Liu, P.L-F., Yoon, S.B. and Kirby, J.T., 1985, "Nonlinear refraction-diffraction of waves in shallow water", *J. Fluid Mech.*, 153, 185-201. (referred to in the text as LYK)
- Mei, C. C. and Unluata, U., 1972, "Harmonic generation in shallow water waves", in *Waves on Beaches*, (ed) R. E. Meyer, Academic Press, N. Y., 181-202.
- Melville, W.K., 1980, "On the Mach reflection of a solitary wave", *J. Fluid Mech.*, 98, 285-297.
- Miles, J.W., 1977, "Resonantly interacting solitary waves" *J. Fluid Mech.*, 79, 171-179.
- Peregrine, D.H., 1967, "Long waves on a beach", *J. Fluid Mech.*, 27, 815-827.
- Rogers, S. R. and Mei, C. C., 1978, "Nonlinear resonant excitation of a long and narrow bay", *J. Fluid Mech.*, 88, 161-180.
- Rygg, O. B., 1988, "Nonlinear refraction-diffraction of surface waves in intermediate and shallow water", *Coastal Engineering* 12, 191-211.
- Segur, H. and Finkel, A., 1985, " An analytical model of periodic waves in shallow water", *Stud. Appl. Math.*, 73, 183-220.
- Su, C. H. and Mirie, R. M., 1980, "On head-on collisions between two solitary waves", *J. Fluid Mech.*, 98, 509-525.
- Wu, D.-M. and Wu, T. Y., 1983, "Three-dimensional nonlinear long waves due to moving surface pressure", *Proc. 14th Symp. Naval Hydro.*, 103-125, Ann Arbor, Michigan.
- Yoon, S. B. and Liu, P. L.-F., 1989, "Stem waves along a breakwater", *J. Waterway, Port, Coast. and Ocean Engrng.*, 115, 635-648.

gage	$x(m)$	$y(m)$	gage	$x(m)$	$y(m)$	gage	$x(m)$	$y(m)$
1	11	-5	7	11	-1.5	13	11	-0.07
2	11	-4	8	11	-1	14	10	-0.07
3	11	-3	9	11	-0.5	15	8	-0.07
4	11	-2.5	10	8	-1	16	6	-0.07
5	12	-0.07	11	6	-1	17	4	-0.07
6	11	-2	12	10	-1	18	2	-0.07

Table 1: Wave gage positions in Mach reflection experiments

test	CR15	CR22	CR30	CR38	CR48	CR58
α	14.5	22.0	30.0	38.5	47.5	57.6
β	10.13	15.48	21.34	27.84	35.18	44.32

Table 2: Paddle phase angles and directed wave angles; Mach reflection experiments

spectral model										
gage	13	9	8	7	6	4	3	2	1	average
CR15	.996	.994	.997	.997	.987	.959	.926	.944	.968	.974
CR22	.974	.958	.963	.954	.951	.898	.943	.990	.860	.943
CR30	.984	.975	.989	.978	.802	.972	.949	.984	.981	.958
CR38	.986	.854	.827	.841	.985	.966	.897	.943	.994	.921
CR48	.993	.996	.950	.986	.982	.877	.783	.989	.993	.950
CR58	.986	.961	.886	.957	.842	.756	.804	.007	.791	.784
parabolic model										
gage	13	9	8	7	6	4	3	2	1	average
CR15	.994	.992	.997	.996	.959	.854	.760	.873	.924	.928
CR22	.984	.950	.923	.893	.807	.524	.742	.931	.523	.809
CR30	.978	.986	.971	.961	.033	.992	.993	.859	.945	.856
CR38	.999	.972	.892	-.644	.952	.839	.871	.703	.901	.721
CR48	.889	.914	-.516	.894	.929	.873	-.658	.938	.870	.570
CR58	.966	.852	.814	.852	.729	.790	.903	.944	.866	.858

Table 3: Correlation coefficients ρ for spectral and parabolic model runs

spectral model										
gage	13	9	8	7	6	4	3	2	1	average
CR15	.089	.109	.078	.076	.177	.296	.386	.349	.285	.193
CR22	.228	.292	.281	.305	.326	.496	.346	.148	.526	.296
CR30	.208	.234	.168	.214	1.250	.306	.317	.124	.196	.250
CR38	.276	.535	.578	1.060	.206	.275	.442	.520	.190	.383
CR48	.128	.137	.636	.206	.216	.524	.953	.162	.124	.273
CR58	.194	.277	.479	.293	.540	.717	.631	1.280	.612	.540
parabolic model										
gage	13	9	8	7	6	4	3	2	1	average
CR15	.113	.132	.093	.103	.327	.600	.713	.503	.422	.319
CR22	.191	.326	.407	.556	.916	1.240	.678	.370	1.020	.509
CR30	.242	.225	.418	.597	1.975	.386	.231	.690	.333	.365
CR38	.211	.324	.706	1.936	.430	.550	.612	.713	.489	.494
CR48	.513	.743	1.911	.473	.398	.799	1.425	.476	.598	.599
CR58	.261	.534	1.099	.969	1.611	.630	.672	.697	.515	.689

Table 4: RMS error coefficients ϵ for spectral and parabolic model runs

List of Figures

1	Interaction coefficients $I(\theta)$, $J(\theta)$ and phase argument $\Theta(\theta)$ for symmetric interaction described by (27-29).	28
2	Amplitudes b and c of second harmonics for case of symmetric, short-crested waves. Solution of full model for $\mu^2 = 0.36$ and $0.05 \leq \epsilon \leq 0.5$	28
3	Linear estimates of triad detuning for various intersection angles. Mismatch is in x component of wavenumbers, assuming perfect match in y components.	28
4	Wavefield for the case $\mu^2 = .36$, $\epsilon = 0.1$, $\gamma = 0.88$ (Corresponds closely to case CR38 in section 5).	29
5	Amplitudes b and c of second harmonics for case of symmetric, short-crested waves. Solution of small-angle model with $I = J = 3$, for $\mu^2 = 0.36$	29
6	Evolution of second harmonics resulting from the oblique interaction of two sinusoidal monochromatic waves. — , primary amplitude; - - - - , amplitude of second harmonic resulting from sum wave interaction; — - — , amplitude of second harmonics resulting from self-interaction in each primary component. All amplitudes normalized by initial value of primary wave amplitude. $\mu^2 = 0.36$, $\epsilon = 0.1$. (a) $\theta = 10^\circ$, (b) $\theta = 10^\circ$, (c) $\theta = 10^\circ$	29
7	Basin configuration, Mach reflection experiments	29
8	Predicted wave field, test CR150204. Spectral model	29
9	Predicted wave field, test CR580204. Spectral model	29
10	Measured and predicted time series for test CR150204, perpendicular transect. — , model; - - - , data. Spectral model	29
11	Measured and predicted time series for test CR580204, perpendicular transect. — , model; - - - , data. Spectral model	29
12	Variation of overall correlation coefficient $\bar{\rho}$ with angle of incidence β . — , spectral model; - - - , parabolic model.	30
13	Measured and predicted time series for test CR580204, perpendicular transect. — , model; - - - , data. Parabolic model	30
14	Variation of overall normalized error $\bar{\epsilon}$ with angle of incidence β . — , spectral model; - - - , parabolic model.	30
15	Measured and predicted time series for test CR580204, transect along wall. — , model; - - - , data. Spectral model	30

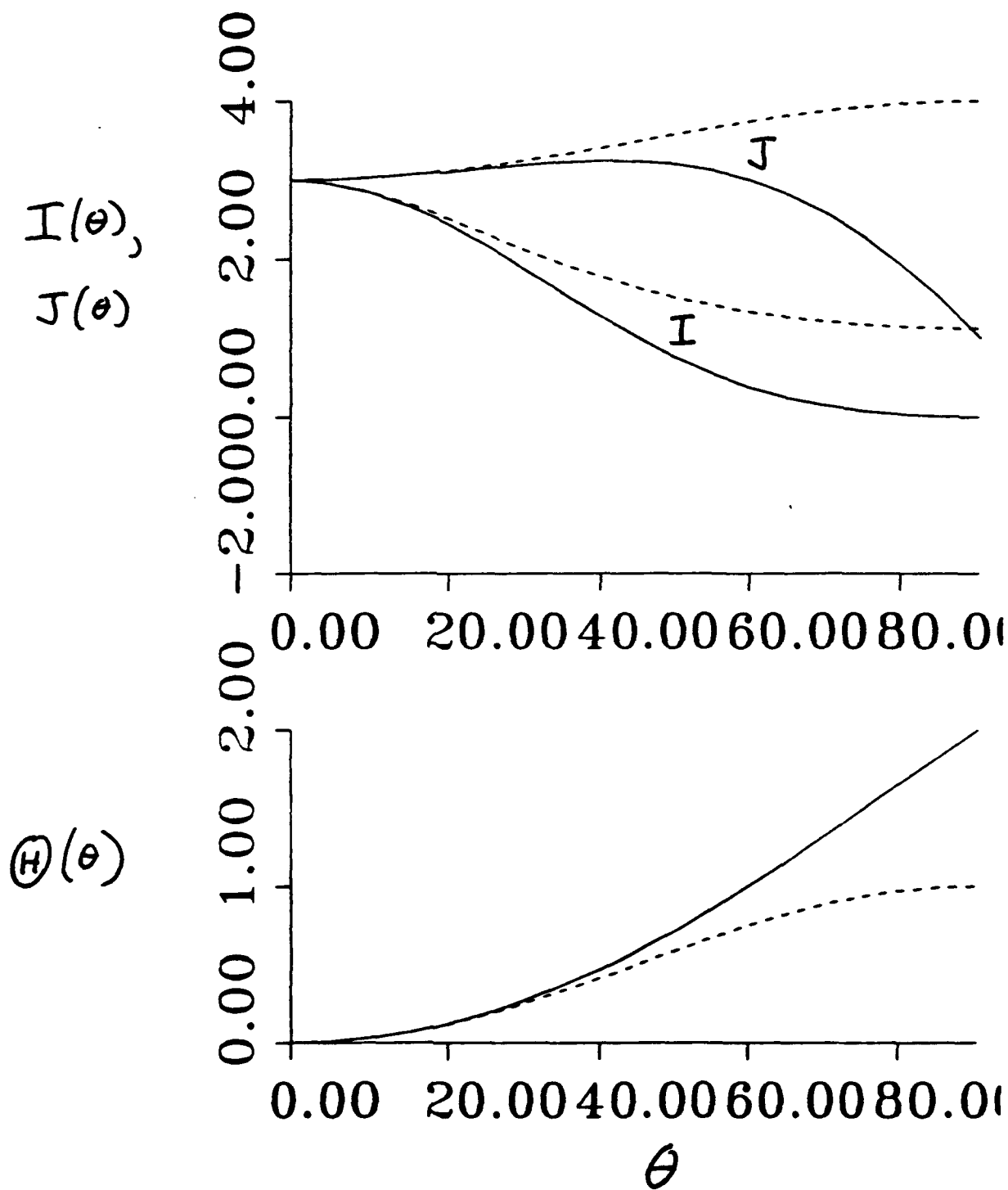


Figure 1

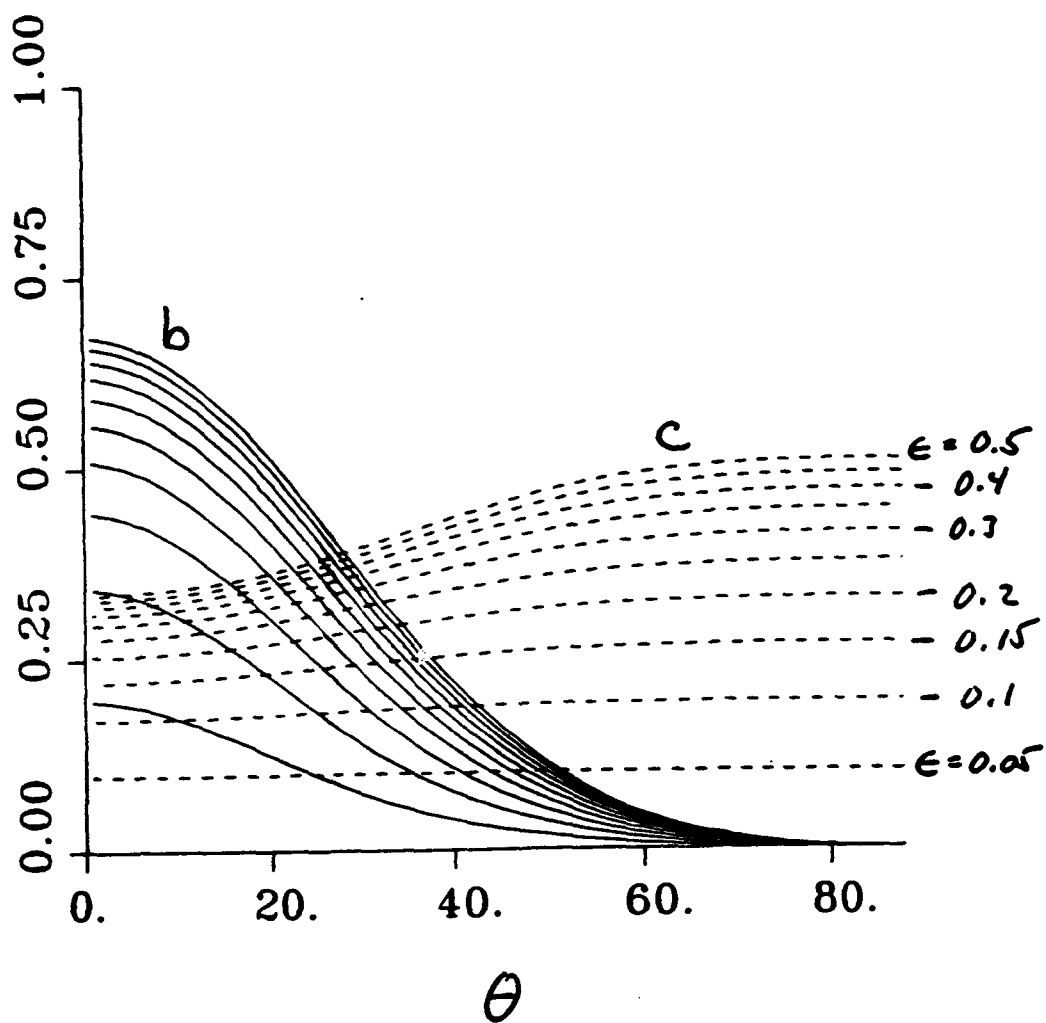
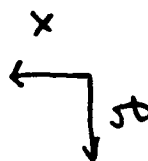
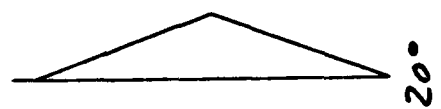
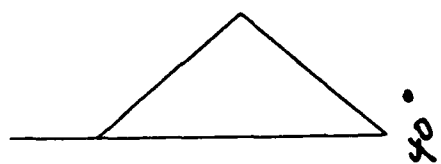
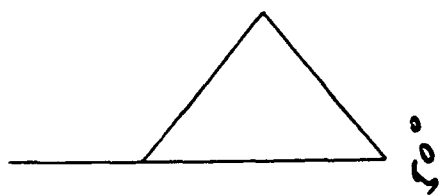


Figure 2

Figure 3



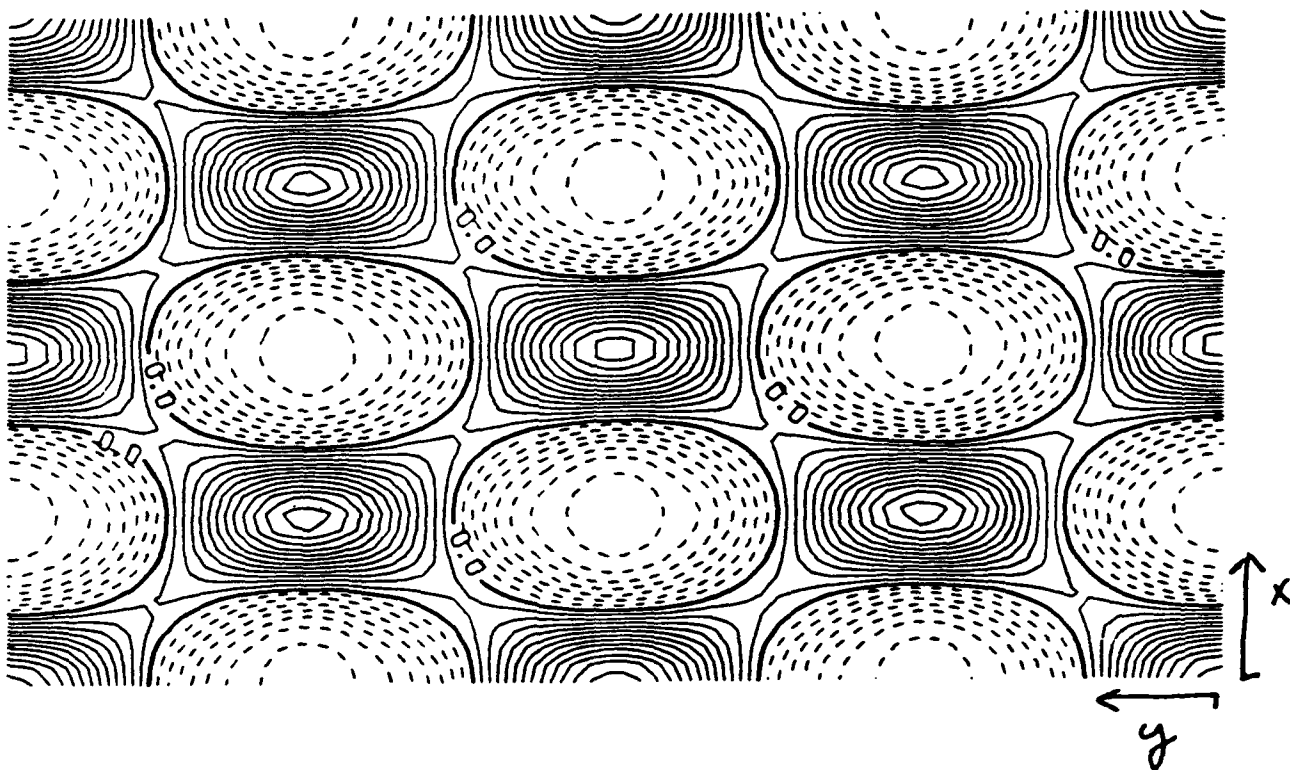


Figure 4

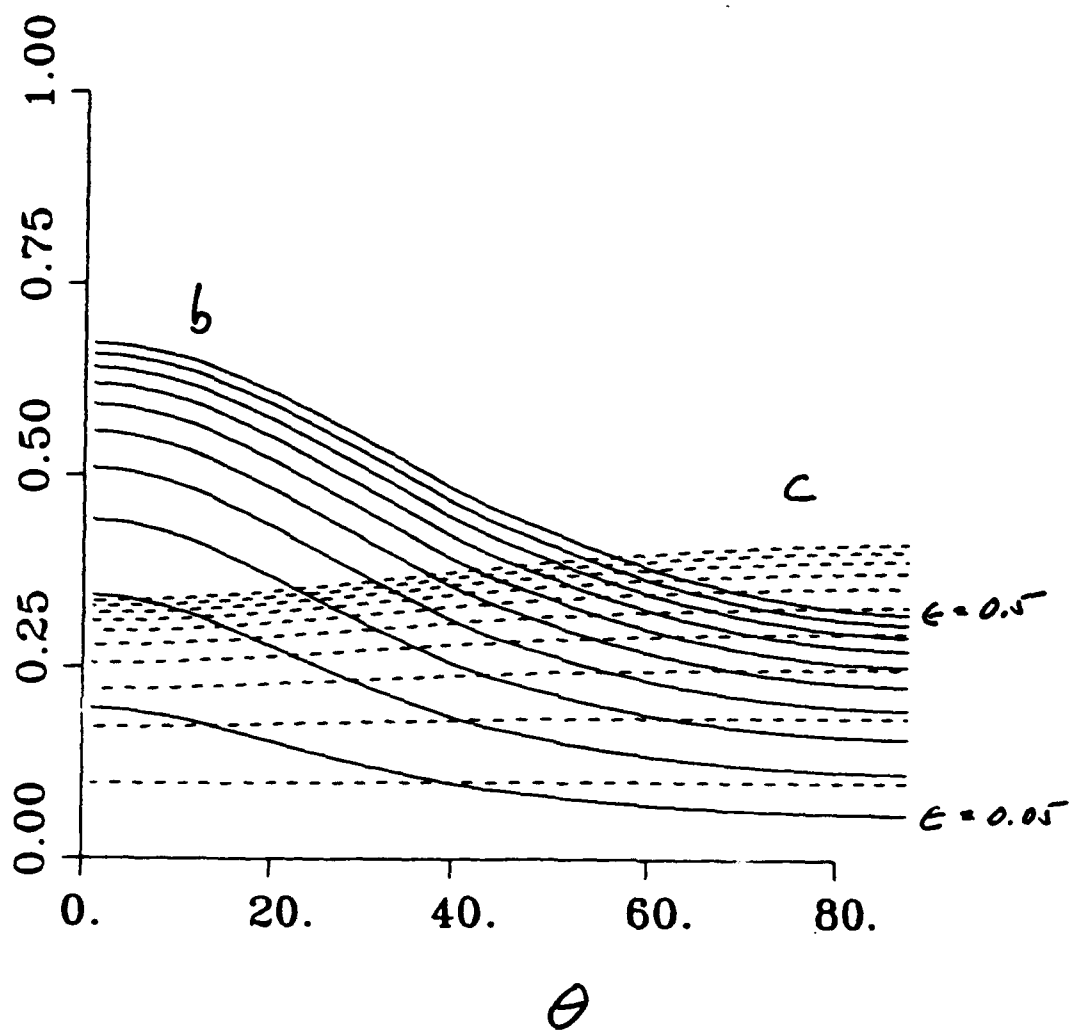


Figure 5

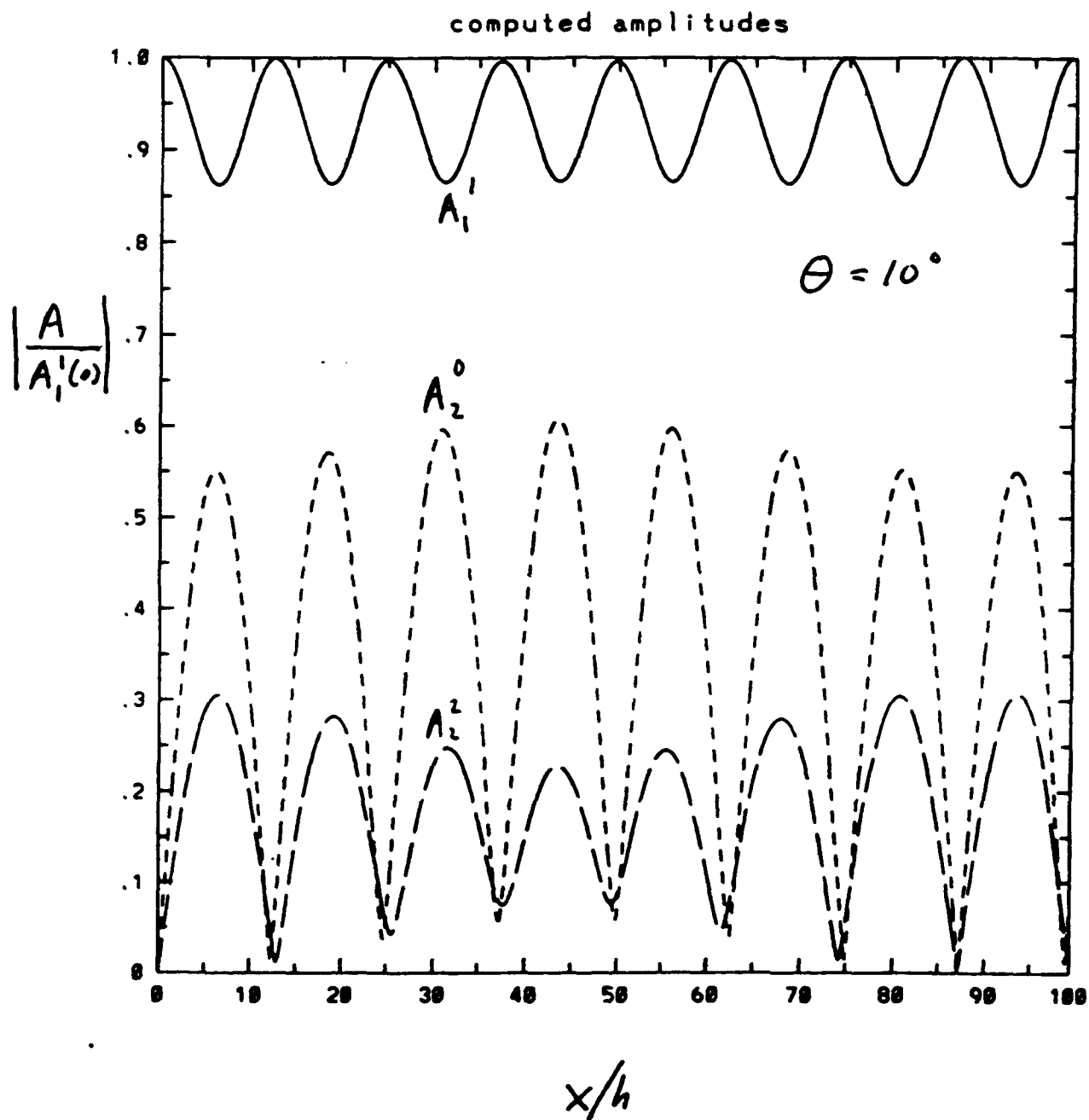


Figure 6a

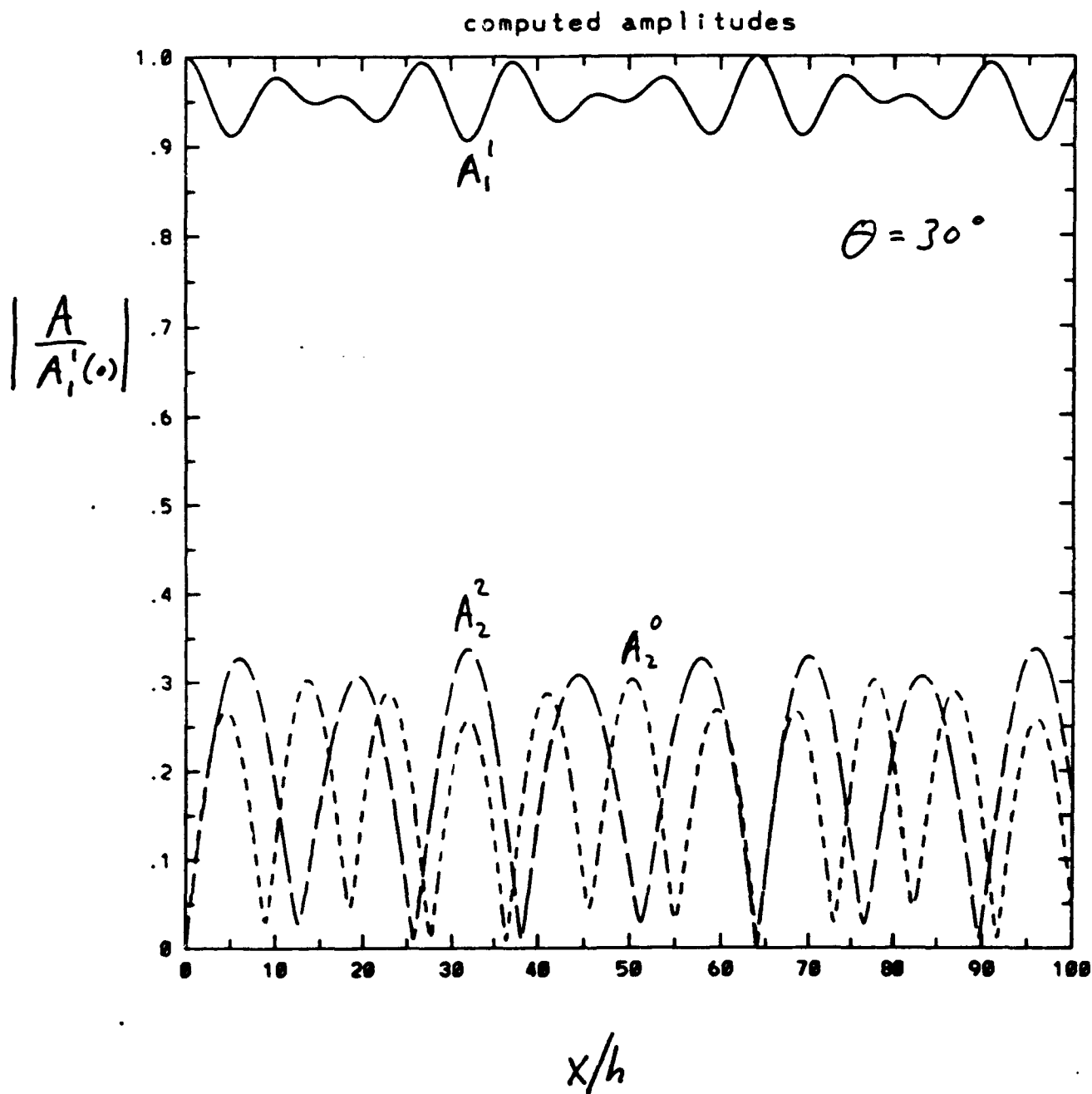


Figure 6b

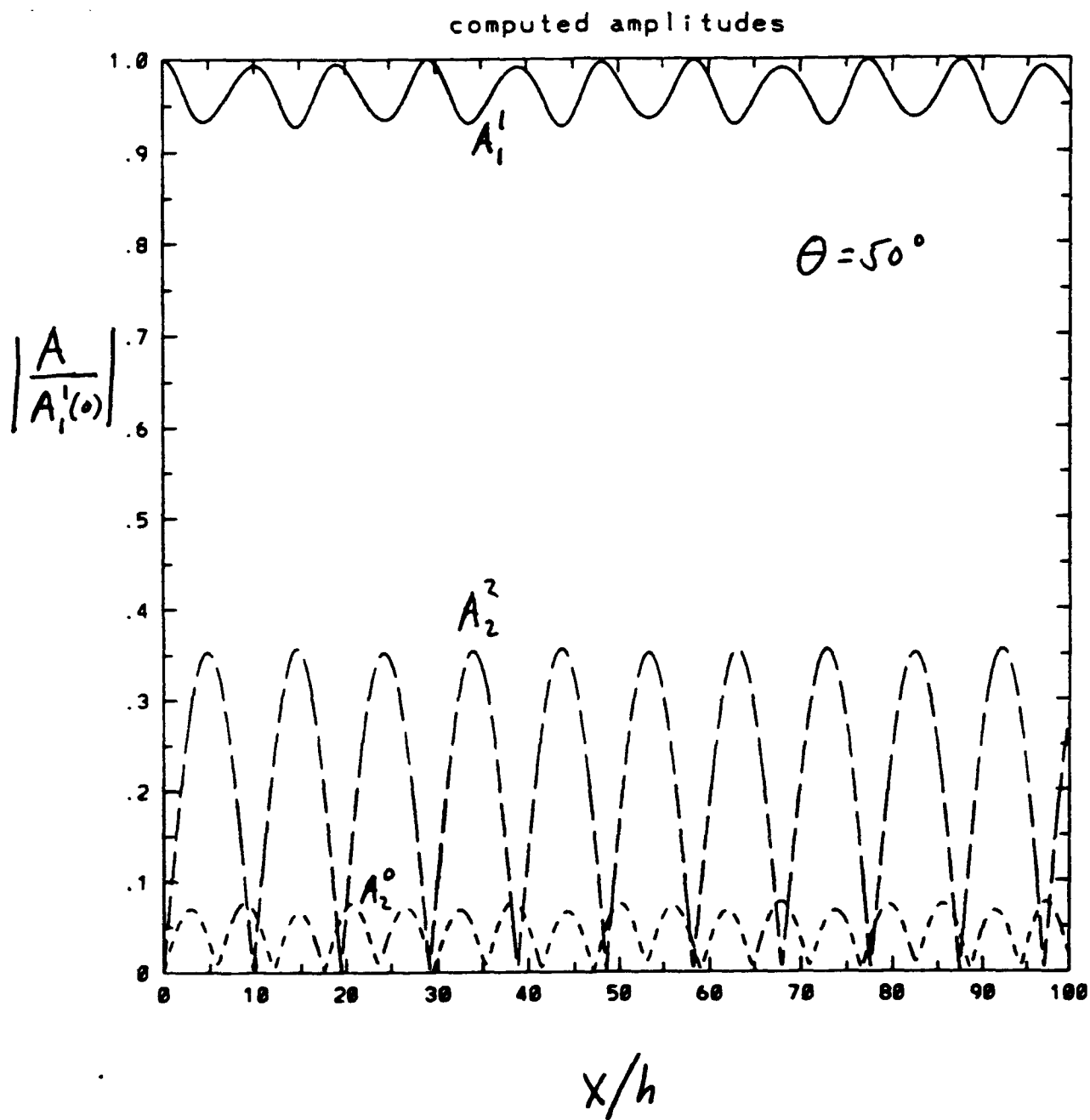


Figure 6c

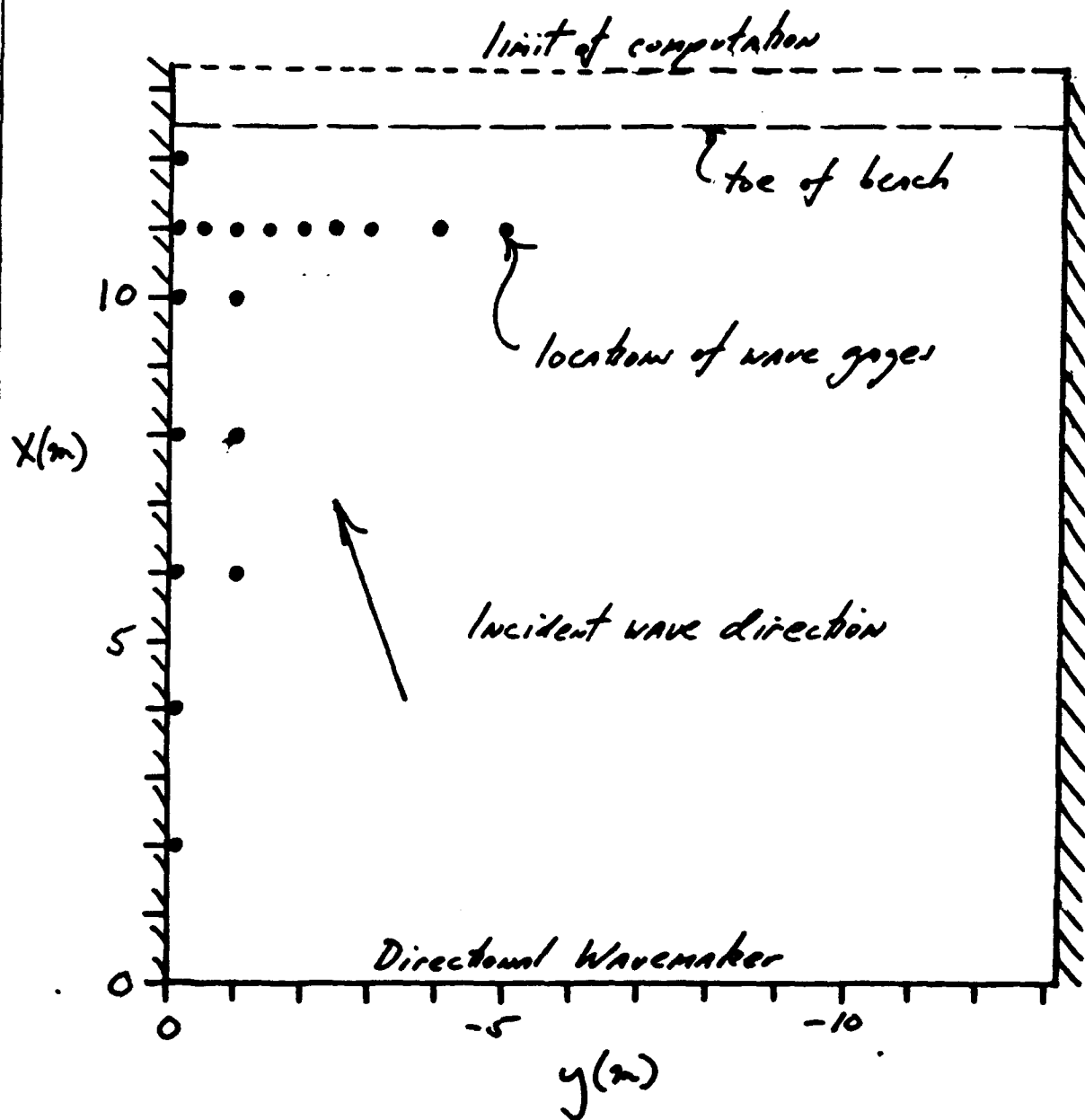


Figure 7

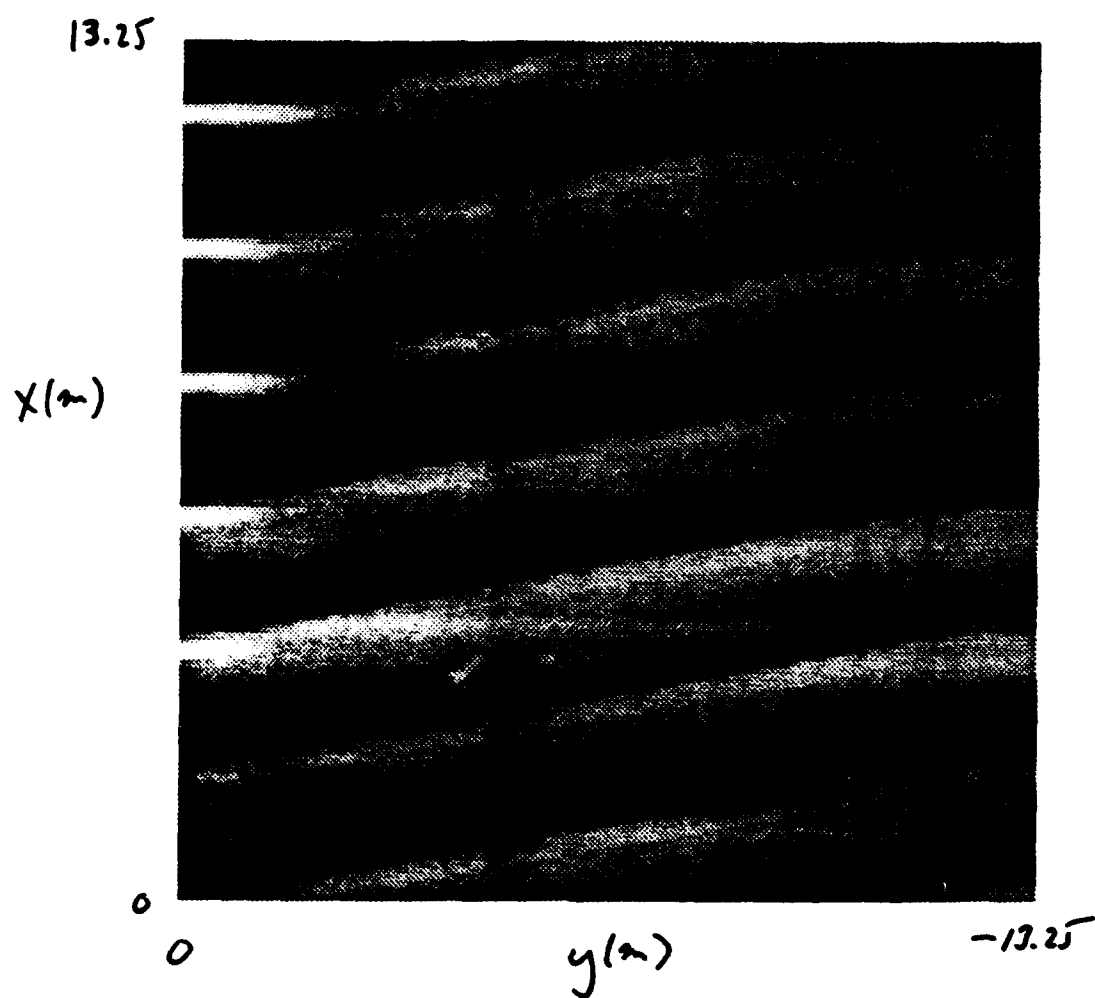


Figure 8

13.25

$x(z)$

0

0

$y(z)$

-13.25

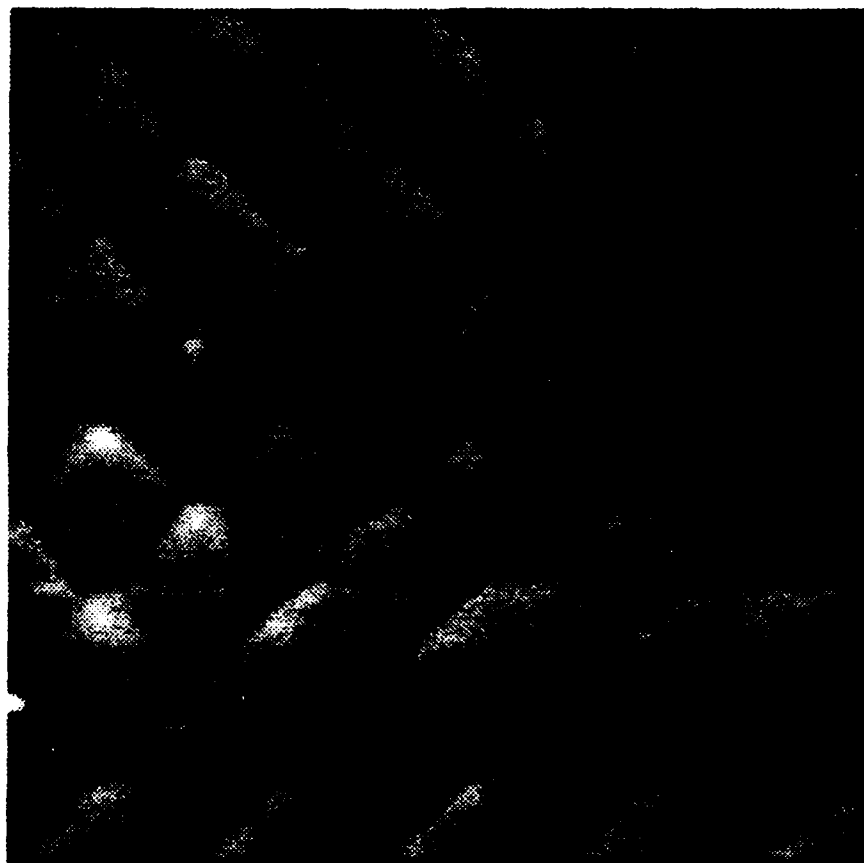


Figure 9

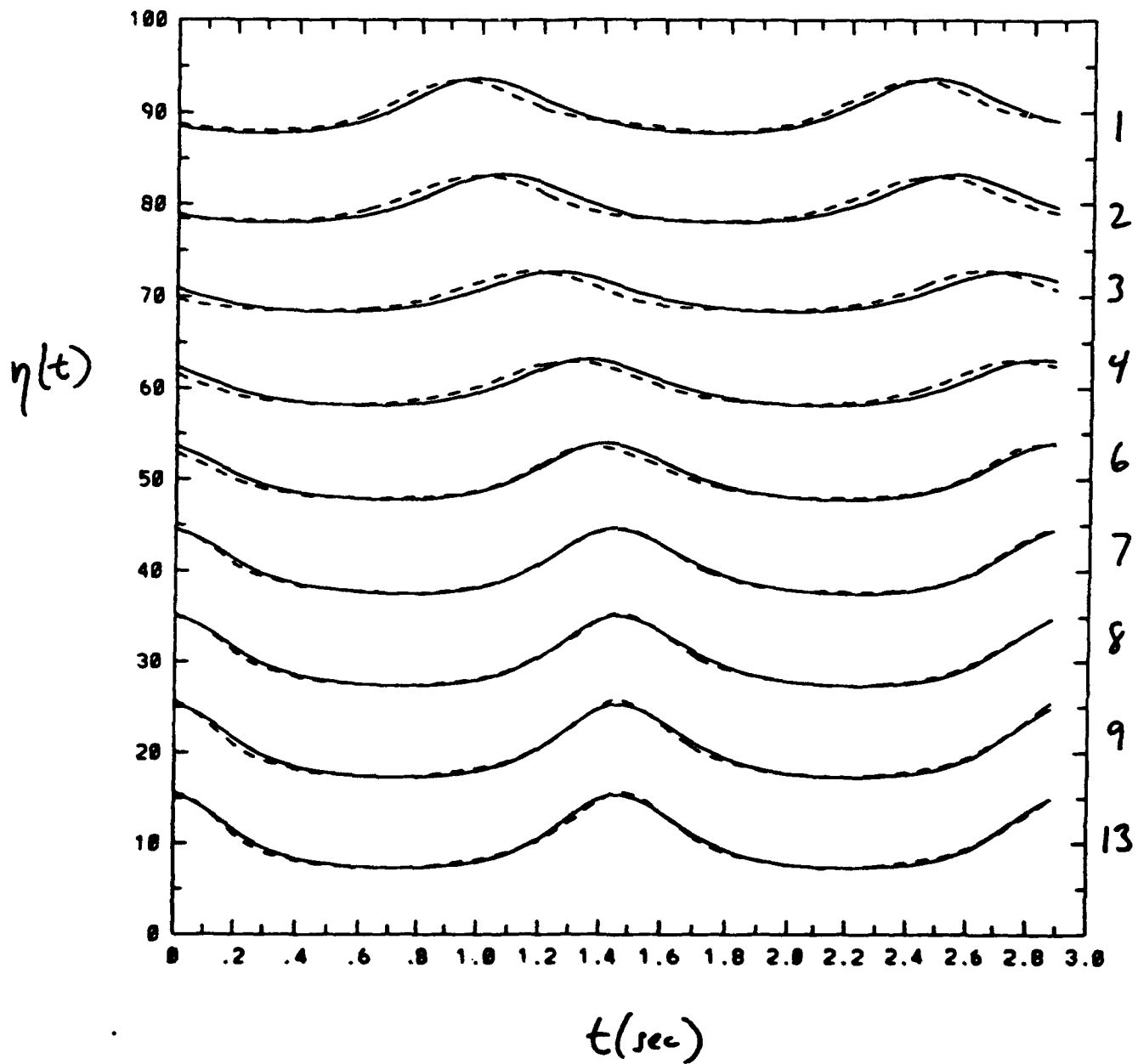


Figure 10

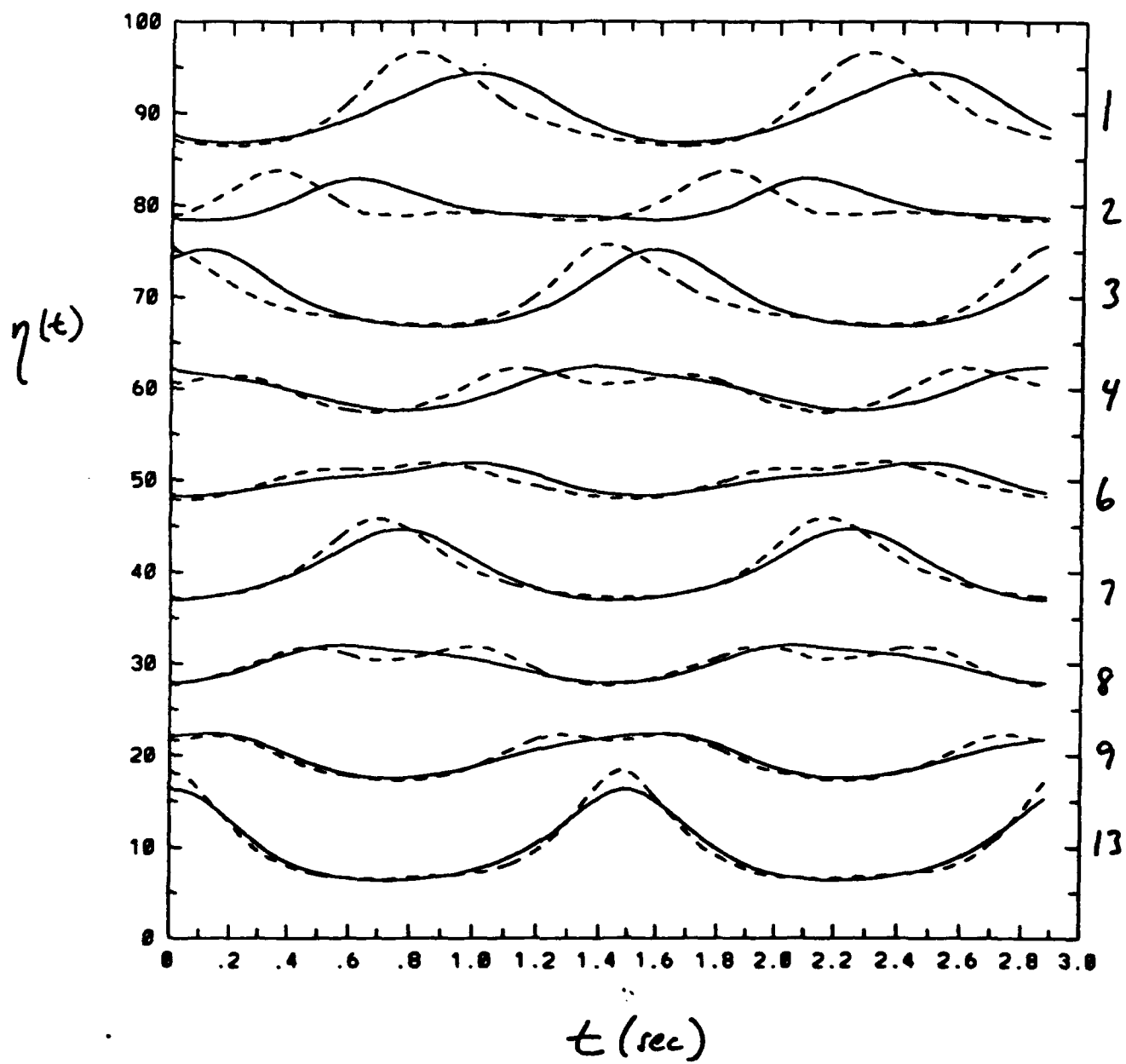


Figure 11

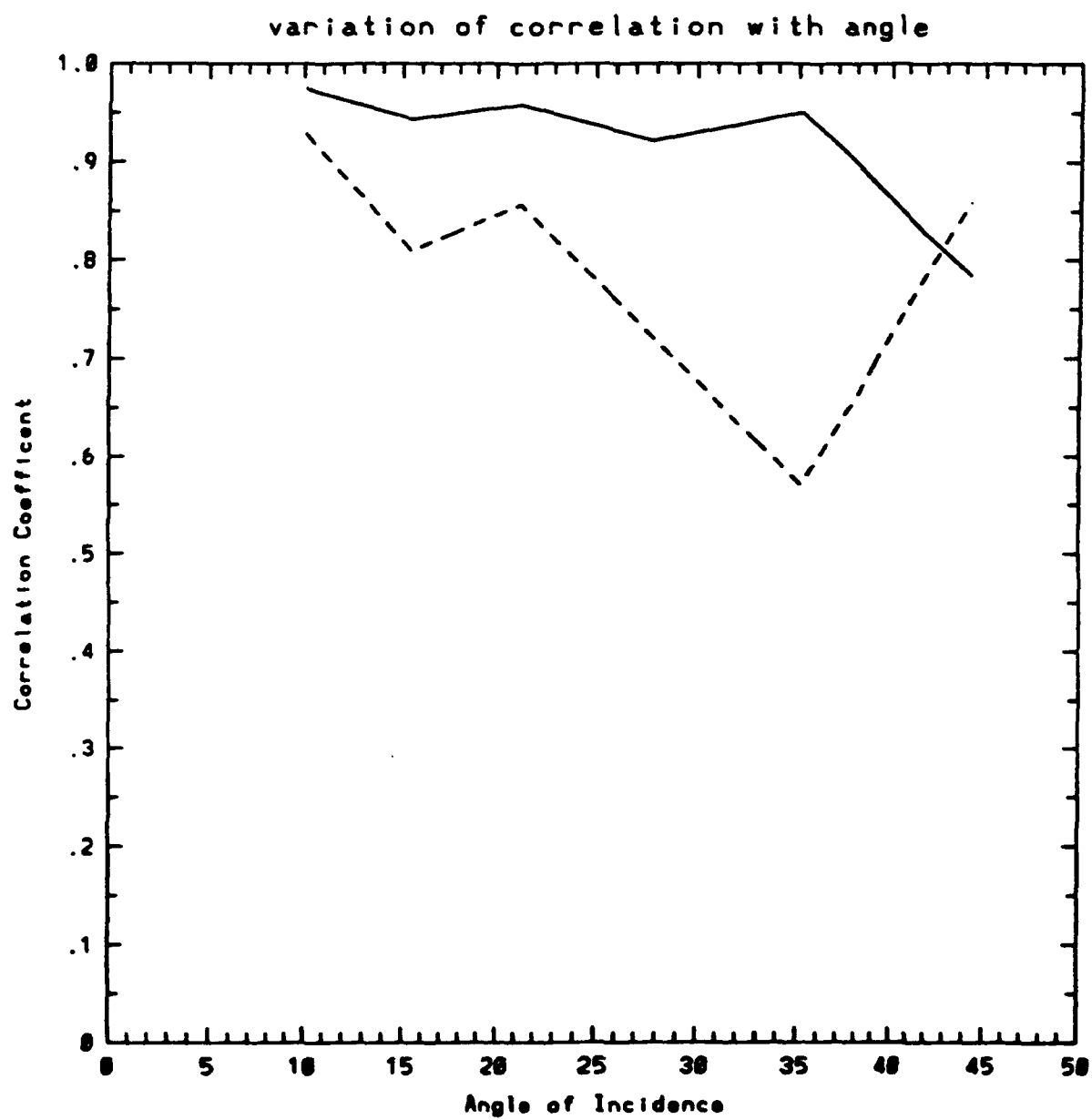
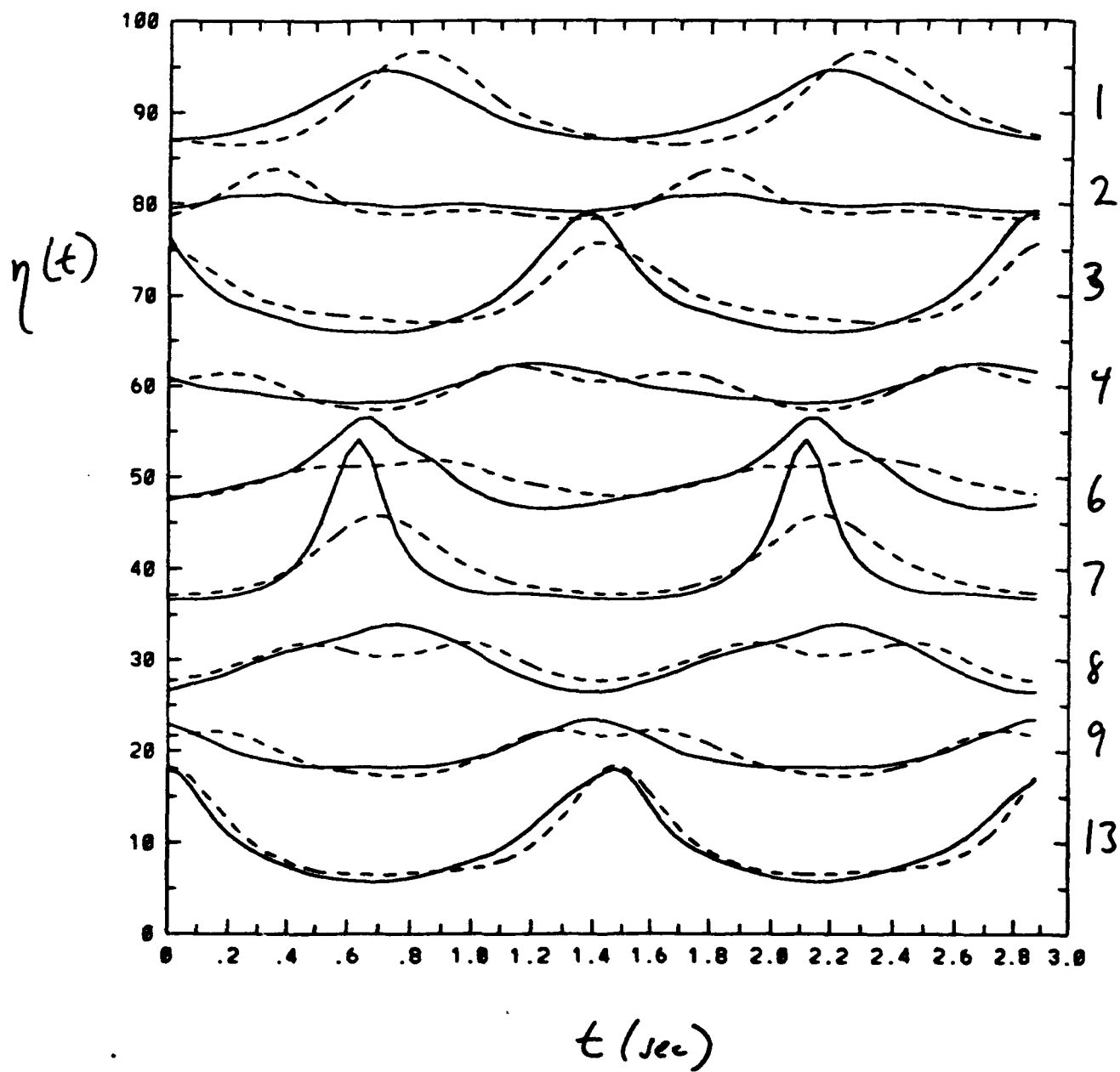


Figure 12



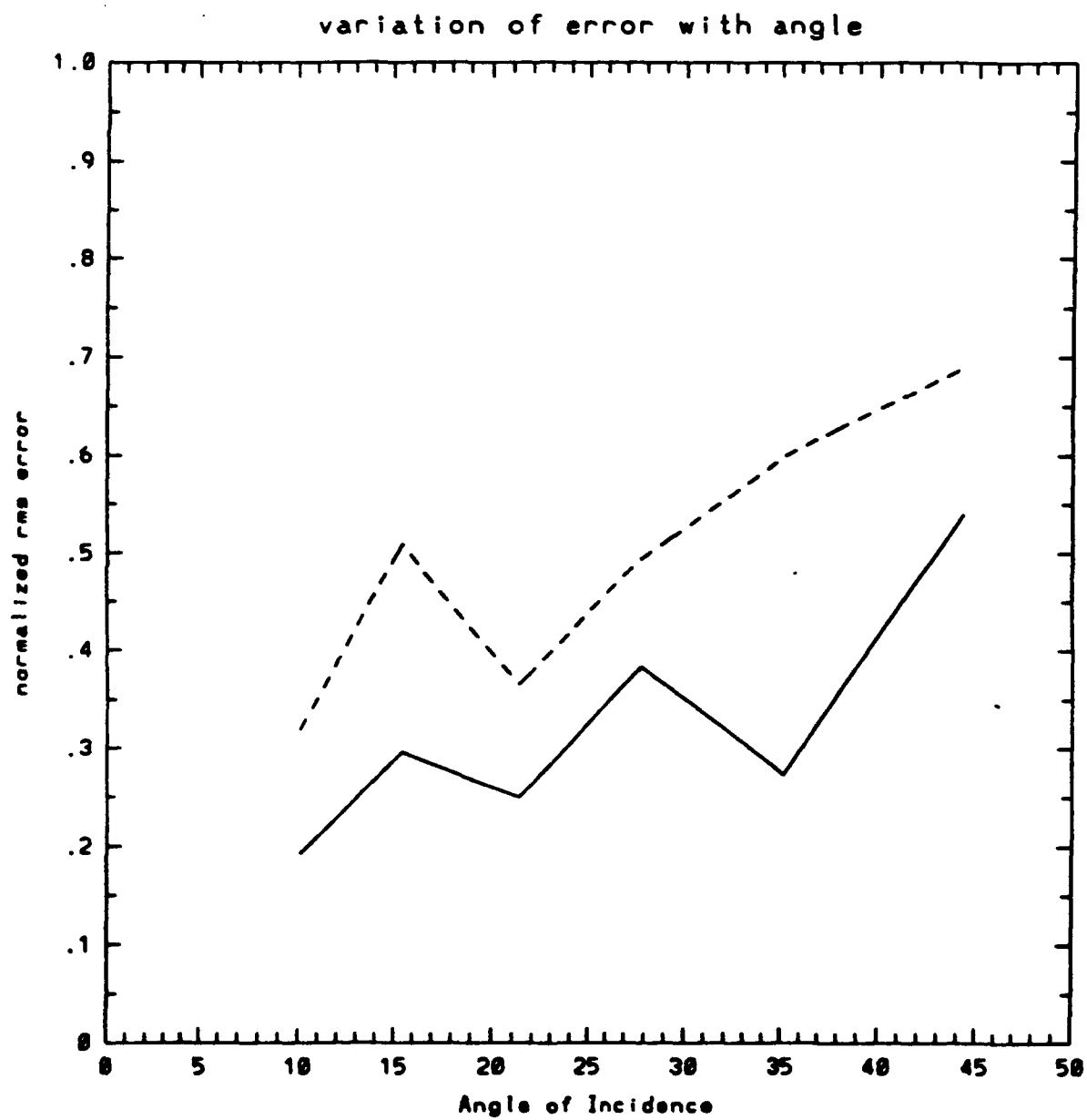


Figure 14

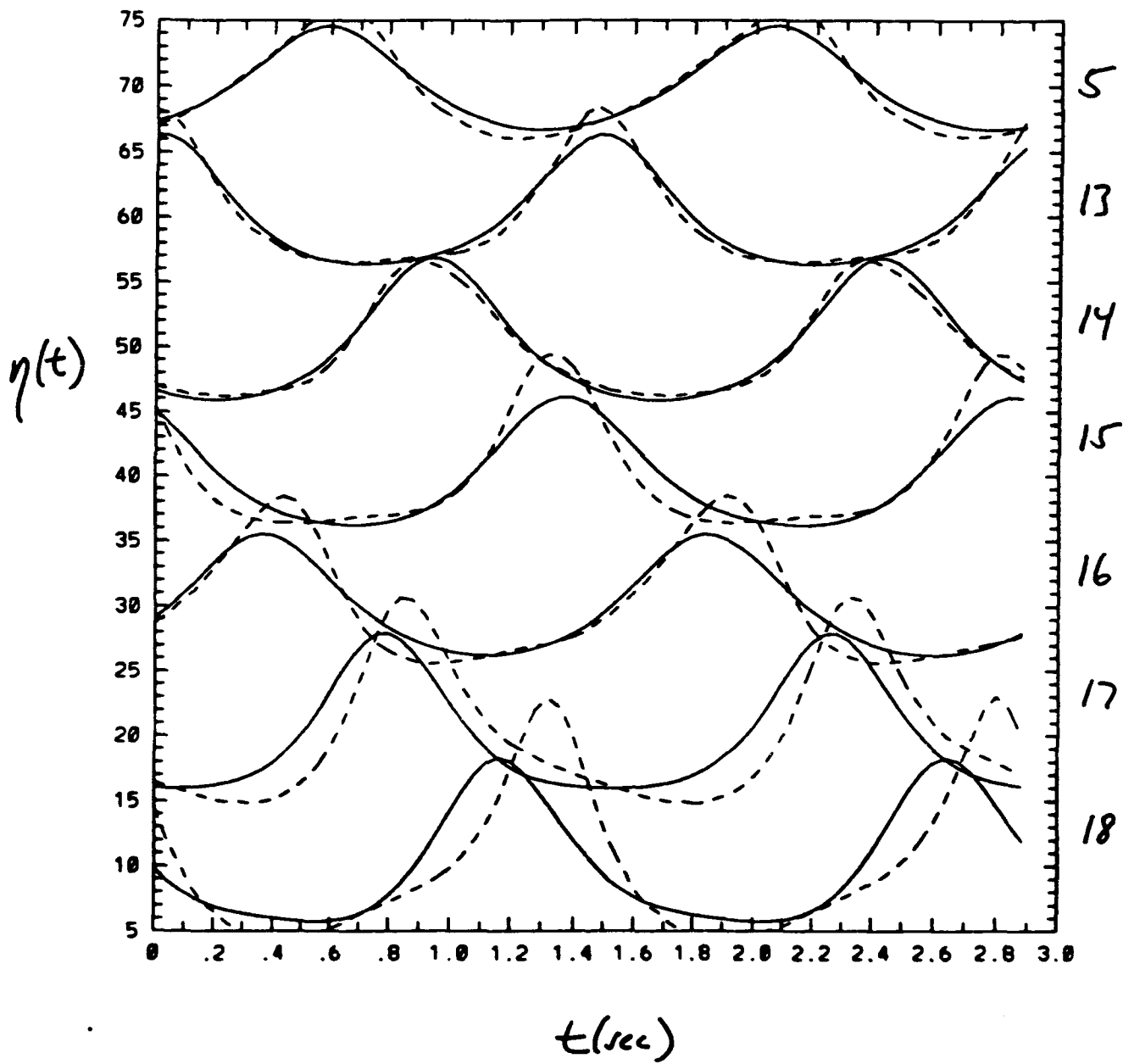


Figure 15

Appendix F: Angular Spectrum Modelling of Water Waves

to appear in *CRC Critical Reviews in Aquatic Science*, 1992.

Angular Spectrum Modelling of Water Waves

Robert A. Dalrymple and James T. Kirby
Center for Applied Coastal Research
University of Delaware
Newark, DE 19716

Contents

1	Introduction	2
2	The Angular Spectrum Model	4
2.1	Constant Depth	6
2.1.1	Wavemakers	8
2.1.2	Waves Behind Narrow Gaps	9
2.1.3	Wave Focussing	12
3	Variable Bathymetry	12
3.1	Straight and Parallel Contours	13
3.2	Realistic Bathymetry	14
3.3	Alternative Formulation of the Bottom Coupling Term	16
3.4	Nonlinear Effects	20
4	Shallow Water Waves	23
4.1	Shoaling waves	25
4.2	Comparison with Laboratory Data	26
5	Conclusions	27
6	References	29

1 Introduction

The propagation of water waves over an irregular bathymetry has served as an important area of research for mathematicians, oceanographers and ocean engineers for a long time due to the importance of the problem and the mathematical difficulties encountered in its solution. For example, the design of shore facilities (harbors, breakwaters and piers) and offshore structures requires a good knowledge of the wave heights and directions to be encountered at the site of interest.

Numerous models have been proposed in the past to solve various aspects of wave propagation. The first models were ray tracing models, which determine the path followed by the waves as they traverse irregular bathymetry (e.g., Munk and Arthur, 1952; Noda, 1974). These models, when used either from offshore towards the shore or in reverse, provide reasonable estimates for wave heights when refraction (due to variations in water depth normal to the direction of propagation) and shoaling (due to changes in water depth in the wave direction) are the dominant phenomena affecting the waves.

Computer models of nearshore circulation have required knowledge of the wave field at discrete grid points over an offshore region, which led to the development of models based on the irrotationality of the wave number. Examples of these models are Perlin and Dean (1983) and Dalrymple (1988). Despite the inclusion of numerous other effects (such as wave-current interaction and bottom friction by Dalrymple), none of these models incorporates the process of diffraction. Ebersole (1985) extended these models to include diffraction.

Diffraction, which is the turning of the wave rays due to gradients in wave amplitude, as would occur as waves pass a surface-piercing obstacle (e.g., breakwaters), was largely ignored for coastal situations due to the lack of a suitable model which would incorporate refraction and diffraction simultaneously. In the vicinity of breakwaters, the optics solution of Sommerfeld (1898) was adapted by Penney and Price (1952) for waves; however, the procedure by which refraction models would be patched locally into the diffraction solution remained an art for many years.

Of fundamental importance to the combined refraction/diffraction problem was the development of the mild-slope equation by Berkhoff (1972). This equation, which is the vertically-averaged equation for wave motion, reduces the 3-D problem of solving the Laplace equation to a 2-D problem for cases where the bottom does not vary greatly. This second order partial differential equation permits refraction and shoaling, as well as diffraction, to occur simultaneously. Numerous finite element models were developed to solve this equation (e.g., Berkhoff, 1972, Houston, 1981, and Bettess and Zienkiewicz, 1977).

Liu and Mei (1976) first developed a parabolic approximation to the problem of wave fields in the vicinity of shore-parallel breakwaters, in order to study the wave-induced circulation caused by the presence of the structure.

Radder (1979) developed the first parabolic representation of the mild-slope equation, leading to greater computational simplicity and the ability to neglect the downwave boundary condition, which in practice is very difficult to specify *a priori*. The parabolic modelling has

been explored more fully by Kirby and Dalrymple (1983) and Liu and Tsay (1984), who showed how to develop a weakly-nonlinear version of the mild-slope equation, allowing for amplitude dispersion (bigger waves travel faster than smaller ones).

One of the drawbacks of the parabolic modelling has been the restriction that the waves travel almost in a prescribed direction. The small-angle parabolic models for example require that the waves travel within $\pm 30^\circ$ of the x axis. Wider angle models have been developed by Booij (1981) and Kirby (1986a,b); however, each successive approximation only opens the range of allowed angles by a finite amount, and the limit of full $\pm 90^\circ$ is never approached. An alternative path taken by Lozano and Liu (1980) was to base the parabolic model on the underlying refracted wave field, such that the large angles due to refraction were taken care of properly prior to the diffraction calculations. However, diffraction effects still only occurred in a narrow range of angles around the principle ray direction.

Angular spectrum modelling has in principle no limitation on wave angle; hence, its development for water waves by Dalrymple and Kirby (1988), Dalrymple, Suh, Kirby and Chae (1989) and Suh, Dalrymple and Kirby (1990). The angular spectrum approach has been used in other fields, such as radio astronomy (Booker and Clemmow, 1950) and electromagnetic fields (Clemmow, 1966). Some references for the development of angular spectra are Goodman (1968; optics) and Stamnes (1986; optics and water waves).

The basic ideas behind the angular spectrum can be obtained by examining a single wave train on the surface of the ocean, which can be described at a point (x, y) in the horizontal plane as

$$\eta(x, y, t) = ae^{i(k \cos \theta x + k \sin \theta y - \omega t)} \quad (1.1)$$

where the real part of η is the displacement of the water surface about its mean position. a is the wave amplitude, k and ω are the wave number (defined as 2π over the wave length L) and the angular frequency (2π over the wave period T), respectively. The angle θ is the direction that the wave direction makes with the x axis, which points onshore. At $x=0$, the wave form can be separated into two parts,

$$\eta(0, y, t) = ae^{ik \sin \theta y} e^{-i\omega t} \quad (1.2)$$

Clearly there is a oscillatory variation of η in the y direction, which will be denoted by $\tilde{\eta}(y)$. Defining λ as $k \sin \theta$ we have

$$\tilde{\eta}(y) = ae^{i\lambda y} \quad (1.3)$$

For a more realistic sea state, the y variation of $\tilde{\eta}$ will be more complicated, say, $f(y)$, resulting from the superimposition of many wave trains with different directions, but with the same frequency ω . To determine the contributions of each of the many wave trains in $f(y)$, we can decompose it through the use of a Fourier transform in the y direction. The Fourier transform and its inverse for any function $f(y)$ defined on an infinitely wide domain are given by

$$\begin{aligned} \hat{f}(\lambda) &= \int_{-\infty}^{\infty} f(y) e^{-i\lambda y} dy \\ f(y) &= \frac{1}{2\pi} \int_{-\infty}^{\infty} \hat{f} e^{i\lambda y} d\lambda \end{aligned} \quad (1.4)$$

where the Fourier transform parameter is λ . The angular spectrum is $\hat{\eta}(\lambda)$, which consists of the amplitudes of the wave trains travelling in directions, $\theta = \sin^{-1}(\lambda/k)$. Thus, the angular spectrum is a (continuous) collection of wave trains, each travelling in a different direction, determined by the Fourier parameter, λ . The free surface displacement is now expressed as

$$\eta(x, y, t) = \frac{1}{2\pi} \int_{-\infty}^{\infty} \hat{\eta}(\lambda) e^{i\sqrt{k^2 - \lambda^2}x} e^{i\lambda y} d\lambda \quad (1.5)$$

where $k \cos \theta$ is rewritten as $\sqrt{k^2 - \lambda^2}$ using the definition of λ . (We note that the contributions from the integral from $|\lambda| > k$ are not propagating waves, as they decay in the x direction.)

2 The Angular Spectrum Model

The sea surface for many years has been described by a superposition of individual wave trains travelling in different directions, leading to a directional spectrum. The angular spectrum is very similar except that the directions are prescribed by Fourier analysis for each frequency, as we now show.

The directional frequency spectrum may be written

$$\eta(x, y, t) = \int_0^{\infty} \int_0^{2\pi} F(\omega, \theta) e^{i(k \cos \theta x + k \sin \theta y - \omega t)} d\theta d\omega \quad (2.1)$$

where the real part of η is the water surface elevation as a function of time at position (x, y) . $F(\omega, \theta)$ is the amplitude spectrum for the waves. If we now assume that we can separate $F(\omega, \theta)$ into a separate frequency and direction components, $F = S(\omega)D(\theta)$ then the above expression can be rewritten (replacing $k \sin \theta$ with the parameter λ and $k \cos \theta$ with $\sqrt{k^2 - \lambda^2}$) as

$$\eta(x, y, t) = \int_0^{\infty} S(\omega) \left\{ \int_{-k}^k \frac{D(\theta)}{\sqrt{k^2 - \lambda^2}} e^{i\sqrt{k^2 - \lambda^2}x} e^{i\lambda y} d\lambda \right\} e^{-i\omega t} d\omega \quad (2.2)$$

For the present time we will restrict ourselves to a single frequency, ω_0 , with an amplitude, $S_0 = S(\omega_0)d\omega$, and define the angular spectrum representation of the waves at that frequency as

$$\eta_{\omega_0}(x, y, t) = \int_{-k}^k S_0 \frac{D(\lambda)}{\sqrt{k^2 - \lambda^2}} e^{i\sqrt{k^2 - \lambda^2}x} e^{i\lambda y} d\lambda \quad (2.3)$$

The angular spectrum is defined as the complex amplitude of the waves,

$$A(\lambda) \equiv \frac{2\pi S_0 D(\lambda)}{\sqrt{k^2 - \lambda^2}}$$

The wave trains making up the angular spectrum are progressive (that is, $\sqrt{k^2 - \lambda^2}$ is real); however, for convenience and for analogy to the Fourier transform, we change the limits of integration to $\pm\infty$.

$$\eta_{\omega_0}(x, y, t) = \frac{1}{2\pi} \int_{-\infty}^{\infty} A(\lambda) e^{i\sqrt{k^2 - \lambda^2}x} e^{i\lambda y} d\lambda \quad (2.4)$$

The new additional wave trains that are added by extending the range of integration are all evanescent, decaying in the x direction as λ is greater than k and the x dependency becomes $\exp\{-\sqrt{\lambda^2 - k^2} x\}$. In this form, the wave spectrum now looks like the Fourier transform (1.5).

For a domain which repeats periodically in the transverse direction, we have the following Fourier transform pair,

$$\hat{f}_n(x, t) = \frac{1}{2b} \int_{-b}^b f(x, y, t) e^{-in\lambda y} dy \quad (2.5)$$

$$f(x, y, t) = \sum_{-\infty}^{\infty} \hat{f}_n e^{in\lambda y} \quad (2.6)$$

where now $\lambda = \pi/b$ and $2b$ is the width of the domain. The equivalent angular spectrum to Eq. 2.4 for a given frequency is

$$\eta(x, y, t) = \sum_{-\infty}^{\infty} A_n e^{i\sqrt{k^2 - (n\lambda)^2} x} e^{in\lambda y} \quad (2.7)$$

where wave trains of amplitude, A_n , propagate in discrete directions, measured by the angle θ_n to the x axis,

$$\theta_n = \tan^{-1} \left(\frac{n\lambda}{\sqrt{k^2 - (n\lambda)^2}} \right) \text{ for } n\lambda < k \text{ and } n = 1, 2, 3, \dots \quad (2.8)$$

Again, evanescent modes occur when $n\lambda > k$. Figure 1 shows a schematic of the angular spectrum, showing a number of wave directions. Sometimes these individual wave trains will be referred to as Fourier modes or simply modes.

For domains bounded laterally by impermeable barriers, solutions are sought in the form

$$f(x, y, t) = \sum_{n=0}^{\infty} \hat{f} \cos n\lambda y \quad (2.9)$$

where again $\lambda = \pi/b$, in order that

$$\frac{\partial f}{\partial y} = 0, \text{ at } y = \pm b,$$

or, for solutions which are non-symmetric about $y = 0$,

$$f(x, y, t) = \sum_{n=0}^{\infty} \hat{f}_e \cos n\lambda y + \sum_{n=0}^{\infty} \hat{f}_o \sin \gamma_n y \quad (2.10)$$

where the first series represents the even solution (symmetric about $y = 0$) and the second series is the antisymmetric part of the solution. The parameter $\gamma_n = (n + \frac{1}{2})\pi/b$.

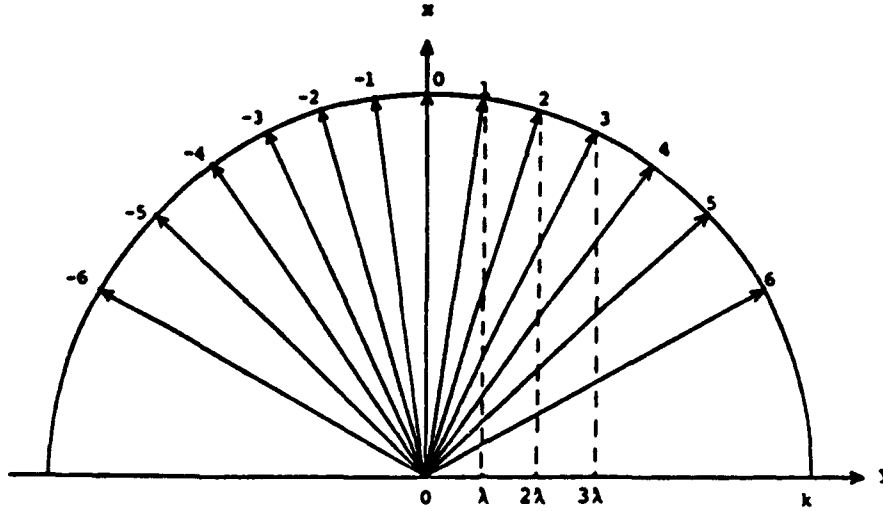


Figure 1: The Angular Spectrum

2.1 Constant Depth

To fix ideas, consider the onshore direction as the x direction and the transverse direction is the y direction; the coordinate z will point upward from the mean water level. The velocity potential for the wave motion is $\Phi(x, y, z, t)$, from which the velocities and water surface elevation can be determined (see, e.g., Dean and Dalrymple, 1984). For linear plane waves on constant depth, the boundary value problem is separable and the reduced potential must satisfy the Helmholtz equation,

$$\frac{\partial^2 \phi}{\partial x^2} + \frac{\partial^2 \phi}{\partial y^2} + k^2 \phi = 0 \quad (2.11)$$

where $\Phi(x, y, z, t) = \phi(x, y) \cosh k(h+z) e^{-i\omega t}$, and the wave number k and the angular wave frequency ω are related through the dispersion relationship,

$$\omega^2 = gk \tanh kh \quad (2.12)$$

Fourier transforming the differential equation in the y direction yields

$$\frac{d^2 \hat{\phi}}{dx^2} + (k^2 - \lambda^2) \hat{\phi} = 0 \quad (2.13)$$

which is an ordinary differential equation for $\hat{\phi}(x)$. The solution is

$$\hat{\phi}(x) = A e^{i\sqrt{k^2 - \lambda^2} x} \quad (2.14)$$

where A is a function of λ (but constant in x) which must be determined. The Fourier inverse in an infinitely wide domain is

$$\phi(x, y) = \frac{1}{2\pi} \int_{-\infty}^{\infty} A(\lambda) e^{i(\sqrt{k^2 - \lambda^2} x + \lambda y)} d\lambda \quad (2.15)$$

At $x = 0$,

$$\phi(0, y) = \int_{-\infty}^{\infty} A(\lambda) e^{i\lambda y} d\lambda \quad (2.16)$$

Comparing with Equations (1.4), we see the boundary condition for $A(\lambda)$,

$$A(\lambda) = \int_{-\infty}^{\infty} \phi(0, y) e^{-i\lambda y} dy \quad (2.17)$$

It should be emphasized that the solution we have obtained (2.15, 2.17) for this linear wave field is fixed by the initial condition at $x = 0$, as there is no coupling between the various modes comprising the angular spectrum. If the problem of interest is wave propagation behind a breakwater, with all the attendant diffraction, the angular spectrum model shows that the wave behavior is solely determined by the initial condition, i.e., the diffraction the waves experience behind a breakwater is determined by the initial condition at the breakwater as each of the wave trains comprising the angular spectrum propagate independently of each other. The diffraction pattern observed is created by the radial spreading of the wave trains comprising the angular spectrum.

For a periodic domain of lateral extent $2b$, the Fourier transform leads to

$$\frac{d^2 \hat{\phi}}{dx^2} + (k^2 - (n\lambda)^2) \hat{\phi} = 0 \quad (2.18)$$

with the solution

$$\hat{\phi}(x, n\lambda) = A_n e^{i\sqrt{k^2 - (n\lambda)^2} x} \quad (2.19)$$

The inverse is

$$\Phi(x, y, z, t) = \sum_{-\infty}^{\infty} A_n e^{i(\sqrt{k^2 - (n\lambda)^2} x + n\lambda y - \omega t)} \cosh k(h + z) \quad (2.20)$$

The wave number vector $\vec{k} = (k \cos \theta, k \sin \theta) = (\sqrt{k^2 - (n\lambda)^2}, n\lambda)$.

Again, the behavior of the wave trains as they propagate is fixed by the initial conditions in this problem, which are ascertained by a Fourier transform of the initial conditions, $\hat{\phi}_n(0, y) = A_n$. For example, for a plane wave train propagating at angle, γ to the x axis, the initial value of $\phi(0, y) = D e^{i\lambda_0 y}$, where $\lambda_0 = k \sin \gamma$. The Fourier transform of this initial condition, again for a periodic domain, is

$$A_n = 2Db \sin(\lambda_0 - n\lambda)b,$$

unless $\lambda_0 = m\lambda$ for some integer, m , in which case all the A_n are zero, except for A_m , which is $2Db$. For computational purposes, it is convenient to choose incident plane wave trains which correspond to a Fourier mode.

The conservation of energy equation can be used as a check for numerical calculations in periodic domains, as the energy fluxes through the lateral boundaries cancel and therefore

the flux of energy across any plane parallel to the y axis is a constant. If the energy flux is defined as

$$\mathcal{F} = - \int_{-b}^b \rho \frac{\partial \Phi}{\partial t} \frac{\partial \Phi}{\partial x} dy dz, \quad (2.21)$$

then the flux past any location in terms of the Fourier coefficients, A_n , can be shown to be

$$\rho \omega \frac{CC_g}{g} b \sum_n^{\infty} |A_n|^2 \sqrt{k^2 - (n\lambda)^2} = \text{constant} \quad (2.22)$$

2.1.1 Wavemakers

The solution for $\phi(x, y)$ in constant depth water (2.15, 2.17) can be used to determine the wave field inside directional wave basins, which are typically rectangular basins with segmented wavemakers along one wall (Dalrymple and Greenberg, 1985). For an example, we will assume the basin is infinitely wide (y direction) with the x axis located at the center of the wavemaker pointing into the basin.

Equation (2.16) indicates that the wave field is known, once the velocity potential is specified along the wavemaker; however, the usual linearized wavemaker boundary condition specifies the velocity in the x direction at $x=0$ (see Dean and Dalrymple, 1984, for example). Therefore we need to treat this problem slightly differently.

We will take the horizontal velocity created by the wavemaker of length $2a$ (associated with the progressive wave mode) to be adequately described by

$$\frac{d\phi(0, y)}{dx} = \begin{cases} e^{i\lambda_0 y}, & |y| < a \\ 0, & |y| > a \end{cases} \quad (2.23)$$

where $\lambda_0 = k \sin \gamma$ and γ measures the desired wave direction. The Fourier transform of this condition is

$$\frac{d\widehat{\phi(0, \lambda)}}{dx} = \frac{2 \sin(\lambda_0 - \lambda)a}{(\lambda_0 - \lambda)} \quad (2.24)$$

From the solution for $\phi(x, y)$, we have

$$\frac{d\phi(0, y)}{dx} = \frac{1}{2\pi} \int_{-\infty}^{\infty} i\sqrt{k^2 - \lambda^2} A(\lambda) e^{i\lambda y} d\lambda \quad (2.25)$$

and, after transforming,

$$\frac{d\widehat{\phi(0, \lambda)}}{dx} = i\sqrt{k^2 - \lambda^2} A(\lambda) \quad (2.26)$$

Equating these two expressions for the transformed velocity, we find

$$A(\lambda) = -\frac{2i \sin(\lambda_0 - \lambda)a}{(\lambda_0 - \lambda)\sqrt{k^2 - \lambda^2}} \quad (2.27)$$

This gives the final form for the velocity potential in the basin

$$\phi(x, y) = -\frac{i}{2\pi} \int_{-\infty}^{\infty} \frac{2 \sin(\lambda_0 - \lambda)a}{(\lambda_0 - \lambda)} \frac{e^{i\sqrt{k^2 - \lambda^2} x}}{\sqrt{k^2 - \lambda^2}} e^{i\lambda y} d\lambda \quad (2.28)$$

The convolution theorem allows this expression to be rewritten into the form shown by Dalrymple and Greenberg (1985) and Dalrymple and Kirby (1988),

$$\phi(x, y) = \frac{i}{2} \int_{-a}^a e^{i\lambda \zeta} H_0^{(1)}(k\sqrt{x^2 - (y - \zeta)^2}) d\zeta \quad (2.29)$$

which is also obtainable through a Greens function approach. Dalrymple and Greenberg (1985) also treated the evanescent modes which are important in the vicinity of the wave-maker. Stamnes (1986) shows how to obtain the evanescent modes in the context of an angular spectrum.

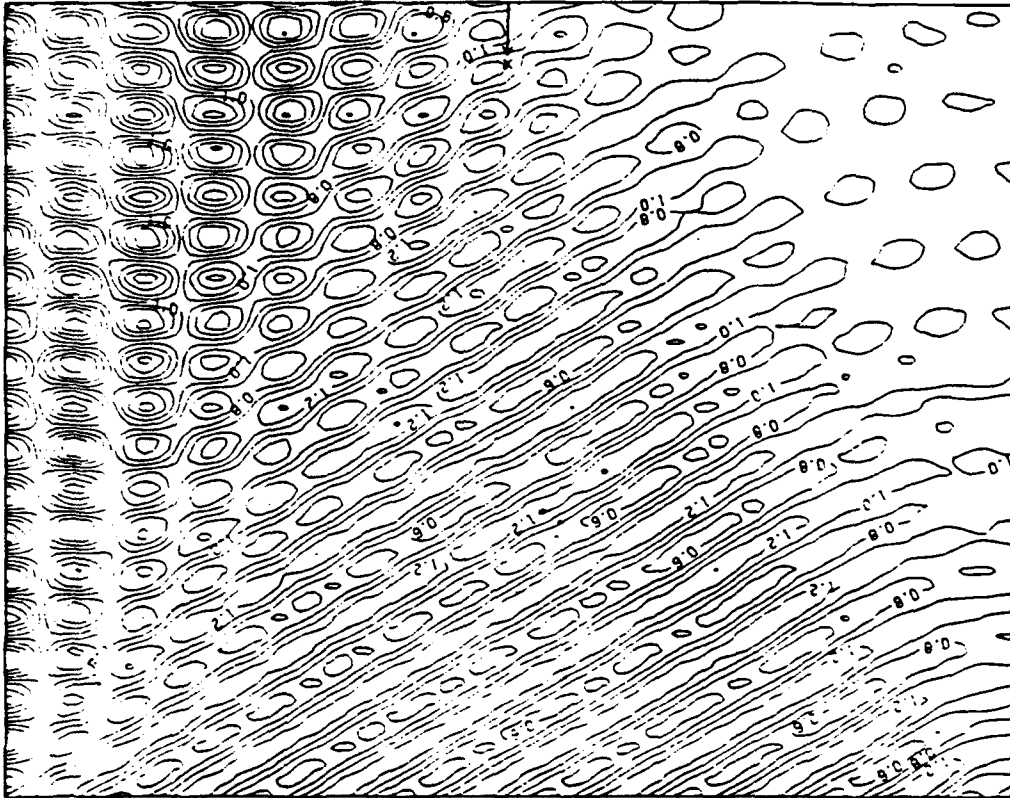
Dalrymple and Kirby (1988) point out that the wave field behind a thin island of width $2a$ can be easily found by taking the plane wave solution and subtracting the wavemaker solution from it, according to Babinet's Principle.

Dalrymple (1989) has used this constant depth solution and the non-symmetric Fourier expansion (2.10) to determine the wave fields generated by directional wavemakers in basins of finite width, taking into account side wall reflection. This is the so-called 'designer waves' solution. (His solution is also valid for basins with straight and parallel bottom contours.)

To illustrate the 'designer wave' concept, see Figure 2, which show the instantaneous water surface for a wave train with 30° angle of incidence which is generated at the wavemaker, located at the bottom of the figure. Due to the presence of the reflecting wall at the left of the figure, a short-crested wave pattern is created. The presence of the side wall at the right of the figure creates a diffraction zone. There is only a limited portion of the wave basin near the wavemakers, where the desired wave train exists. At the far end of the tank (at the top of the figure), the wave field is clearly no longer a uniform wave train. Now, if this long-crested wave train is desired to occur at the far end of the tank, then the power of a directional wavemaker can be used. By generating a nonuniform wave field, the presence of the side walls can be incorporated in the wavemaker signals. For example, to generate a wave train with 30° angle of incidence at the far end of the basin, the wavemaker must generate short-crested and diffracted waves. For this case, if we now imagine the wavemaker at the top of the same figure, we see that by the time the wave field propagates to the far end of the tank (now the bottom of Figure 2), the wave becomes long-crested. This technique, including shoaling waves, is used in the Ocean Engineering Laboratory at the University of Delaware.

2.1.2 Waves Behind Narrow Gaps

Another interesting application of this constant depth solution is the propagation of a directional sea state through a small gap. This problem can be treated in several ways. First the influence of the waves on the seaward side of the breakwater could be neglected, in which



case the wavemaker solution could be used directly with the appropriate specification of the velocity. Alternatively the offshore wave field can be specified and matched at the gap to the wavefield on the sheltered side of the breakwater. This is the case we will treat.

Consider either a natural gap through which waves must propagate into an embayment or a man-made gap, as between two breakwater segments. It has been noticed that, regardless of how directional the sea state seaward of the gap is, the waves inshore of the gap are long-crested and these crests are circular. To show that this is true, we postulate an angular spectrum for the waves offshore of the (infinitesimally narrow) gap for a given frequency as

$$\phi_o(x, y) = \frac{1}{2\pi} \int_{-\infty}^{\infty} A(\lambda) e^{i\sqrt{k^2 - \lambda^2}x} e^{i\lambda y} d\lambda \quad (2.30)$$

where the $A(\lambda)$ are imposed by the nature of the offshore sea state. The velocity at the gap is

$$\frac{\partial \phi_o(0, y)}{\partial x} = \frac{1}{2\pi} \int_{-\infty}^{\infty} i\sqrt{k^2 - \lambda^2} A(\lambda) e^{i\lambda y} d\lambda \delta(y) \quad (2.31)$$

where the $\delta(y)$ is the Dirac delta function, which represents the fact that the velocity is zero except at the narrow gap. The Fourier transform:

$$\frac{\partial \widehat{\phi_o(0, y)}}{\partial x} = \frac{1}{2\pi} \int_{-\infty}^{\infty} i\sqrt{k^2 - \lambda^2} A(\lambda) d\lambda \quad (2.32)$$

Inside the (infinitely thin) breakwater, the wave field for this frequency is given by another angular spectrum,

$$\phi_i(x, y) = \int_{-\infty}^{\infty} B(\lambda) e^{i\sqrt{k^2 - \lambda^2}x} e^{i\lambda y} d\lambda \quad (2.33)$$

The transformed horizontal velocity (x direction) at the gap is

$$\frac{\partial \widehat{\phi_i(0, y)}}{\partial x} = i\sqrt{k^2 - \lambda^2} B(\lambda) \quad (2.34)$$

Equating both of the velocities yields

$$B(\lambda) = \frac{1}{2\pi} \frac{\int_{-\infty}^{\infty} \sqrt{k^2 - \lambda^2} A(\lambda) d\lambda}{\sqrt{k^2 - \lambda^2}} \quad (2.35)$$

We can make several assumptions here for $A(\lambda)$. If we assume that the wave trains are coming from all directions with the same height (a), then $A(\lambda) = a$; alternatively if the waves come only from the direction associated with λ_0 , then $A(\lambda) = A(\lambda_0)\delta(\lambda_0 - \lambda)$. For both cases, the integral in the above expression can be evaluated, such that

$$B(\lambda) = \frac{ak^2}{4\sqrt{k^2 - \lambda^2}} \quad (2.36)$$

or

$$B(\lambda) = \frac{-iA(\lambda_0)}{\sqrt{k^2 - \lambda^2}} \quad (2.37)$$

Substituting these expression into the angular spectrum inside the breakwater, (2.33), and integrating, we have

$$\phi_i(x, y) = \alpha H_0(kr) \quad (2.38)$$

where, for the first case, $\alpha = ak^2/2$ and, for the second case, $\alpha = -iA(\lambda_0)/2$. The Hankel function of the first kind and order zero, which is a function of the wavenumber and the radial distance $r = \sqrt{x^2 + y^2}$, arrives through the following identity:

$$\frac{1}{2\pi} \int_{-\infty}^{\infty} \frac{e^{i\sqrt{k^2 - \lambda^2}x} e^{i\lambda y} d\lambda}{\sqrt{k^2 - \lambda^2}} = \frac{i}{2} H_0(kr) \quad (2.39)$$

The nature of our solution for one frequency is that the wave form inside the bay, which is only dependent on the radial distance from the gap, is described by circular wave crests (via the Hankel function). For the linear superposition of many frequencies, the same result obtains—all frequencies are described by circular wave crests.

For waves through a breakwater gap much smaller than a wavelength, the result is not new, Penney and Price (1952).

Dalrymple and Martin (1990) examine the wave field inshore of a line of breakwaters that are separated by gaps of the same length (similar to an optical grating). The influence of the offshore waves is included in their analysis. They find that the wave field inshore of the breakwater can be very complicated as new wave modes are generated when the gap spacing is less than a wave length, due to superposition of the diffraction patterns behind each gap. The presence of multiple wave trains of the same frequency can lead to the formation of rip currents behind such structures.

2.1.3 Wave Focussing

Stamnes *et al.* (1983) carried out a laboratory and theoretical study of the focussing of waves behind a submerged shoal, designed to act as a Fresnel lens. The field experiment consisted of generating a circular wave with a point wavemaker; these waves were focussed by the lens to another (focal) point. Wave height measurements were made with densely spaced transects in the vicinity of the focal point. The comparisons to the data were made using the (linear) angular spectrum approach, along with a nonlinear parabolic model. The comparison was carried out by assuming the wave field over the lens was representable by a arc of a circular wave converging on the focal point.

3 Variable Bathymetry

Most coastal regions of interest are not characterized by uniform depth, but instead have spatial nonuniformity in bathymetry. At the simplest, this spatial variation is characterized by a trend of decreasing depth in the shoreward direction, with a superposed, irregular depth variation in both the on-offshore and longshore direction. For the case of intermediate

water depth, it is convenient to model small amplitude waves using the mild-slope equation (Berkhoff, 1972; Smith and Sprinks, 1975),

$$\nabla \cdot CC_g \nabla \phi + k^2 CC_g \phi = 0 \quad (3.1)$$

which is applied separately to each frequency component in the wave train. Here, $\nabla = (\frac{\partial}{\partial x} \vec{i} + \frac{\partial}{\partial y} \vec{j})$ is the horizontal gradient operator, C is the wave phase celerity and C_g is the group velocity of the waves, given by

$$C(x, y) = \omega / k(x, y) \quad (3.2)$$

$$C_g(x, y) = \frac{1}{2} \left(1 + \frac{2kh}{\sinh 2kh} \right) C \quad (3.3)$$

Again, the complete velocity potential is $\Phi(x, y, z, t) = \phi(x, y) \cosh k(h+z) e^{-i\omega t}$. The coefficients, C and C_g , in (3.1) are determined based on the local value of the water depth $h(x, y)$ at each point in the domain of interest and the dispersion relationship (2.12).

3.1 Straight and Parallel Contours

The Fourier transform of (3.1) for an infinitely wide domain where the depth only varies in the x direction is

$$\frac{d}{dx} \left(CC_g \frac{d\hat{\phi}}{dx} \right) + (k^2 - \lambda^2) CC_g \hat{\phi} = 0 \quad (3.4)$$

This ordinary differential equation for $\hat{\phi}$ has variable coefficients as the wave number, wave phase, and group velocities vary with the depth, $h(x)$.

An assumed form of the solution for $\hat{\phi}$ is

$$\hat{\phi}(x) = \tilde{\phi}(x) e^{i \int \sqrt{k^2 - \lambda^2} dx} \quad (3.5)$$

where $\tilde{\phi}$ is assumed to vary slowly in x as the exponential term carries most of the phase information and the integral is necessary to get the phase change with x correctly. Substituting into equation (3.4) leaves an equation for $\tilde{\phi}$,

$$CC_g \sqrt{k^2 - \lambda^2} \frac{d\tilde{\phi}}{dx} + \frac{d(CC_g \sqrt{k^2 - \lambda^2} \tilde{\phi})}{dx} = 0 \quad (3.6)$$

where we have neglected two small terms,

$$CC_g \frac{d^2 \tilde{\phi}}{dx^2} \ll 1 \quad (3.7)$$

$$\frac{\partial CC_g}{\partial x} \frac{d\tilde{\phi}}{dx} \ll 1 \quad (3.8)$$

as the bottom varies slowly in x as does $\tilde{\phi}$.

The resulting equation is a first order differential equation for the wave modes which can be solved by separation, resulting in

$$\bar{\phi} = A_0 \frac{\sqrt{CC_g \sqrt{k^2 - \lambda^2}}_0}{\sqrt{CC_g \sqrt{k^2 - \lambda^2}}} = A_0 K_s(\lambda) K_r(\lambda) \quad (3.9)$$

or

$$\hat{\phi} = A_0 K_s K_r e^{i \int \sqrt{k^2 - \lambda^2} dx} \quad (3.10)$$

where the terms with a zero subscript are evaluated at the origin. This equation shows that the (transformed) wave form is given by an initial amplitude, A , evaluated at $x = 0$ and then the wave changes with x in accordance with standard shoaling and refraction coefficients, K_s, K_r . Furthermore there is no interaction between the different Fourier modes; any diffraction observed for $x > 0$ is due to the spreading of the angular spectrum, as each wave train propagates in a different direction.

The inverse Fourier transform yields

$$\Phi = \frac{1}{2\pi} \int_{-\infty}^{\infty} A K_s K_r e^{i \int \sqrt{k(x)^2 - \lambda^2} dx} e^{i\lambda y} d\lambda \quad (3.11)$$

for an infinitely wide domain. This is a generalization of the result of Mei *et al.* (1968), who used a multiple scales approach, to now include all possible wave trains in a directional sea.

Dalrymple and Kirby (1988) studied the case of waves propagating through gaps in a row of periodically spaced offshore breakwaters, assuming that the potential through the gaps could be given as the wave potential in the absence of the breakwaters (known as the Kirchhoff approximation in optics). Shoreward of the breakwater the assumed planar bottom sloped upwards to the shoreline. Their results, see Figure 3, show diffraction patterns behind each of the breakwater gaps as would be expected, including the refraction of the waves due to the sloping bottom. There is also a region of short-crested waves due to the influence of neighboring gaps.

3.2 Realistic Bathymetry

For more realistic bathymetry, we must permit a variation in the bathymetry in the y direction as well. It is convenient to modify the mild-slope equation to treat this problem. Introducing $p(x, y) = CC_g$ and $\bar{\phi} = \sqrt{p}\phi$, we obtain a Helmholtz equation for the modified potential,

$$\nabla^2 \bar{\phi} + k_c^2 \bar{\phi} = 0 \quad (3.12)$$

where

$$k_c^2 = k^2 - \frac{\nabla^2 \sqrt{p}}{\sqrt{p}} \quad (3.13)$$

Following Dalrymple *et al.*, 1989, a laterally averaged wave number is introduced for a domain of width, $2b$,

$$\bar{k}^2 = \frac{1}{2b} \int_0^b k_c^2 dy$$

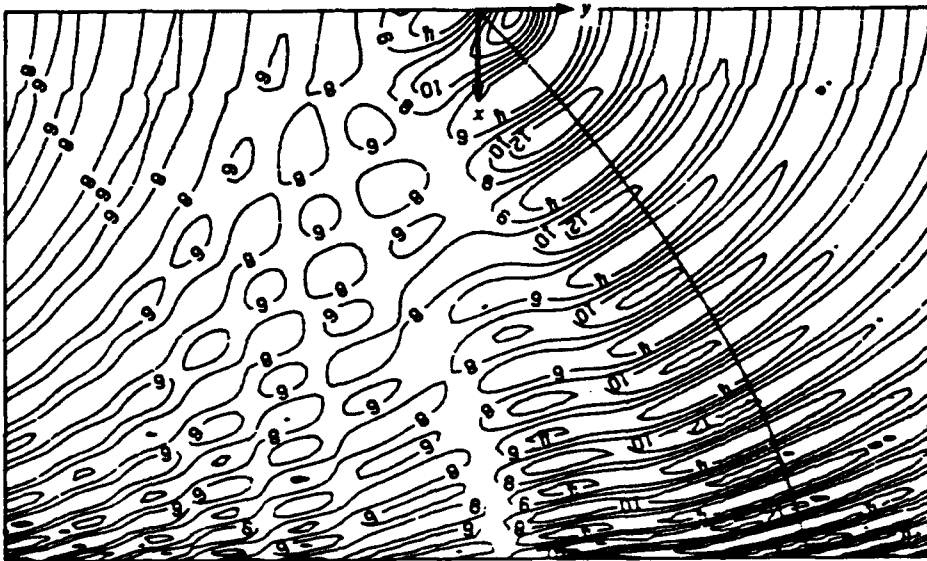


Figure 3: Instantaneous Wave Field Behind a Breakwater Gap Over a Sloping Bottom, from Dalrymple and Kirby (1988)

This permits rewriting the Helmholtz equation as

$$\nabla^2 \bar{\phi} + \bar{k}^2 \phi - \bar{k}^2 \nu^2 \phi = 0 \quad (3.14)$$

where $\nu^2(x, y)$ represents the lateral deviation of $\bar{k}(x)$ from $k_c(x, y)$:

$$\bar{k}^2 \nu^2 = \bar{k}^2 - k_c^2.$$

For bathymetries which have very little variation in the y direction, the ν^2 is small.

Fourier transforming (3.14) yields an equation for the Fourier modes,

$$\frac{d^2 \hat{\phi}}{dx^2} + (\bar{k}^2 - \lambda^2) \hat{\phi} - \bar{k}^2 F(\nu^2 \bar{\phi}) = 0 \quad (3.15)$$

where the Fourier transform of the product, $\nu^2 \bar{\phi}$ is shown symbolically with the F operator.

This second order differential equation can be separated into two equations (as is done for developing parabolic equations), one equation governing waves propagating in the positive x direction and another for the opposite direction, which, after assuming that the negatively propagating wave motion is small, due to only small amounts of reflection, yields one equation,

$$\frac{d\hat{\phi}(x, \lambda)}{dx} = i\sqrt{\bar{k}^2 - \lambda^2} \hat{\phi} - \frac{(\sqrt{\bar{k}^2 - \lambda^2})}{2\sqrt{\bar{k}^2 - \lambda^2}} x \hat{\phi} - \frac{i\bar{k}^2 F(\nu^2 \bar{\phi})}{2\sqrt{\bar{k}^2 - \lambda^2}} \quad (3.16)$$

The second term on the right hand side is the shoaling and refraction term, which occurs for planar bathymetry, and the last term represents the effect of the irregular bathymetry. This bathymetric effect represents a coupling between all Fourier wave modes and the bottom due to refraction. Modes which do not exist can be created by this interaction.

The example used by Dalrymple, Suh, Kirby and Chae (1989) is that of a submerged circular shoal located in a region of constant depth. as studied in the laboratory by Ito and Tanimoto (1972). The evolution of the modes over and behind the shoal are shown in Figure 4. The incident wave train is specified to have only one direction (mode). As the wave train encounters the shoal, the waves refract and focus due to the depth changes. Through the bottom term, new Fourier modes are spawned and grow over the island. Behind the island, in the constant depth region, the bottom coupling term is no longer active and the angular spectrum is unchanged with further propagation distance, yet the wave field experiences the formation of a strong focal region, where diffraction is important. The apparent diffraction once again is explained by the radial propagation of the individual members of the angular spectrum, generated by refraction over the shoal. The envelope of the wave field in the vicinity of the shoal is shown in Figure 5.

3.3 Alternative Formulation of the Bottom Coupling Term

Due to the efficiency of the FFT algorithm, the Fourier transform of the last term in (3.16) and the inverse transform needed to obtain $\bar{\phi}$ from $\hat{\phi}$ are usually evaluated over a periodic

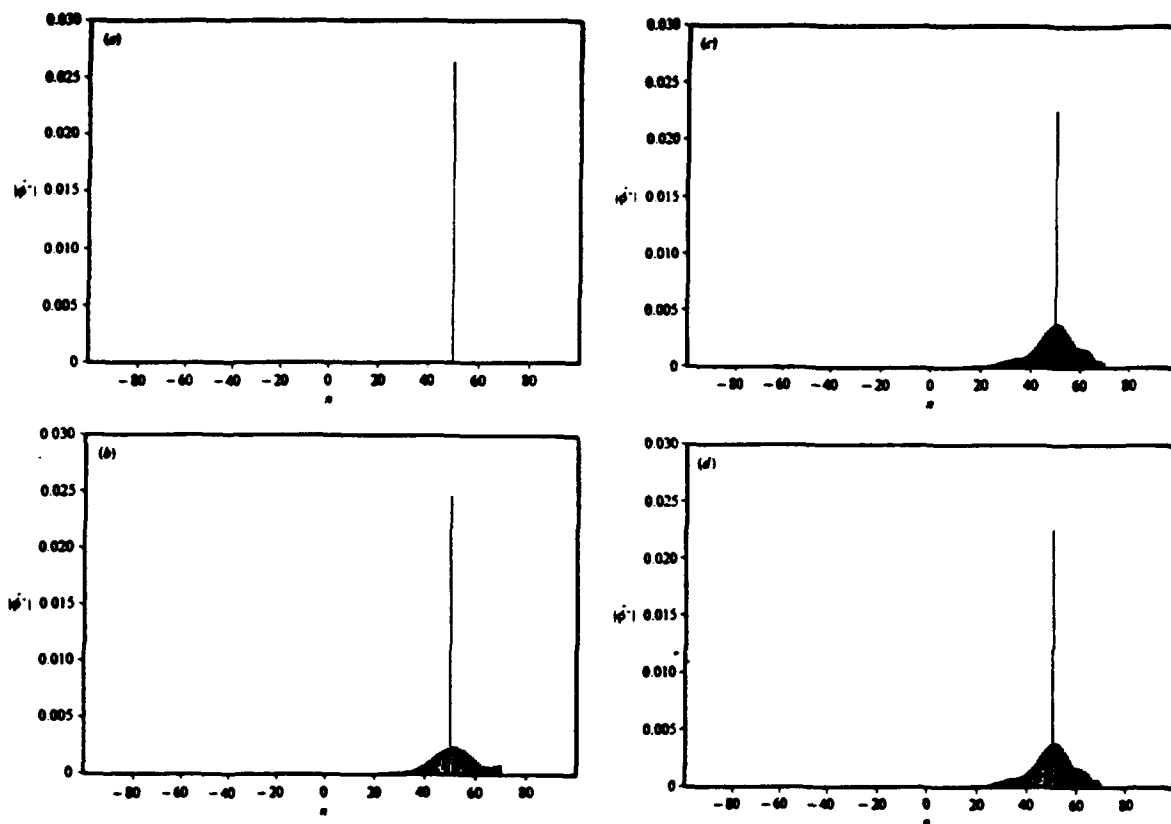


Figure 4: Evolution of the Angular Spectrum over a Circular Shoal, from Dalrymple *et al.*, 1989. (a) Seaward of Shoal, (b) Over the Top of the Shoal, (c) Just Landward of the Shoal, (d) Far Landward of the Shoal (note: no change from (c) to (d)).

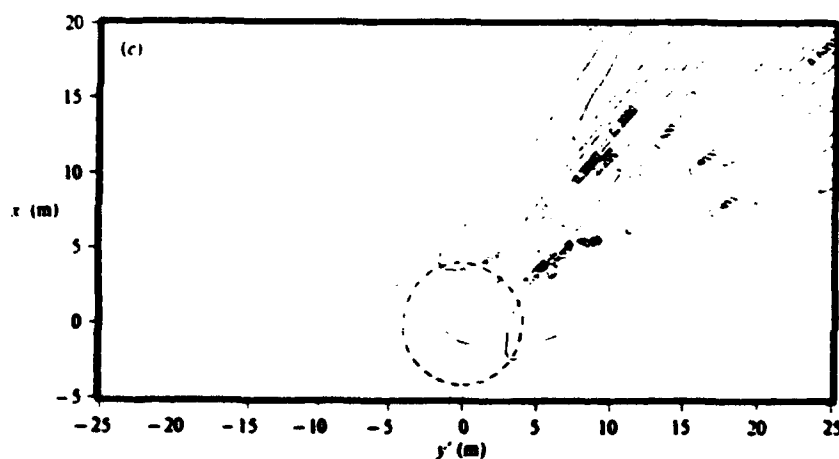


Figure 5: Envelope of the Wave Amplitude Behind a Circular Shoal for 45° of Incidence, from Dalrymple *et al.*, 1989

interval in a finite width domain. Using this fact about the computational procedure allows the effect of the coupling term to be directly interpreted in terms of mode coupling between transverse surface wave modes and transverse bottom modes. In order to show this, let

$$f(y) = \nu^2 \bar{\phi} \quad (3.17)$$

denote the real-valued argument of F on the line $-b \leq y \leq b$. The Fourier transform pair for f is then defined by the transform pair, (2.5, 2.6).

$$f(y) = \sum_{n=-\infty}^{\infty} \hat{f}_n e^{in\lambda y}; \quad \lambda = \frac{\pi}{b} \quad (3.18)$$

$$\hat{f}_n = \frac{1}{2b} \int_{-b}^b f(y) e^{-in\lambda y} dy \quad (3.19)$$

Likewise, the discrete transforms ϕ_n, ν_n^2 of the physical variables $\bar{\phi}, \nu^2$ are defined by

$$\begin{pmatrix} \bar{\phi}(y) \\ \nu^2(y) \end{pmatrix} = \sum_{n=-\infty}^{\infty} \begin{pmatrix} \phi_n \\ \nu_n^2 \end{pmatrix} e^{in\lambda y}; \quad \lambda = \frac{\pi}{b} \quad (3.20)$$

$$\begin{pmatrix} \phi_n \\ \nu_n^2 \end{pmatrix} = \frac{1}{2b} \int_{-b}^b \begin{pmatrix} \bar{\phi}(y) \\ \nu^2(y) \end{pmatrix} e^{-in\lambda y} dy \quad (3.21)$$

The discrete Fourier transform of the governing equation (3.15) gives

$$\frac{d^2 \phi_n}{dx^2} + (\bar{k}^2 - (n\lambda)^2) \phi_n - \bar{k}^2 \hat{f}_n = 0 \quad (3.22)$$

By direct substitution, we obtain

$$f(y) = \sum_l \sum_m \nu_l^2 \phi_m e^{i(l+m)\lambda y} \quad (3.23)$$

Then

$$\begin{aligned} \hat{f}_n &= \frac{1}{2b} \int_{-b}^b \sum_l \sum_m \nu_l^2 \phi_m e^{i(l+m-n)\lambda y} dy \\ &= \sum_l \sum_m \nu_l^2 \phi_m \delta(l+m-n) \end{aligned} \quad (3.24)$$

where $\delta(s) = 1$ for $s = 0$ and zero otherwise. We thus require the condition $l + m - n = 0$ in order to obtain a contribution to the surface wave mode by the bottom. For an arbitrary choice of l and a subsequently fixed value of $m = n - l$, we obtain the expression

$$\hat{f}_n = \sum_{l=-\infty}^{\infty} \nu_l^2 \phi_{n-l} \quad (3.25)$$

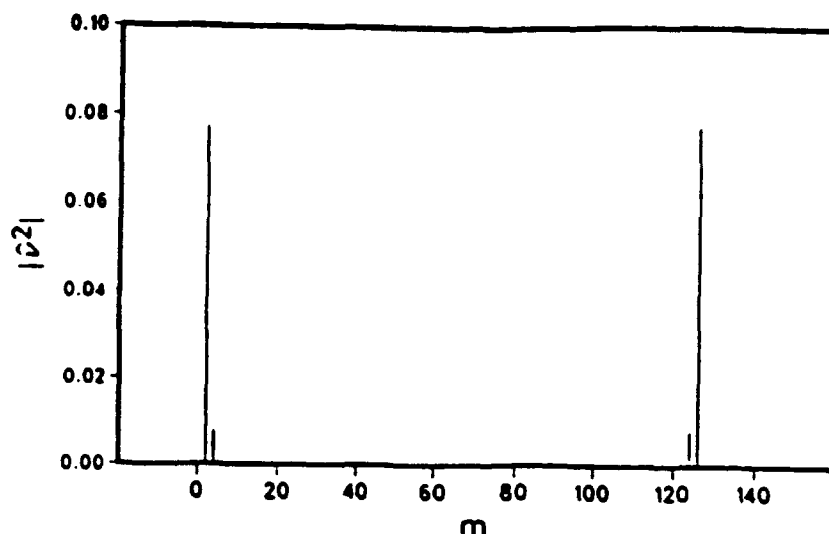


Figure 6: Amplitude Spectrum of the Bottom Modes, $\nu^2(x, m\lambda)$, from Dalrymple and Suh, 1988

When this term is substituted back into (3.22), it is clear that the effect of F_n is to scatter energy into (or out of) mode n through resonant interaction between a surface wave at mode $n - l$ and a bottom mode l . The interaction is a linear process, since the amplitudes ν_l^2 are fixed. The formulation may be interpreted as a generalization of the Bragg scattering mechanism described by Mei (1985) for forward propagation over a sinusoidal bed (actually not explicitly covered here) and by Naciri and Mei (1988) for waves propagating over a bi-periodic bottom. In this extension, the entire problem of wave deformation by a non-uniform bottom may be viewed as the result of a complicated multiple scattering problem involving the entire set of Fourier modes resolved by the system.

In practice, it is possible either to use the FFT and inverse FFT algorithms to evaluate the last term in (3.22), or to evaluate the sum in (3.25) after evaluating the FFT of ν^2 . The operation count of the second option is smaller, although all exponentials involved in the computation of the FFT's may be evaluated once and then stored, making the subsequent FFT calls quite efficient.

Dalrymple and Suh (1988) show this interaction between the bottom and surface modes, using an idealized bathymetry consisting of sinusoidal corrugations perpendicular to the x axis, so that the major component of the bottom was ν_2^2 . The surface wave train was incident at an angle corresponding to ϕ_4 at $x=0$. According to (3.25), the next modes to be forced by the bottom are ϕ_2 and ϕ_6 . These modes then create additional modes. These results are shown on Figures 6 - 8, which show the evolution of the angular spectrum with distance, x , and the instantaneous water surface. Note that wave rays, obtained from refraction theory and depicted with solid lines, are also shown.

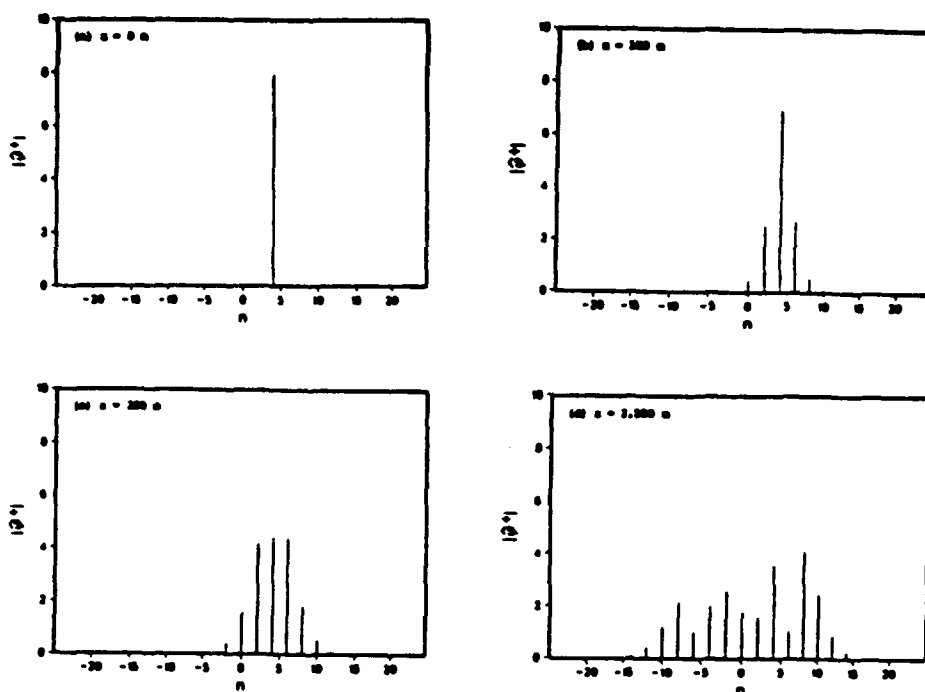


Figure 7: Evolution of the Angular Spectrum at Different x Locations, from Dalrymple and Suh, 1988

3.4 Nonlinear Effects

The solutions discussed so far have been for linear theory, which permits the summation over many wave directions. The water wave problem however is nonlinear, due to the free surface boundary conditions. There have been two approaches to solving a more nonlinear problem. The first is to replace the linear dispersion relationship (2.12) used to find the wave number given the wave frequency with a nonlinear dispersion relationship, which includes amplitude dispersion. Candidates for this dispersion relationship could be the Stokes third order relationship or the modified dispersion relationship of Kirby and Dalrymple (1986). This last relationship was used directly in the equations in Section 3.2, with very good agreement with laboratory data by Dalrymple *et al.* (1989).

The second approach is to rigorously satisfy the nonlinear governing equations, which are

$$\nabla^2 \Phi = 0 \quad (-h < z < \eta) \quad (3.26)$$

$$g\Phi_x + \Phi_t + |\nabla\Phi|^2 + \frac{1}{2}(\nabla\Phi \cdot \nabla)|\nabla\Phi|^2 = 0 \quad (z = \eta) \quad (3.27)$$

$$\Phi_t + \frac{1}{2}|\nabla\Phi|^2 + g\eta = 0 \quad (z = \eta) \quad (3.28)$$

$$\Phi_x = -\nabla_h \Phi \cdot \nabla_h h \quad (z = -h) \quad (3.29)$$

where ∇ and ∇_h are the three-dimensional and the horizontal gradient operators.

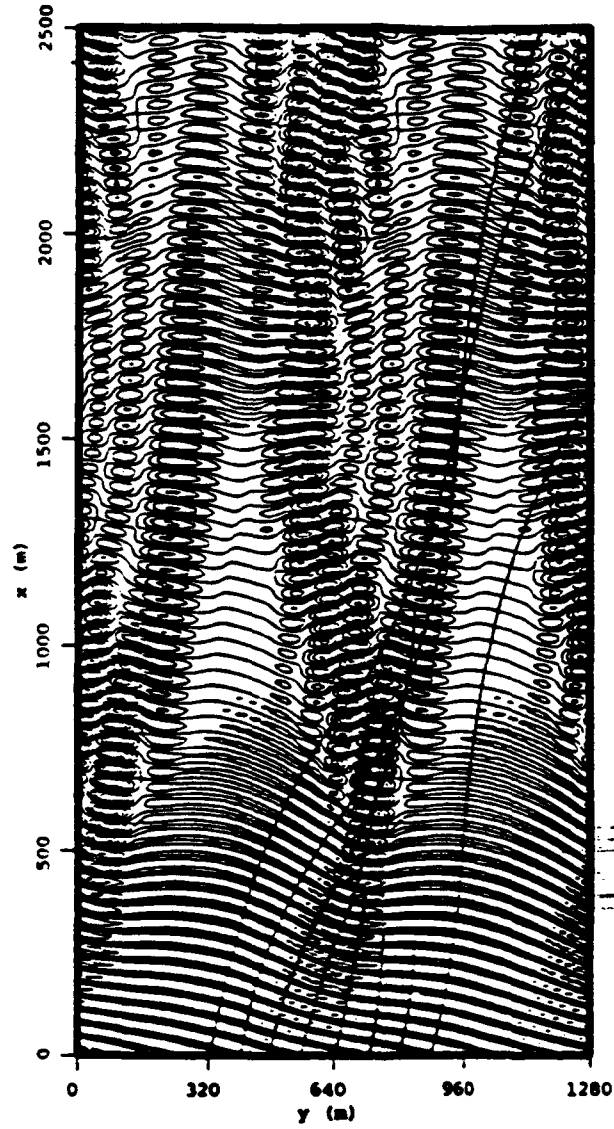


Figure 8: Instantaneous Water Surface Elevations Over Periodic Ridges, from Dalrymple and Suh, 1988

The methodology is to expand Φ and η in terms of a small parameter, ϵ , which is the Stokes steepness parameter,

$$\Phi = \sum_{n=1}^{\infty} \epsilon^n \phi_n; \quad \eta = \sum_{n=1}^{\infty} \epsilon^n \eta_n \quad (3.30)$$

Also the method of multiple scales is used, which has been shown to be very useful for wave evolution problems. Suh *et al.* (1990) chose the following slow variables

$$x_1 = \epsilon x, x_2 = \epsilon^2 x, \dots; t_1 = \epsilon t, t_2 = \epsilon^2 t, \dots \quad (3.31)$$

A mild slope bottom was assumed, such that $h_x \sim \epsilon^2 h_{x_2}$. This leaves the bottom effectively characterized by straight and parallel contours up until third order. Next, the Taylor series is used to expand the nonlinear free surface boundary conditions about $z = 0$ and the bottom boundary condition about $z = -\bar{h}$, which provides for series representations of these nonlinear conditions in linear form, ordered by the Stokes parameter. Finally, grouping the coefficients of each order of the Stokes parameter gives a boundary value problem for each order, n :

$$\nabla^2 \phi_n = F_n \quad (-\bar{h} < z < 0) \quad (3.32)$$

$$g\phi_{n,z} + \phi_{n,tt} = G_n \quad (z = 0) \quad (3.33)$$

$$\phi_{n,t} + g\eta_n = H_n \quad (z = 0) \quad (3.34)$$

$$\phi_{n,z} = B_n \quad (z = -\bar{h}) \quad (3.35)$$

where the forcing terms, F_n, G_n, H_n, B_n , are determined from solutions of lower order. See Suh *et al.* (1990) for the complete expressions for the right hand sides. The first order solution, as expected, is that of Dalrymple and Kirby (1988), for waves on straight and parallel contours. At the second order, the interaction of components of the first order directional spectrum leads to the appearance of sum and difference frequencies, including the usual Stokes harmonic. Additionally, forcing from the bottom occurs through the coupling term in Dalrymple *et al.* (1989). At the third order, the forcing of the wave field is due to third-order terms proportional to the first harmonics and a cubic resonance which results from the interaction of the primary waves and the second-order sum and difference waves or among three primary waves. New bottom coupling terms arise as well.

Suh *et al.* (1990) compared the third-order model to data (Booij, Berkhoff and Radder, 1982, Ito and Tanimoto, 1972), showing good agreement, far better than that obtained by linear theory. Another comparison was made to the nonlinear model of Dalrymple *et al.* (1989) on the BBR data set, also showing good agreement and indicating that, at least for the example shown, the two methods of including nonlinearity are almost equivalent. In fact, the Dalrymple *et al.* (1989) model has a computational advantage for most applications; however it does not include the wave-wave interactions as does Suh *et al.* (1990). Both models have the disadvantage that for very large angles, say greater than 50° , the model results begin to show discrepancies.

4 Shallow Water Waves

As waves propagate towards shore, they enter a region where the wavelength becomes long relative to the water depth, and the product kh in the dispersion relation (2.12) becomes small. In this case, the dispersion relation approaches the limiting form

$$\omega^2 = gk^2h \quad (4.1)$$

and wave speed $C = \omega/k$ becomes only weakly dependent on frequency. In this limit, all waves are travelling at nearly the same speed, and strong nonlinear coupling exists between waves of different frequency and direction. Prior to wave breaking, numerous studies have indicated that the Boussinesq equations (in which all frequencies are treated together) provide an adequate model for the wave field. To date, this problem has only been treated (from the angular spectrum point of view) for the case of topography varying in one direction; the case of two-dimensional topography has not been described as of yet. Kirby (1990) has developed a model for waves on an infinitely long beach and has compared model results to data and parabolic model results. This model will be presented here.

We first establish the form of a model for waves in a laterally unrestricted domain. Again, a Cartesian coordinate system is adopted which has x pointed in the onshore direction and y pointing alongshore. Depth is assumed to vary as $h(x)$ only. We take as a starting point the variable depth Boussinesq equations as given by Peregrine (1967):

$$\eta_t + \nabla \cdot (h\mathbf{u}) + \epsilon \nabla \cdot (\eta \mathbf{u}) = 0 \quad (4.2)$$

$$\mathbf{u}_t + \epsilon \mathbf{u} \cdot \nabla \mathbf{u} + g \nabla \eta = \mu^2 \left\{ \frac{h}{2} \nabla (\nabla \cdot (h\mathbf{u}_t)) - \frac{h^2}{6} \nabla (\nabla \cdot \mathbf{u}_t) \right\} \quad (4.3)$$

Here, η is the surface displacement and \mathbf{u} is the horizontal wave-induced velocity vector. The equations are kept in dimensional form; the scaling parameters ϵ for nonlinearity and μ^2 for weak dispersion are present only schematically and will be subsequently dropped. We will assume that either bottom slope or the amplitude of bottom features (as scaled by water depth) are also small and hence the model will be developed to leading order in nonlinearity, dispersion, and domain inhomogeneity. This leads to immediate neglect of bottom slope effects in the dispersive terms of (4.3). Using the linear portion of (4.2), we may then write (4.3) in the reduced form

$$\mathbf{u}_t + \mathbf{u} \cdot \nabla \mathbf{u} + g \nabla \eta + \frac{h}{3} \nabla \eta_t = 0. \quad (4.4)$$

We now make the following two assumptions. First, the model will be applied to time-periodic wave trains, where periodicity is in the sense of either a regular wave train, or of a discrete FFT over a finite length of sampled data. This assumption has been routinely applied in the spectral sense in the one-directional shoaling model of Freilich and Guza (1984) (see also Elgar and Guza, 1985). Its interpretation in the regular wave case is straightforward, with the wave being separated into its harmonic components (Rogers and Mei, 1978; Liu, Yoon and Kirby, 1985, hereafter referred to as LYK). Secondly, the wave field will be assumed

to be periodic in the transverse y direction. This corresponds again to a fixed longshore wavelength in the regular wave case, or to periodicity over a long spatial interval in the spectral sense.

The governing equations are first split into coupled elliptic models for separate harmonic components. Following LYK, the surface displacement and velocity are written as

$$\eta = \sum_{n=0}^N \frac{\eta_n(x, y)}{2} e^{-in\omega t} + c.c. \quad (4.5)$$

$$u = \sum_{n=0}^N \frac{u_n(x, y)}{2} e^{-in\omega t} + c.c. \quad (4.6)$$

Substitution of (4.5) and (4.6) in (4.2) and (4.4) and subsequent elimination of the velocity leads to the following model equation for the η_n in the horizontal plane:

$$n^2 \omega^2 \eta_n + \nabla \cdot (G_n \nabla \eta_n) + [n.l.t.]_n = 0; \quad n = 1, \dots, N \quad (4.7)$$

Here, $[n.l.t.]_n$ denotes the nonlinear interactions with other discrete frequency components which are sorted by means of the rules for triad interactions applied to the time dependence; complete expressions may be found in Kirby (1990). The mode $n = 0$ corresponding to the steady, wave-induced setdown is neglected since it is at most second order in the largest wave amplitudes present (see LYK). Also,

$$G_n(x) = gh(x) - \frac{1}{3} n^2 \omega^2 h^2(x). \quad (4.8)$$

We now Fourier transform the wave field in the y direction, assuming propagation is to be considered in the on-offshore ($\pm x$) direction. We consider here the case of an unbounded lateral domain and a wave field which is periodic over the basic interval $-b < y < b$. We then represent $\eta_n(x, y)$ as

$$\eta_n(x, y) = \sum_{m=-M}^M \eta_n^m(x) e^{im\lambda y} \quad (4.9)$$

where

$$\lambda = \frac{\pi}{b}. \quad (4.10)$$

as before. Substituting (4.9) in (4.7) and neglecting x - derivatives of small terms in G_n then leads to a set of coupled second-order ODE's for the η_n^m , given by

$$\begin{aligned} \frac{G_n}{gh} \eta_{n,xx}^m + \frac{h_x}{h} \eta_{n,x}^m + (\gamma_n^m)^2 \eta_n^m + \frac{1}{3} m^2 n^2 \lambda^2 k^2 h^2 \eta_n^m + \frac{1}{gh} [n.l.t.]_n^m &= 0; \\ n = 1, \dots, N; \quad m = -M, \dots, M. \end{aligned} \quad (4.11)$$

where $[n.l.t.]_n^m$ now represents triad interactions satisfying resonance conditions in t and y . Here, k is the wavenumber determined by the lowest order dispersion relation (4.1). Also,

$$(\gamma_n^m)^2 = n^2 k^2 - m^2 \lambda^2 \quad (4.12)$$

For fixed n, k, λ , large values of m will make γ_n^m imaginary, which corresponds to modes which are exponential rather than oscillatory in x in the linear approximation. In the linear case, the presence of these modes in the initial conditions would be interpreted in the same light as the presence of evanescent modes in the wavemaker problem discussed in Section 2.1.1. However, the interpretation in the case of possible nonlinear forcing of the offshore portion of trapped modes in the nearshore region is non-trivial and will need to be considered carefully in applications where the inclusion of this effect is desired. In addition, nonlinearity could force the propagation of modes that would not be present in a linearized wave field, and which could affect a detailed representation of an individual wave. At present, the range of M at each value of n may be restricted to $M_n \leq nk/\lambda$ in order to eliminate forcing of these modes arbitrarily.

4.1 Shoaling waves

The model developed in the previous section allows for the onshore and offshore propagation of the directional spectrum components. Here, attention is restricted to waves propagating onshore, or in the positive sense with respect to the x coordinate.

Based on the linear, nondispersive portion of the model (4.11), we assume that the incident wave may be written in the form

$$\eta_n^m(x) = A_n^m(x) e^{i n \int k \tilde{\gamma}_n^m dx} \quad (4.13)$$

where it is assumed that the x dependence of A , k and $\tilde{\gamma}$ is on a slow scale of $O(\epsilon)$, and where

$$\tilde{\gamma}_n^m = (1 - (\frac{m}{n})^2 (\frac{\lambda}{k})^2)^{1/2} = \frac{\gamma_n^m}{nk} \quad (4.14)$$

(where the positive root is taken). The amplitudes A represent the discrete angular spectrum being considered here, and are allowed to vary owing to refraction, shoaling, dispersion and nonlinear interaction. (It would be possible to absorb shoaling and refraction effects by the use of the usual linear refraction formulae; this step is not taken here.) Substitution of (4.13) in (4.11) leads to the spectral model for incident waves, given by

$$\begin{aligned} & \tilde{\gamma}_n^m A_{n,x}^m + \frac{(kh\tilde{\gamma}_n^m)_x}{2kh} A_n^m - \frac{1}{6} i n^3 k^3 h^2 A_n^m \\ & + \frac{ink}{8h} \left\{ \sum_{l=1}^{n-1} \sum_{p=P_1}^{P_2} I_{n,l}^{m,p} A_l^p A_{n-l}^{m-p} e^{i \int \Theta_{n,l}^{m,p} dx} + 2 \sum_{l=1}^{N-n} \sum_{p=P_3}^{P_4} J_{n,l}^{m,p} A_l^{p*} A_{n+l}^{m+p} e^{i \int \Upsilon_{n,l}^{m,p} dx} \right\} = 0; \\ & n = 1, \dots, N; \quad m = -M_n, \dots, M_n. \end{aligned} \quad (4.15)$$

Here, $(\cdot)^*$ denotes the complex conjugate. The limits of summation $P_1 - P_4$ are given by

$$\begin{aligned} P_1 &= \max(-M_l, -M_{n-l} + m) \\ P_2 &= \min(M_l, M_{n-l} + m) \\ P_3 &= \max(-M_l, -M_{n+l} - m) \\ P_4 &= \min(M_l, M_{n+l} - m) \end{aligned} \quad (4.16)$$

The interaction coefficients I and J are given by

$$I_{n,l}^{m,p} = 1 + [\tilde{\gamma}_l^p \tilde{\gamma}_{n-l}^{m-p} + \frac{p}{l} \frac{m-p}{n-l} (\frac{\lambda}{k})^2] \cdot [1 + (\frac{m}{n})^2 (\frac{\lambda}{k})^2 + \frac{(l\tilde{\gamma}_l^p + (n-l)\tilde{\gamma}_{n-l}^{m-p})^2}{n^2}] \quad (4.17)$$

$$J_{n,l}^{m,p} = I_{n,-l}^{m,-p}. \quad (4.18)$$

The phase arguments Θ and Υ represent the basic mismatch in the x direction of the triads chosen based on perfect matching in y and t . Generally, the only components which experience complete resonance in the long wave limit must have parallel propagation directions; all obliquely interacting components are somewhat detuned. The phase arguments are given by

$$\Theta_{n,l}^{m,p} = lk\tilde{\gamma}_l^p + (n-l)k\tilde{\gamma}_{n-l}^{m-p} - nk\tilde{\gamma}_n^m \quad (4.19)$$

$$\Upsilon_{n,l}^{m,p} = \Theta_{n,-l}^{m,-p} \quad (4.20)$$

The spectral model (4.15) is a set of coupled first order ODE's which are solvable by standard techniques. Results were obtained using a 4th-order Runge-Kutta scheme.

4.2 Comparison with Laboratory Data

In order to verify the basic computational model provided by (4.15), Kirby (1990) compared model predictions to the laboratory data obtained by Hammack *et al.* (1990) for the case of glancing, or Mach, reflection of a cnoidal wave by a vertical wall. Additional comparisons were made with parabolic models. The experimental tests were conducted using the directional wave maker at the Coastal Engineering Research Center, Vicksburg, MS. A prior use of this facility to study the properties of intersecting cnoidal waves is described in Hammack *et al.* (1989), referred to here as HSS, who also discuss the instrumentation and data acquisition used.

For the tests considered here, the wave basin was operated with a water depth of 20cm in a constant depth region extending 12.55m in front of the wavemaker, after which a beach with 1:30 slope provided an efficient wave absorber giving little reflection. For the Mach stem tests, two parallel false walls were installed perpendicular to the wavemaker axis in order to provide a closed channel. The channel walls were situated 13.26m apart, which fixes the width of the numerical domain to be considered.

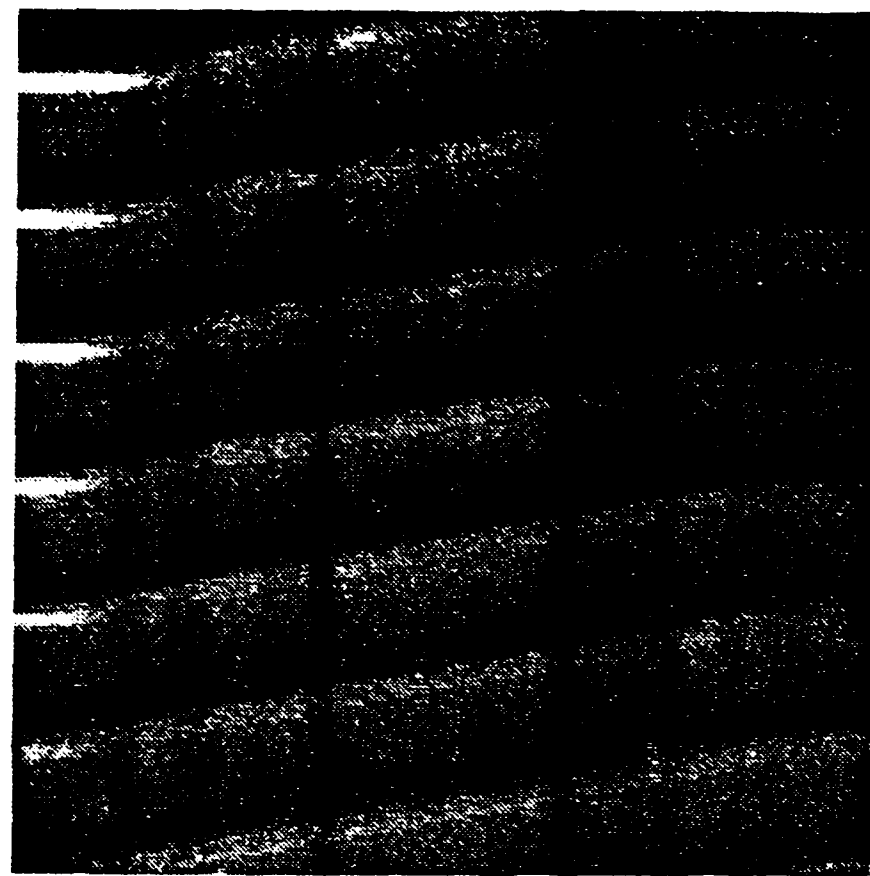
The generation of oblique cnoidal waves using the directional wavemaker has been described in HSS. In the present laboratory tests, waves were initially specified as having a wavelength of 2m and a crest elevation 4cm above mean water level.

A sample of the model calculations are presented here as gray level contour plots of instantaneous surface over the model basin. The gray level plots are actually of the quantity $-\partial\eta/\partial x$, and the pictures thus mimic the visual image that would be obtained in an overhead photograph resulting from lighting at a low angle from the direction of the wavemaker. (This is similar to the photographic arrangement in HSS). Figure 9 presents results for the test

13.25

 $\chi(\alpha)$

0

 $\eta(\alpha)$

-13.25

Figure 9: Reflection of Cnoidal Wave from Barrier, Corresponding to TEST CR150204 (Kirby, 1990)

CR150204, which clearly shows the evolution of a wide Mach stem wave along the reflecting boundary. In contrast, Figure 10 shows the other extreme example of test CR580204, where the angle of incidence is about 45° and the reflection pattern is regular (i.e., nearly linear superposition.) The reader is referred to Kirby (1990) for a detailed comparison between model results and the laboratory data.

5 Conclusions

The angular spectrum method for both intermediate and shallow water depths provides a useful tool for the propagation of water waves. It has the advantage of including refraction, diffraction, and shoaling, but permitting larger angles of propagation than the parabolic models permit.

The angular spectrum provides an interesting interpretation of diffraction. For the case of diffraction through a gap, treated by the Kirchhoff approximation, the initial condition contains all the information for diffraction. The circular spreading of waves behind a gap is simply the radial spreading associated with the different propagation directions of the

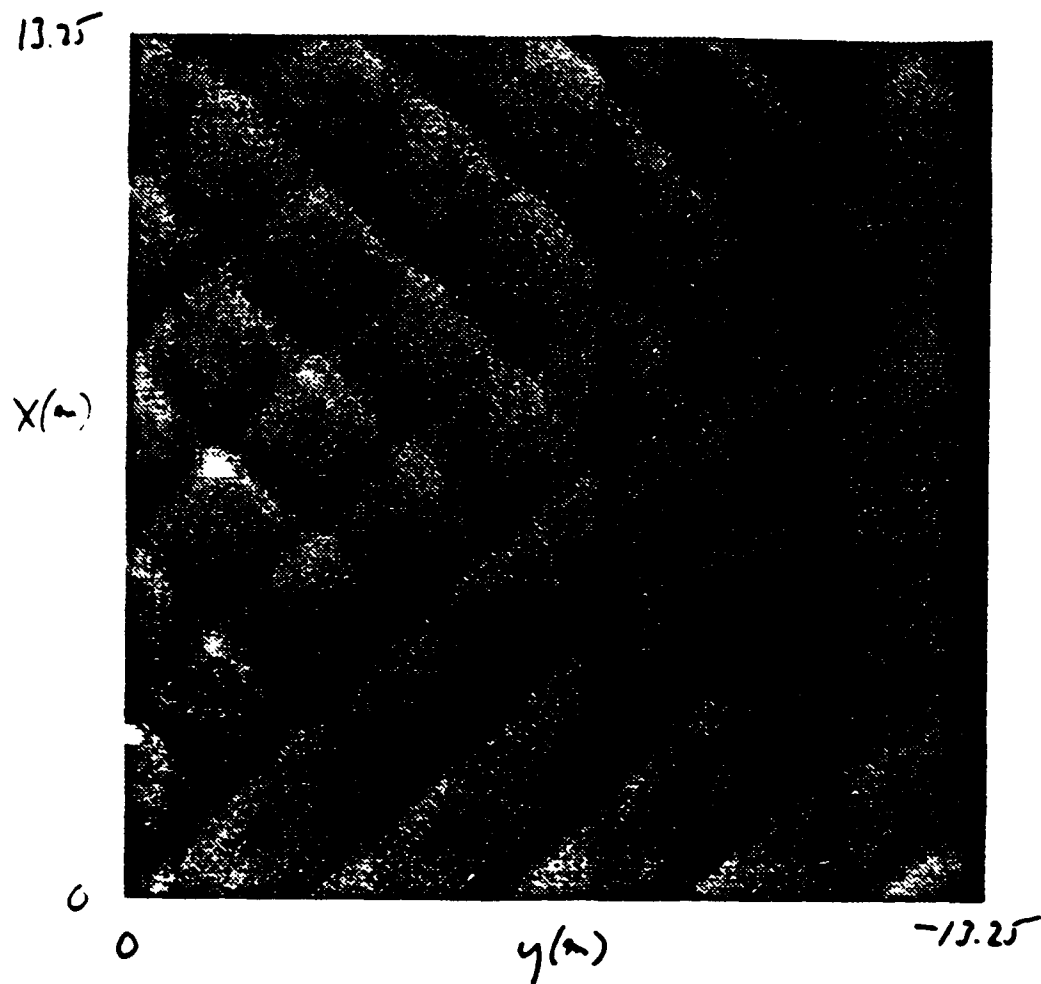


Figure 10: Reflection of Cnoidal Wave from Barrier, Corresponding to TEST CR580204 (Kirby, 1990)

Fourier modes. There is no coupling between the modes when there is no lateral variation in bathymetry. Further for cases where diffraction occurs within the computational domain, say, behind a shoal surrounded by constant depth water, the coupling between the bottom modes and the surface wave modes over the shoal forces new modes to grow which, behind the shoal, lead to the characteristic focus and diffraction regions. However, for linear wave models, there is no coupling between the modes after the waves pass over the (refractive) shoal region.

In shallow water, the mode coupling is very strong and plays a major role in the computations. However, comparisons to data show that the angular spectrum model is very good; in fact, better than parabolic representations of the Boussinesq equations.

Future work in angular spectrum modelling will be directed to the development of an elliptic angular spectrum model to provide for reflection upwave and the application to a full directional spectrum by superposing many frequencies.

6 References

1. Berkhoff, J.C.W., "Computation of Combined Refraction-diffraction," *Proc. 13th Intl. Coastal Engin. Conf.*, ASCE, 471-490, 1972.
2. Berkhoff, J.C.W., N. Booij, and A.C. Radder, "Verification of Numerical Models for Simple Harmonic Linear Waves," *Coastal Engineering*, 6, 255-279, 1982.
3. Bettess, P. and O.C. Zienkiewicz, "Diffraction and Refraction of Surface Waves Using Finite and Infinite Elements," *Int. J. Numerical Meth. in Eng.*, 11, 1271-129, 1977.
4. Booij, N., Gravity Waves on Water with Non-uniform Depth and Current, Department of Civil Engrg., Tech. Univ. Delft, Rpt. 81-1, 1981.
5. Booker, H.G. and P.C. Clemmow, "The Concept of an Angular Spectrum of Plane Waves, and its Relation to that of Polar Diagram and Aperture Distribution," *Proc. Instn. Elect. Eng.*, Pt III, 97, 11, 1950.
6. Clemmow, P.C., *The Plane Wave Spectrum Representation of Electromagnetic Fields*, Oxford: Pergamon Press, 185pp, 1966.
7. Dalrymple, R.A., "A Model for the Refraction of Water Waves," *Journal of Waterway, Port, Coastal and Ocean Eng.*, ASCE, 114, 4, 423-435, 1988.
8. Dalrymple, R.A., "Directional Wavemaker Theory with Sidewall Reflection," *Journal of Hydraulic Research*, 27, 1, 1989.
9. Dalrymple, R.A. and M. Greenberg, "Directional Wavemakers," in *Physical Modelling in Coastal Engineering*, R.A. Dalrymple, ed., Rotterdam: A.A. Balkema, 1985.
10. Dalrymple, R.A. and J.T. Kirby, "Models for Very Wide Angle Water Waves and Wave Diffraction," *J. of Fluid Mech.*, 192, 33-50, 1988.

11. Dalrymple, R.A. and P.A. Martin, "Wave Diffraction Through Offshore Breakwaters," *J. Waterway, Port, Coastal and Ocean Engineering*, 116, 6, ASCE, 1990.
12. Dalrymple, R.A. and K. Suh, "Wide-angle water Wave Models Using Fourier Method," *Proc. 21st Int. Conf. Coastal Engineering*, ASCE, Torremolinos, 246-260, 1988.
13. Dalrymple, R.A., K. Suh, J.T. Kirby and J.W. Chae, "Models for Very Wide Angle Water Waves and Wave Diffraction, Part 2. Irregular bathymetry" *J. Fluid Mech.*, 201, 299-322, 1989.
14. Dean, R.G. and Dalrymple, R.A., *Water Wave Mechanics for Engineers and Scientists*, Englewood Cliffs: Prentice-Hall, pp. 353, 1984; reprinted by World Scientific, Singapore, 1990.
15. Ebersole, B.A., "Refraction-diffraction Model for Linear Water Waves," *J. Waterway, Port, Coastal and Ocean Engineering*, 111, 6, ASCE, 1985.
16. Elgar, S. and R.T. Guza, "Shoaling Gravity Waves: Comparisons Between Field Observations, Linear Theory, and a Nonlinear Model," *J. Fluid Mech.*, 158, 47-70, 1985.
17. Freilich, M.H. and R.T. Guza, "Nonlinear Effects on Shoaling Surface Gravity Waves," *Phil. Trans. Roy. Soc. Lond., A*, 31, 1-41, 1984.
18. Goodman, J.W., *Introduction to Fourier Optics*, San Francisco: McGraw-Hill, pp 287, 1968.
19. Hammack, J., N. Scheffner and H. Segur, "Two-dimensional Periodic Waves in Shallow Water," *J. Fluid Mech.*, 209, 567-589, 1989.
20. Hammack, J., N. Scheffner and H. Segur, personal communication, 1990.
21. Houston, J.R., "Combined Refraction and Diffraction of Short Waves Using the Finite Element Method," *Applied Ocean Research*, 3, 163-170, 1981.
22. Ito, Y. and K. Tanimoto, "A Method of Numerical Analysis of Wave Propagation: Application to Wave Diffraction and Refraction," *Proc. 13th Intl. Conf. Coastal Engrg.*, ASCE, Vancouver, 503-522, 1972.
23. Kirby, J.T., "Higher-order Approximations in the Parabolic Equation Method for Water Waves", *J. Geophys. Res.*, 91, 933-952, 1986a.
24. Kirby, J. T., "Rational Approximations in the Parabolic Equation Method for Water Waves", *Coastal Engineering*, 10, 355-378, 1986b.
25. Kirby, J.T., "Modelling Shoaling Directional Wave Spectra in Shallow Water", *Proc. 22nd Intl. Conf. Coastal Engrg.*, ASCE, Delft, 1990.
26. Kirby, J.T. and R.A. Dalrymple, "A Parabolic Equation for the Combined Refraction-diffraction of Stokes Waves by Mildly Varying Topography," *J. Fluid Mech.*, 136, 453-466, 1983.
27. Kirby, J.T. and R.A. Dalrymple, "An Approximate Model for Nonlinear Dispersion in Monochromatic Wave Propagation Models," *Coastal Engineering*, 9, 1986.

28. Liu, P.L.-F. and C.C. Mei, "Water Motion on a Beach in the Presence of a Breakwater, I. Waves" *J. Geophys. Res.*, C, 81, 3079-3084, 1976.
29. Liu, P.L.-F. and T.K. Tsay, "Refraction-diffraction Model for Weakly Nonlinear Water Waves," *J. Fluid Mech.*, 141, 265-274, 1984.
30. Liu, P.L.-F., Yoon, S.B. and Kirby, J.T., 1985, "Nonlinear Refraction-diffraction of Waves in Shallow Water", *J. Fluid Mech.*, 153, 185-201.
31. Lozano, C.J. and P.L.-F. Liu, "Refraction-diffraction Model for Linear Surface Water Waves," *J. Fluid Mech.*, 101, 1980.
32. Mei, C. C., "Resonant Reflection of Surface Water Waves by Periodic Sandbars", *J. Fluid Mech.*, 152, 315-335, 1985.
33. Munk, W.H. and R.S. Arthur, "Wave Intensity along a Refracted Ray in Gravity Waves," *Natl. Bur. Stand. Circ.* 521, Washington, D.C., 1952.
34. Naciri, M. and Mei, C. C., "Bragg Scattering of Water Waves by a Doubly Periodic Seabed", *J. Fluid Mech.*, 192, 51-74, 1988.
35. Noda, E.K., "Wave-induced Nearshore Circulation," *J. Geophysical Res.*, 79, 27, 4097-4106, 1974.
36. Penney, W.G. and A.T. Price, "The Diffraction Theory of Sea Waves and the Shelter Afforded by Breakwaters," *Philos. Trans. Roy. Soc.*, A, 244(882), 236-253, 1950.
37. Peregrine, D.H., "Long Waves on a Beach", *J. Fluid Mech.*, 27, 815-827, 1967.
38. Perlin, M. and R.G. Dean, "An Efficient Numerical Algorithm for Wave Refraction/shoaling Problems," *Proc. Coastal Structures*, 83, ASCE, 988-999, 1983.
39. Radder, A.C., "On the Parabolic Equation Method for Water-wave Propagation", *J. Fluid Mech.*, 95, 1, 159-176, 1979.
40. Rodgers, S.R. and C.C. Mei, "Nonlinear Resonant Excitation of a Long and Narrow Bay," *J. Fluid Mech.*, 88, 161-180, 1978.
41. Sommerfeld, A., "Mathematische Theorie der Diffraction," *Math. Ann.*, 47, 317-374, 1898.
42. Smith, R. and Sprinks, T., "Scattering of Surface Waves by a Conical Island," *J. Fluid Mechanics*, 72, 2, 373-384, 1975.
43. Stamnes, J.J., *Waves in Focal Regions : Propagation, Diffraction and Focussing of Light, Sound and Water Waves*, Boston : Adam Hilger, 1986.
44. Stamnes, J.J., Lovhaugen, O., Spjelkavik, B., Mei, C.C., Lo, E. and Yue, D.K.P., "Nonlinear Focussing of Surface Waves by a Lens-Theory and Experiment", *J. of Fluid Mech.*, 135, 71-94, 1983.
45. Suh, K.D., R.A. Dalrymple, and J.T. Kirby, "An Angular Spectrum Model for Propagation of Stokes Waves," *J. Fluid Mech.*, 221, 205-232, 1990.